Detection and characterization of cerebral microbleeds : application in clinical imaging sequences on large populations of subjects

Takoua Kaaouana

University PIERRE ET MARIE CURIE

PHD THESIS

Doctoral school Brain-Cognition-Behaviour (ED3C)

Presented by

Takoua KAAOUANA

Detection and characterization of cerebral microbleeds: Application in clinical imaging sequences on large populations of subjects

prepared at ICM, ARAMIS LAB, Paris

defended on December 21^{th}, 2015

Jury

Isabelle Bloch	Reviewer
Emmanuel Barbier	Reviewer
Habib Benali	Examiner
Charlotte Cordonnier	Examiner
Paulo Loureiro de sousa	Examiner
Ludovic De rochefort	Co-advisor
Marie Chupin	Co-advisor
Didier Dormont	Advisor

Remerciement

Ce remerciement est sans doute l'une des choses que j'appréhendais le plus depuis la soutenance. C'est le moment de penser à toutes les personnes qui ont participé à l'élaboration de ce travail aussi bien sur le plan professionnel que personnel, c'est un moment de recul sur les trois années d'une thèse, pour moi c'est un bien plus. Mes souvenirs remontent à ce moment en 2008 quand j'ai eu le visa pour aller étudier en France. Ce moment où j'ai senti que ma vie allait changer, que je ne passerai plus mes journées à flâner les rues de Tunis avec mon amie, Amira. La destination ne me préoccupe pas, je me préoccupais plus de Tunis et comment quitter Tunis, cette ville à la fois dure et généreuse. Comment me préparer ? On n'est jamais prêt à quitter Tunis !

J'ai quitté Tunis et j'ai démarré une nouvelle vie à Toulouse où j'ai appris à vivre autrement. Je voulais juste suivre mon rêve, le rêve d'être une femme différente.

J'ai suivi mon rêve et aujourd'hui je suis Docteur en science et j'en suis ravie et fière. Pour cela je remercie d'abord et avant tout mes parents qui ont cru en moi, qui ont risquaient leur confort en me faisant confiance dans une société orientale si compliquée. Sans votre soutien, je n'aurais jamais vécu tout ce que j'ai vécu ces sept dernières années.

J'exprime ma profonde gratitude à ma directrice de thèse, Marie Chupin. Merci à toi Marie de m'avoir proposé cette thèse. Merci d'avoir cru en moi et de m'avoir laissé une liberté pour travailler sur des axes qui m'intéressaient. Merci pour tes conseils avisés, ton écoute et de m'avoir consacré tant de temps. Je te remercie énormément sur ton sens des rapports humains ; Merci d'avoir su m'épauler dans tant de preuves endurées pendant cette thèse. Je penserai toujours à toi quand j'écouterai « Imagine » de John Lennon.

Il en va aussi pour Ludovic de Rochefort. Sa connaissance, sa gentillesse, sa rigueur, sa disponibilité et son empathie ont joué un rôle clé dans ma thèse. Je te remercie pour ces différentes discussions enrichissantes, de tout ce que tu m'as appris sur l'IRM et de m'avoir encouragé toujours pour aller de l'avant. Ludovic, je t'en serais toujours reconnaissante.

Je remercie également Didier Dormont pour ses encouragements, ses lectures, les informations cliniques partagés et qui ont mis du sens à tout ce qu'on a fait.

Je remercie les membres du jury présidé par Habib Ben Ali. Je remercie tout particulièrement Isabelle Bloch et Emmanuel Barbier de m'avoir fait l'honneur d'être rapporteurs de ce travail. Je leur exprime toute ma reconnaissance pour le temps qu'ils ont consacré à la lecture approfondie de ce manuscrit ainsi que pour les retours si constructifs qu'ils m'ont adressés. Je remercie aussi

chaleureusement Charlotte Cordonnier, Paulo Loureiro de Sousa d'avoir accepté de faire partie de mon jury de thèse, je suis honorée.

Je remercie également tous les cliniciens qui ont participé à cette étude et surtout Anne Bertrand et Christine Delmaire.

Je remercie tous les Aramisiens pour cette agréable et amicale ambiance qu'ils créent, Merci Olivier de m'avoir accueilli dans cette équipe, Merci à tous les étudiants, post doc, arc, ingénieurs et titulaires. Mes pensées vont d'abord au méchant italien ; merci d'avoir rendu ma thèse un bon et fun souvenir. Je n'oublierai jamais tes blagues à l'italienne (celle à Cannes et celle de Allah resteront mes préférés). Merci d'avoir était un super ami avec qui j'ai partagé des moments de joies, de réussite mais aussi des moments moins joyeux. Merci à toi ma petite Claire, d'être là quand j'avais besoin de toi, reste comme tu es, une si belle, joyeuse et optimiste personne. Gentil Thomas, je te remercie de ton aide, ton humour, ta générosité et ta patience. Ludo, c'est un plaisir de connaitre une personne aussi respectueuse et sur qui on peut vraiment compter, Merci gentleman. Hugo, merci de ton amitié, ta gentillesse et ta positivité sans limite. Ana, rien que te voir me fait du bien. Au nom de tous les doctorants, je te remercie, tu es comme une aide divine envoyée pour nous épauler et nous remonter le moral. Chabha, ma confidente, je te remercie profondément de m'avoir aidé à surmonter des moments difficiles, je n'oublierais jamais ça. Merci également à Linda, Ali, Thomas et Johanne j'aurais aimé que vous soyez là pour partager ce moment de bonheur avec vous. Alex, le dealer, merci de ton humour et ta générosité. Catherine, merci de tes conseils théâtrales et de ton amitié. Merci Sonia de ta générosité et ton amitié. Merci Barbara, Fanny, JB, Jeremy, Xavier, Mario, Fabrizio et tous les membres de l'équipe Aramis que je n'ai pas pu citer ici.

Je remercie les gens que j'ai rencontré en France et qui sont devenus comme une famille pour moi ; la famille Boughattas pour leur accueil, leur générosité et leur soutien que je n'oublierai jamais. Merci à toute la famille Sassi qui m'ont tant aidé et soutenu, Merci Inés et khalti Ltifa. Merci à toi Isabelle de ton amitié et de ton soutien. Merci à Ahmed et Rim, Amal pour votre amitié.

Je remercie mes cousines et mes amies tunisiennes qui ont été là pour moi malgré la distance: Amira, Zohra, Imen, Hajer, Abrar kaouther, Olfa, Najia et mes tantes Khatwiya et Najiba.

Merci Anis pour tes encouragements et ton soutien.

Pour toi mon oncle, j'aurais été si fière de te dire que j'ai réussi.

Pour omi Jamila, pour ton amour et ta tendresse

Pour celle à qui je n'ai pas eu l'occasion de faire mes adieux, khdaiej

J'exprime ma profonde gratitude à ma sœur si exceptionnelle, Yathreb et mes deux frères, Abdallah et Haroun. Yathroubti, merci de m'avoir soutenue sans limite. Pour moi, tu étais toujours une petite lumière d'espoir pour me relever.

Moez, notre amour a certainement rendu l'épreuve encore plus dure mais sans toi rien de tout cela n'aurait un sens. On a rêvé ensemble et on continuera de rêver car nous sommes des Hommes libres.

C'est pour baba et ommi pour leur soutien et leur amour inconditionnels.

Pour Raoued que je rêve de voir briller

Je dédie affectueusement cette thèse à ma Tunisie qui continue de se battre pour sa liberté.

* * *

« Changer n'est pas devenir quelqu'un d'autre, c'est devenir qui on est... et l'accepter »

–Jacques Salomé–

Contents

List of Figures

List of Tables

Glossary

2DHF 2D harmonic filtering

AD Alzheimer's Disease

APP Amyloid Precursor Protein

APP Amyloid Precursor Protein

BOMBS Brain Observer Microbleed Scale

CAA Cerebral Amyloid Angiopathy

CAA Cerebral amyloid angiopathy

CATI Centre pour acquisition et traitement d'image

CGS Centimetre–Gram–Second system of units

CMBs Cerebral Microbleeds

CMCs Cerebral Micro-Calcifications

CSF Cerebral Spinal Fluid

ECD Equivalent Circular Diameter

ESWAN Enhanced Susceptibility weighted angiography

FID Free-Induction Decay

FN False negatives

FP False positives

FRST function of radial symmetry transform

FSE Fast Spin Echo

GM Gray Matter

GRE Gradient-Recalled-Echo

GUI Graphical User Interface

HPF High Pass Filtering

HTA Hypertensive Arteriopathy

HTA Hypertensive arteriopathy

ICC Intraclass Correlation Coefficient

ICH Intra-Cerebral Hemorrhage

IFM Internal Field Maps

MARS The Microbleed Anatomical Rating Scale

MEDI Morphology Enabled Dipole Inversion

MIDAS Microbleed Detection Using Automated Segmentation

mIP Minimal Intensity Projection

MNI Montreal Neurological Institute

MR Magnetic Resonance

MR Magnetic Resonance

MRI Magnetic Resonance Imaging

NMR Nuclear Magnetic Resonance

PD proton Density

PDF Projection onto Dipole Fields

PET Positron Emission Tomography

ppm Part Per Million

QSM Quantitative Susceptibility Mapping

RA Relative anisotropy

RF Radiofrequency

ROI Regions-of- interest

RST Radial Symmetry Transform

SE Spin-Echo

SHARP Sophisticated Harmonic Artifact Reduction on Phase data

SI System of Units

SNR Signal to noise ratio

SPM Statistical Parametric Mapping

SVM Support vector machines

SWI Susceptibility Weighted Imaging

T Tesla

TE Echo Time

TKD Truncated K-space division

TP True Positives

TR Repetition Time

TS Total Susceptibility

WM White Matter

INTRODUCTION

With the overall ageing of the population, dementia has become a major challenge for public health systems. Alzheimer's disease (AD) is considered the most common form of dementia affecting this population, followed by vascular dementia. It would affect 860000 people in France, with 250000 new cases reported each year. AD is a neuro-degenerative disease that affects brain tissues and its main clinical pattern is a gradual and irreversible loss of cognitive functions such as memory. On MRI or histology, it is associated with a systematic pattern of progressive damage of brain structures, from the temporal cortex to more widespread regions. AD's pathophysiology is not yet completely understood, but two types of lesions are considered as related with AD processes: amyloid plaques, that are an accumulation of amyloid peptide located in both neocortex and hippocampus, and neurofibrillary tangles. However, there may not be such a clear-cut partition between AD and vascular dementia. In fact, a high prevalence (20-30 %) has been observed for cerebro-vascular lesions in patients with AD while 30 to 50% of patients with vascular dementia show AD-related histological lesions. This overlap between vascular and degenerative lesions may suggest the involvement of common vascular factors in vascular dementia and AD.

Alzheimer's disease was declared a major national cause in France in 2007. Among AD-related issues, early diagnosis required particular attention and has been focused on by the neuroimaging community through the search for efficient imaging biomarkers.

In particular, recent advances of Magnetic Resonance Imaging make it possible to detect different types of structural and functional abnormalities at an early stage of the disease. The most commonly used MRI anatomical biomarkers for AD are brain and hippocampal volume loss. Furthermore, MRI allows assessing three types of vascular abnormalities: white matter hyper intensities (leucoariosis), lacuna (silent infarct) and cerebral microbleeds (CMBs). While white matter hyper intensities have a prevalence ranging from 28.9% to 100%, CMBs have a prevalence

of 23 % in patients with AD. Several studies have been undertaken to understand the clinical and pathophysiological significance of CMBs. However, large scale studies or meta-analyses are made difficult because their identification varies with MRI sequence parameters, suffers from reproducibility issues and is time-consuming. Automatic identification methods have been proposed to address these issues but they all require manual post processing selection steps, because of a very high number of false positives. This suggests that a better characterization of CMBs may be the key to improve their detection, as it would allow better identifying them from misleading structures and lesions.

This PhD focused on achieving a better characterization of CMBs to better detect them with an automatic method. It covers multiple aspects to improve CMBs identification. First, MR phase image was taken into account in addition to the standard MR magnitude image, because of its sensitivity to CMBs. A new MR phase image processing technique was developed to obtain the magnetic field of interest free of contamination from background sources in datasets equivalent to clinical routine. A comparison study was carried-out to evaluate the outcome of this tool for CMBs detection in a standardized dataset in a clinical environment. A proof-of-concept is given to illustrate the advantages of new features for automatically identifying CMBs.

This PhD thesis will be organized as follows. The first chapter presents the general context including an overview on clinical aspects of CMBs, a description of MR basis for their detection and the state of the art of CMBs identification methods. The objectives of this PhD are presented at the end of this chapter. The second chapter describes the main contribution of this thesis, a new MR phase processing technique for CMBs characterization from clinical routine datasets. The third chapter includes a detailed clinical routine validation of the new developed tool. The last chapter is a proof-of-concept of a new CMBs identification method.

This PhD was undertaken by the (http://cati-neuroimaging.com/) to address the requirement of the MEMENTO methodological group to embed the number of CMBs in the description of the participants of the MEMENTO cohort.

* * *

Chapter 1

CONTEXT

The aims of this chapter are to introduce cerebral microbleeds (CMBs), their clinical context and to describe their neuroimaging features and the challenges raised by their identification on magnetic resonance imaging (MRI). State-of-the-art methods that dealt with both visual and semi-automatic CMBs identification and that aimed to standardize their detection will be discussed. At the end of this chapter, the overall objectives of this PhD will be developed.

1.1 Clinical context

The goal of this section is to provide an overview on CMBs, their definition, clinical meaning and challenges related to making their identification efficient.

1.1.1 History of cerebral microbleeds

Very small vascular lesions such as cerebral microbleeds have long been impossible to see in-vivo, even standards such as catheter angiography was not sensitive enough [Gregoire, 2014]. In-vivo investigation of such lesion only was made possible with recent MRI technical progress. Sharf et al [Scharf et al., 1994] were the first to report the presence of small, intra-cerebral hyposignal on T2-weighted Fast Spin Echo (FSE) MRI sequence in patients with hypertensive cerebrovascular disease and intra-cerebral hemorrhage (ICH) at low magnetic field strength (1 Tesla), they called them «hemorrhagic lacunae». Since then, the frequent use of MRI sequences that are sensitive to magnetic susceptibility during research and clinical investigation of neurological disorders has led to the frequent detection of small, homogeneous, round foci of low signal intensity in

different populations: patients with ischemia or hemorrhagic stroke, hypertensive and healthy elderly subjects [Fazekas et al., 1999].

In 1996, at least three studies revealed strong association between ICH and CMBs on gradient-recalled-echo (GRE) T2*-weighted MRI, suggesting that CMBs may provide key information regarding the pathogenesis of ICH. Greenberg et al [Greenberg et al., 1996] reported lobar focal hypointensities in nine out of fifteen cerebral amyloid angiopathy (CAA) patients; Offenbacher et al [Offenbacher et al., 1996] described similar intra-cerebral focal hypointensities in 39 of 120 patients with spontaneous ICH; Chan et al [Chan et al., 1996] reported multifocal hypointense cerebral lesions on patients with chronic hypertension. The majority were described as homogeneous, rounded lesions with diameters varying between 2 and 5 mm, and they were named 'microbleeds'.

Later in 1999, the histopathological correlates of CMBs began to be reported. Histology-MRI correlations were studied in eleven brains of people who died after non-traumatic ICH [Fazekas et al., 1999], and in three brains of people who died from a variety of other diseases [Tanaka et al., 1999]. Sections with small hyposignals on a T2*-weighted echo plannar imaging (EPI) MRI were examined. Histological-MRI correlations demonstrated that the hypointensities detected on GRE T2* images reported as CMBs corresponded to focal deposits of *paramagnetic blood break-down products [Chavhan et al., 2009]*, especially haemosiderin, within macrophages in perivascular tissue consistent with vascular leakage of blood cells. Figure 1.1.1 shows a typical histopathological illustration of a CMB in a rat brain.

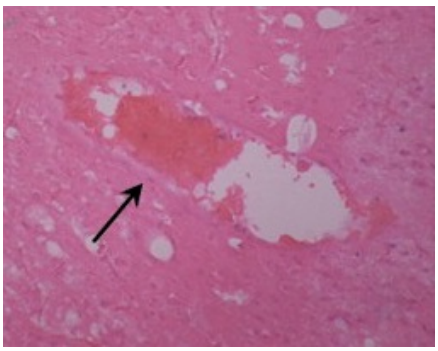

Figure 1.1.1: A typical CMB in a rat brain (arrow), magnification = ×100. Blood clots and red-cells appeared inside the CMBs [Jiang et al., 2015].

1.1.2 CMBs definition on MRI

As seen above CMBs are paramagnetic and are, thus, visible on MRI sequences that are sensitive to magnetic susceptibility differences (such as GRE T2*-weighted sequence). According to Greenberg et al. [Greenberg et al., 2009] CMBs *should be black or very hypointense on T2*-weighted MRI, round or ovoid (excluding tubular or linear structures such as those representing vessels or a resorbed macrobleed), blooming (larger or more conspicuous on GRE than Spin-Echo (SE) MRI, see Figure 1.1.2), devoid of T1- or T2-weighted hyperintensity (such as cavernous malformation), and at least half surrounded by brain parenchyma (permitting superficial CMB as seen in CAA). Other mimics such as mineralization of the basal ganglia or diffuse axonal injury are excluded based on appearance or clinical history. The size may be relatively unimportant for correctly categorizing lesions that otherwise meet these criteria and should be applied conservatively if at all.*

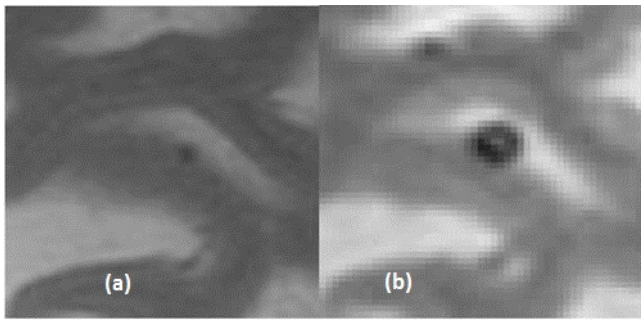

Figure 1.1.2: CMB illustration: The blooming effect is demonstrated by the larger area of signal void on the T2*-weighted MRI in (b) compared to the fast SE image in (a) [Greenberg et al., 2009].

1.1.3 Clinical relevance

CMBs has long been considered as low abundance bleeding sequelae and, thus, as asymptomatic markers of small vessel diseases. Recent interest in these lesions has increased and several MRI-pathology correlations showed that they are associated with other manifestations of small vessel disease and AD [Vernooij et al., 2008, Cordonnier et al., 2009]. The alteration of the walls of small vessels may theoretically produce steady extravasations of erythrocytes through the fragile vascular walls [Roob and Fazekas, 2000] or tiny areas of haemorrhage.

Recent research studies suggest that their origin and clinical interpretation may depends on their location [Cordonnier, 2011, Cordonnier et al., 2006]; deep CMBs are markers of hyper-

tensive arteriopathy (HTA) while those confined in the cortical-sub-cortical region are linked to cerebral amyloid angiopathy (CAA), as illustrated in Figure 1.1.3.

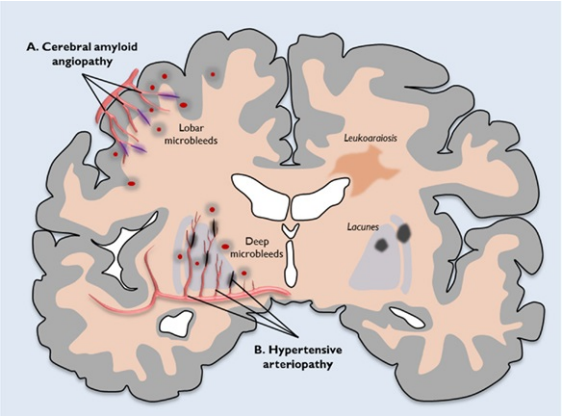

Figure 1.1.3: (A) CAA preferentially affects the small arteries and arterioles of the cerebral cortex and gray–white matter junction; (B) HTA typically affects small deep arterial [Charidimou et al., 2012].

The presence of strictly lobar CMBs has been included in the diagnostic criteria of CAA. Their association to small vessel arteriopathies (HTA and CAA) makes CMBs a valuable indicator of cerebral small vessel disease [Gregoire, 2014]. Moreover, this association suggests their implication in both hypotheses regarding the pathological process of Alzheimer's disease: those associated with HTA (deep CMBs) result of ischemia or arteriosclerosis, on the benefit of the vascular hypothesis: those associated with CAA could result from the amyloid protein deposition on the walls of blood vessels. CMBs understanding may contribute to the understanding of AD; Figure 1.1.4 illustrates how CMBs may play a prominent role in this neurodegenerative disease.

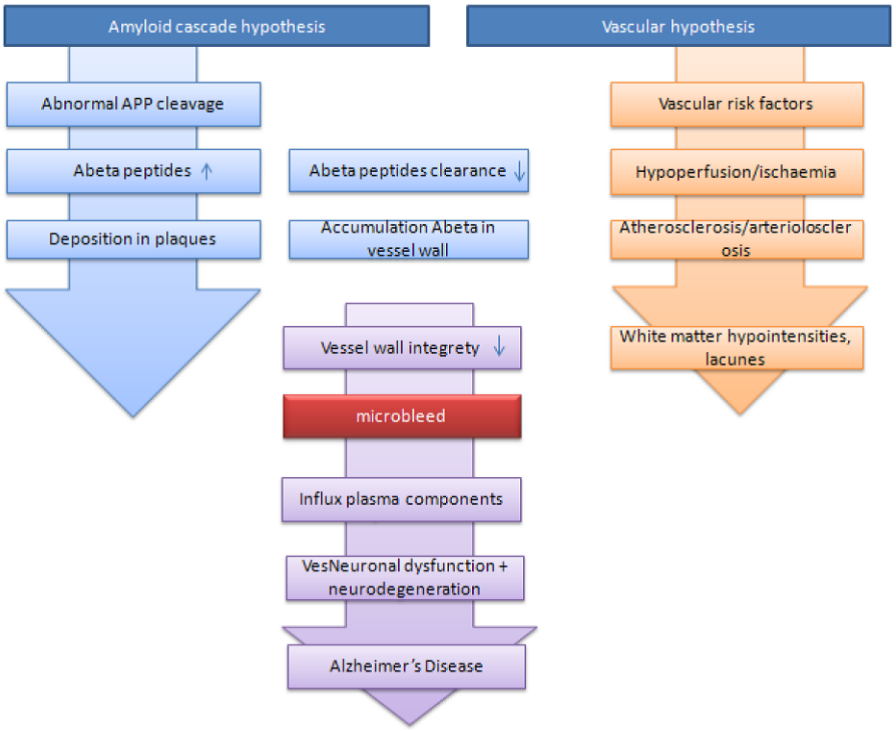

Figure 1.1.4: Proposed representation of the pathophysiological pathway of AD with a prominent role for CMBs, suggesting that they might act as a link between the two pathways. APP = amyloid precursor protein [Cordonnier, 2011].

To conclude, several studies were undertaken to determine the meaning of these hypointensities observed on MRI. CMBs are no longer considered as asymptomatic deposits in the perivascular regions. Their prevalence on MRI in the general population varies from 5% to 35% [Murao et al., 2013]. In fact, they are of special interest in the aging population and are relatively common in vascular dementia, with reported prevalence ranging between 35% and 85% [Cordonnier, 2011].

However, the understanding of CMBs etiology is rendered more difficult due to several issues. Their size is very small and only those of sufficient size can be seen on MRI. Their size is also variable and their appearance is disturbed by the blooming effect, thus leading to a larger apparent radiological size than their real size. CMBs are widespread in the brain, and can easily be missed by visual inspection. Visual CMB's rating is a time consuming procedure, limiting the number of brains with CMBs that have been analyzed in MRI-pathology correlation studies [Gregoire, 2014]. Further large, well-designed histopathological studies combined with MRI correlation are needed to characterize the range and threshold of haemosiderin pathology

required to create a CMB visible on MRI and confirm the bleeding or ischemic origin of CMBs according to the underlying arteriopathy [Gregoire, 2014].

1.2 MR magnetic susceptibility and Phase MR image

In order to better understand how CMBs can be detected on MRI, this chapter briefly reviews the physical basis of magnetic susceptibility and how it affects the signal of MRI sequences that are sensitive to magnetic susceptibility[1].

Whereas an electric charge is the basis for an electric field, an electric charge in motion produces a magnetic field. For example, a loop carrying current produces a magnetic field equivalent to the one produced by a magnetic dipole (see Figure (1.2.1)).

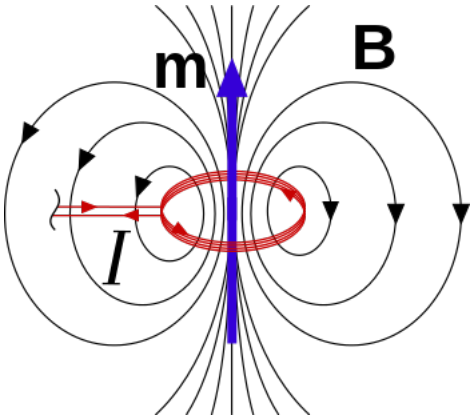

Figure 1.2.1: The magnetic field, B, and magnetic moment m, due to an electric current, I.

A magnetic dipole is a basic physical entity that acts as a source of the magnetic field [Haacke and Reichenbach, 2011]. It is defined by two poles that attract or repel one another. A magnetic dipole is characterized by a vector quantity called the *magnetic moment*, **m**. When a material is placed into a magnetic field, electrons and nucleons acquire different energy states. A physical quantity, the *spin*, is used to describe these energy states; the *spin* is proportional to the *magnetic moment* of either an electron or a nucleon. The total magnetic moment of an atom can be calculated by vector summation of the individual spins from nucleons and electrons. Since the gyromagnetic ratio[2] of an electron is several hundreds of times larger than the gyromagnetic ratio of a nucleon, the magnetic moment of an atom is usually dominated by

[1] The italic notation in this chapter stands for vectors.
[2] The ratio of its magnetic dipole moment to its angular momentum.

the overall electronic spin. Due to thermal energy at ambient temperature, the individual atom magnetic dipole moments point randomly in different directions and the resulting vector is in fact negligible in the absence of external magnetic field. However, when placed in an external magnetic field, the individual magnetic moments tend to counteract thermal effects and align with the external field, thus resulting in a macroscopic magnetic moment. If a large number of atoms contained in a given volume are considered, the magnetization can be defined as the average magnetic moments over the volume, enabling to define a property called the "magnetic susceptibility" as defined below. It can be noted that these macroscopic magnetic properties are dominated by electronic effects, and that it will produce deformation of the external magnetic field in MRI. However, most biological tissues contain predominantly water molecules, and 63% of the human body is consequently hydrogen atoms. The nuclear magnetic moments are the basis for the nuclear magnetic resonance (NMR) phenomenon: a nuclear magnetization can be produced for protons of hydrogen atoms, thus making MRI possible [Haacke and Reichenbach, 2011].

Magnetic susceptibility

Let us consider an uniform external magnetic field $B_0 = \mu_0 \cdot H$, with μ_0 the absolute vacuum permeability and H the measured field [Haacke and Reichenbach, 2011].

When a material is placed into the field B_0, the actual field B given in Tesla (T) inside the material is

$$B = \mu_0 (H + M) \tag{1.2.1}$$

where M is the induced magnetization, or the volume average of magnetic moments.

The induced magnetization M inside the material may be related to the H field by a constant χ through

$$M = \chi H \tag{1.2.2}$$

χ is called magnetic susceptibility. It implies linearity between the external field and the induced magnetization and depends on the average microscopic content. In the International System of Units (SI), M and H are measured in amperes per meter. χ is therefore a dimensionless quantity.

DIAMAGNETISM, PARAMAGNETISM, AND FERROMAGNETISM

χ is an intrinsic property of the material, reflecting the perturbations of the applied magnetic field. Most materials are classified either as diamagnetic, paramagnetic, or ferromagnetic.

At the atomic level, any two paired-electrons together in an orbital are diamagnetic electrons. Atoms with all diamagnetic electrons (paired) are called diamagnetic atoms. A paramagnetic electron is an unpaired electron. An atom is considered paramagnetic as soon as it has one paramagnetic electron. Therefore, paramagnetic materials are attracted by an applied magnetic field and yield internal, induced magnetic fields in the direction of the applied magnetic field. Diamagnetic materials create an induced magnetic field in a direction opposite to an applied magnetic field and are therefore repelled by the applied magnetic field.

If the susceptibility χ is positive, the material or the object is paramagnetic. If χ is negative, the material is diamagnetic. For vacuum, χ is zero.

Human tissues contain mostly water, thus, almost all soft tissues in the body are diamagnetic. Bone is slightly more diamagnetic than soft tissues due to its calcium content [Hopkins and Wehrli, 1997]. In MRI, it is practical to express susceptibility as "paramagnetic" or "diamagnetic" *relative to the susceptibility of water* or a reference tissue, rather than that of vacuum. Indeed, differences with tissues appear more clearly, and, as a volume property, it then relates to differences in content as compared to water or a reference tissue. Some examples of magnetic susceptibilities of a few biological tissue are given in Table 1.2.1. Manganese, iron (Fe^{2+} and Fe^{3+}) and gadolinium (Gd^{3+}) are some examples of paramagnetic ions [Haacke and Reichenbach, 2011]. Molecular oxygen is also slightly paramagnetic. The addition of a given paramagnetic substance to a tissue will result in a small change in the volume susceptibility. To account for the change of susceptibility for a given amount of paramagnetic subtance,$[S]$, added to water or tissue, the molar susceptibility, χ_m, can be defined, and the resulting suceptibility is then:

$$\chi_{[S]} = \chi_{[S]=0} + \chi_m \times [S] \tag{1.2.3}$$

χ_m is measured in $m^3 \cdot mol^{-1}$ (SI) or $cm^3 \cdot mol^{-1}$ (CGS (Centimetre–gram–second system of units)).

Tissue	Magnetic susceptibility
Cortical bone	-12.82×10^{-6}
Lipids	-10×10^{-6}
Hemoglobin protein (without Fe ions)	-9.91×10^{-6}
Pure water	-9.05×10^{-6}
Fully deoxygenated whole blood	-7.9×10^{-6}
Fully deoxygenated red blood cell	-6.56×10^{-6}
Ferritin	$+520 \times 10^{-6}$

Table 1.2.1: Magnetic Susceptibilities of a few biological Tissue [Haacke and Reichenbach, 2011] in SI. This value is devided by 4π to obtain the dimensionless CGS value of volume susceptibility.

As can be seen, iron, that can be found in various forms in the body such a ferritin or paramagnetic ions in blood products, will induce important susceptibility variations in tissues.

MRI basics

Though it is a recent technology (introduced by Lauterbur in 1973 [Lauterbur, 1973]) as compared to other medical imaging techniques, MRI has a wide range of applications in medical diagnosis and over 25,000 scanners are estimated to be in use worldwide. It is considered as non-invasive without known side effects by itself.

MRI relies on the nuclear magnetic resonance principle, that relates to the ability that have some nuclei to absorb energy of an electromagnetic field on resonance (or photons with a given specific energy). The resonance condition relates to the energy level difference between the microscopic nuclear spin states. When a sample is placed in a static magnetic field B_0, its magnetic moments align themselves with the direction of B_0 resulting in an average nuclear magnetization. This magnetization M is thus oriented in the longitudinal direction (z) as schematically illustrated in Figure 1.2.2 (b) for a spin $1/2$ nucleus such as the one of hydrogen. The nuclear magnetization can thus absorb energy from an electromagnetic field at specific frequencies: for a spin $1/2$, the angular velocity of M around B_0, which is called the Larmor angular frequency, ω and given by

$$\omega = -\gamma \cdot B \tag{1.2.4}$$

where γ is the gyromagnetic ratio of the nucleus. The gyromagnetic ratio of hydrogen nucleus is $\gamma = 2.675.10^8\, rd/T$, and in practice clinical magnetic fields are between 1.5T and 7T leading to the Larmor frequencies in the radiofrequency (RF) range.

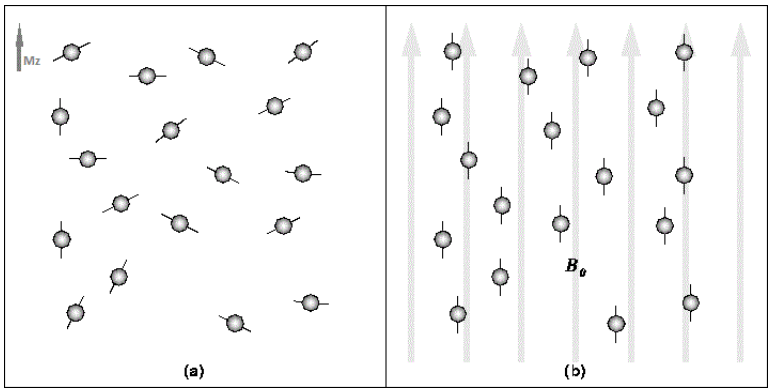

Figure 1.2.2: In the absence of B_0, hydrogen nuclei are randomly oriented as in (a). With B_0 applied, the hydrogen nuclei precess about the direction of the field as in (b), from http://www.mr-tip.com.

A semi-classic vector representation for spin 1/2 can be used, leading to the Bloch equation describing how the nuclear magnetization react to a magnetic field:

$$\frac{dM}{dt} = \gamma M \times B \tag{1.2.5}$$

During the excitation period, a radiofrequency field, B_{rf}, is applied perpendicular to B_0 at the Larmor frequency ω (see Figure 1.2.3 (a)), the magnetization deviates away from B_0 as illustrated in Figure 1.2.3 (b). The resulting excitation angle between the main field B_0 and the magnetization is called the flip angle.

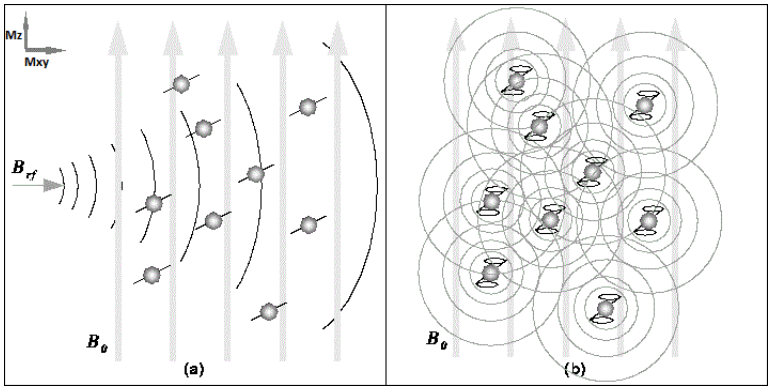

Figure 1.2.3: The RF pulse, B_{rf}, causes the net magnetic moment of the nuclei, M, to tilt away from B_0as in (a). When the RF pulse stops, the nuclei return to its equilibrium parallel to B_0. During realignment, the nuclei lose energy that can be measured, from http://www.mr-tip.com.

When switching off B_{rf} after the excitation, a relaxation phenomenon occurs. This reflects

the return to equilibrium of tissue magnetization during which the nuclei lose energy as a measurable signal; In response to the force bringing them back to their equilibrium orientation, the protons undergo a rotating motion "precession", much like a spin wheel under the effect of gravity. These effects are formally described by the Bloch equations with relaxation:

$$\frac{dM}{dt} = \gamma M \times B - \frac{M_{xy}}{T2} + \frac{(M_0 - M_z)}{T1} \tag{1.2.6}$$

where T1 is the longitudinal relaxation time and T2 the tranverse relaxation time, M_z the longitudinal component (along B_0) and M_{xy} the tranverse component.

These temporal changes in magnetization Mxy induce a time-varying magnetic flux, and an induced current at the Larmor frequency in a receiver coils at the origin of the MR signal. The frequency at which protons resonate depends on the strength of the local magnetic field in the imaged volume. This signal is referred to as the free-induction decay (FID), see Figure 1.2.4.

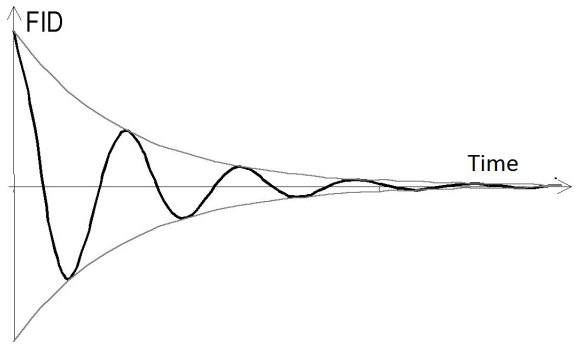

Figure 1.2.4: Free-induction decay (FID) signal [Chupin, 2004].

The FID response signal is measured by induction using a conductive coil placed around the object and describes how the transverse magnetization M_{xy} changes with time. The evolution during the relaxation period for both transverse M_{xy} and longitudinal M_Z components is illustrated in Figure 1.2.5.

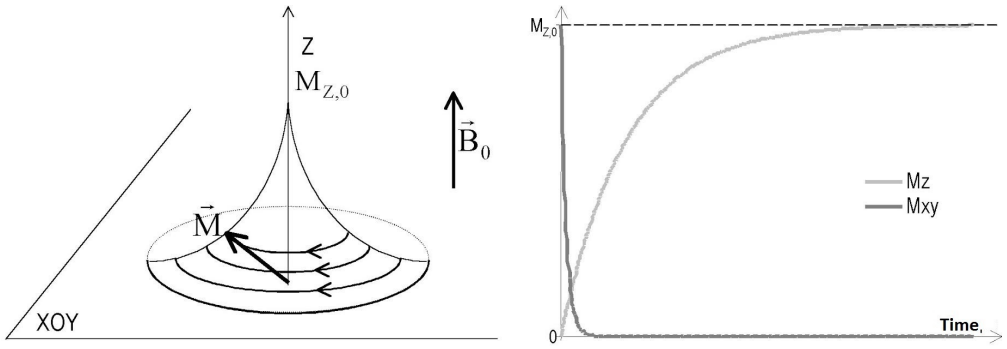

Figure 1.2.5: Representation of M when B_{rf} is switched of. Visualization of M's component : transverse "Mxy" and longitudinal "Mz" [Chupin, 2004].

The process associated with the time parameter T1, is responsible for the recovery of the longitudinal magnetization, M_Z. T1 is the characteristic time required for nuclei in the sample to realign to initial magnetization with an exponential decay. It is also called the "spin-lattice relaxation time", as it relates to local energy exchange with all the surrounding tissue. After a time of T1, M_Z will recover 63% of its steady state value. The other relaxation process, associated with the characteristic time T2, is accounting for the exponential decay of the transverse magnetization, M_{xy}. It is also called the spin-spin relaxation time to account for interactions between dipoles: the nuclei lose their phase coherence because of their proximity which results in a loss of M_{xy} faster than T1. In the relaxation period, after a time T2 transverse magnetization has lost 63% of its amplitude.

It is to be noted that the main magnetic field is never perfectly homogeneous and inhomogeneities may result either from intrinsic defects in the magnet itself or from susceptibility-induced field distortions produced by the tissue or other materials placed within the field. Correcting these inhomogeneities cannot be done perfectly. This inhomogeneous field results in inhomogeneous frequencies at the scale of the imaged volume and the transverse magnetization apparently decays faster than would be predicted by T2; to account for this faster apparent relaxation, an apparent relaxation time T2*[3] is introduced. T2* is thus always smaller than or equal to T2 as illustrated in Figure 1.2.6.

[3] T2* ="T2-star".

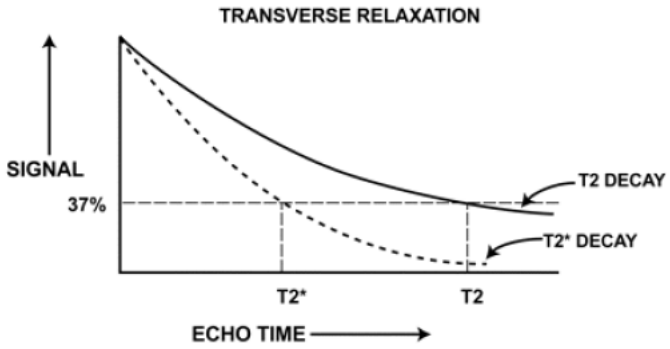

Figure 1.2.6: Illustration of the difference between T2 and T2* decay with $T2^* < T2$ [Chavhan et al., 2009]

relaxation times T1 and T2 mainly depend on molecular mobility. Structured materials, such as bone and other hard tissues, have very fast relaxation times while in contrast soft tissues have higher water mobility and longer relaxation times. The following table shows typical T1 and T2 relaxation times for some brain tissues at 1.5 T.

	T1 (ms)	T2 (ms)
Water	3000	3000
Gray matter	810	100
White matter	680	90
Liver	420	45
Fat	240	85

Table 1.2.2: T1 and T2 relaxations times for brain tissues at 1.5T.

Additionally the water distribution in soft tissues gives the possibility to distinguish between them through these relaxation constant. The subtle differing characteristic of different tissues (T1, T2 and proton density (PD)) are the origin of contrast in MRI images. T1 and T2 contrast mechanisms are illustrated in Figure 1.2.7.

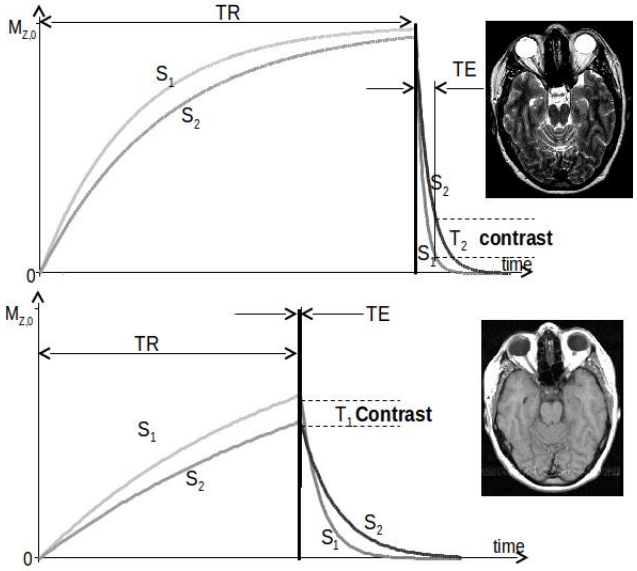

Figure 1.2.7: T1 and T2 contrast illustration in a typical spin-echo sequence. Top graph illustrates the T2 contrast that depends on TE. Bottom image illustrates the T1 contrast that depends on the repetition time TR [Chupin, 2004].

To generate contrasted images, RF pulses are applied and the signal measured according to a predefined sequence with experimentally defined times, the repetition time (TR) and the echo time (TE). TR is the time between two repeated excitations. It enables to measure how much longitudinal magnetization recovers between each pulse (see Figure 1.2.7). TE is the time between the RF pulse and the signal recording time, it enables to measure signals with selected T2 relaxation (see Figure 1.2.8).

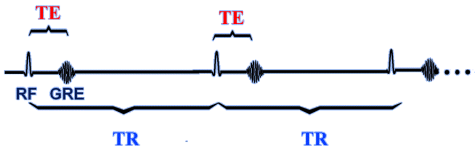

Figure 1.2.8: Operator-selected pulse sequences parameters: time echo (TE) and time repetition (TR).

To obtain a T1-weighted images mainly characterized by differences in T1 properties, a short TR and a short TE (TR $<$ 1000msec, TE $<$ 30msec) is needed, see Figure 1.2.7 (b). To obtain a contrast dominated by T2, or a T2-weighted image mainly characterized by differences in T2 relaxation, a long TR and a long TE (TR $>$ 2000msec, TE $>$ 80msec) are used, see Figure 1.2.7 (a). A proton density PD sequence is based on a long TR and a short TE to render the influence

of relaxation times negligible with regard to PD.

Localization principles

The relaxation principles have been presented regardless of localization. To generate an image, localization principles are needed. MRI consequently uses *spatial encoding* methods to divide the sample into voxels[4]. Three major principles are the slice selection, the readout encoding, and the phase encoding that are combined in imaging sequences. Generally speaking, to localize signals the magnetic field is changed spatially. This is performed using the so called 'gradients', or the spatial derivative of the magnetic field along B0. The gradients can be represented as a vector to account for the 3 components of the spatial derivation along x, y, and z of the magnetic field. The gradients can then be applied in any direction and changed rapidly during an imaging sequence. Changing spatially the magnetic field has the effect of changing the resonance frequency in proportion, which is the basis of localization principles in MRI.

For the slice selection, a slice selection gradient G_s is used to select the anatomical volume of interest. By applying G_s, nuclei experience a different magnetic field strength dependent on their position along that gradient. A frequency selective RF pulse is applied at the same time, thus only flipping the magnetization within this slice. When this B_{rf} pulse is applied with a frequency $[\omega \pm \delta\omega]$, only the nuclei experiencing the corresponding magnetic field will be excited, resulting in the first partition of voxels. Within this slice, the position of each point will then be encoded in the two remaining dimension.

The second localization principle is the readout gradient, or frequency encoding gradient G_f. When applied perpendicularly to the slice encoding gradient and after the excitation, it results in a change of Larmor frequencies in this direction. The acquired signal thus contains different frequencies: an analysis of the frequency content using a Fourier transform thus provides an amount of signal as a function of position along the readout gradient.

The third localization principle is to apply a phase encoding gradient,G_p in the third direction. It modifies the spin resonance frequencies, inducing dephasizing, which persists after the gradient is interrupted. This results in all the protons precessing at the same frequency but with different phases. This sequence is then repeated with different gradient G_p, resulting in different accumulated phases and leading to a discrete Fourier encoding. After a Fourier

[4] volume elements

transform among this phase encoding dimension, localization is then obtained.

These principles are illustrated in the following section detailing the gradient-echo imaging sequence.

Gradient Echo Imaging and k-space

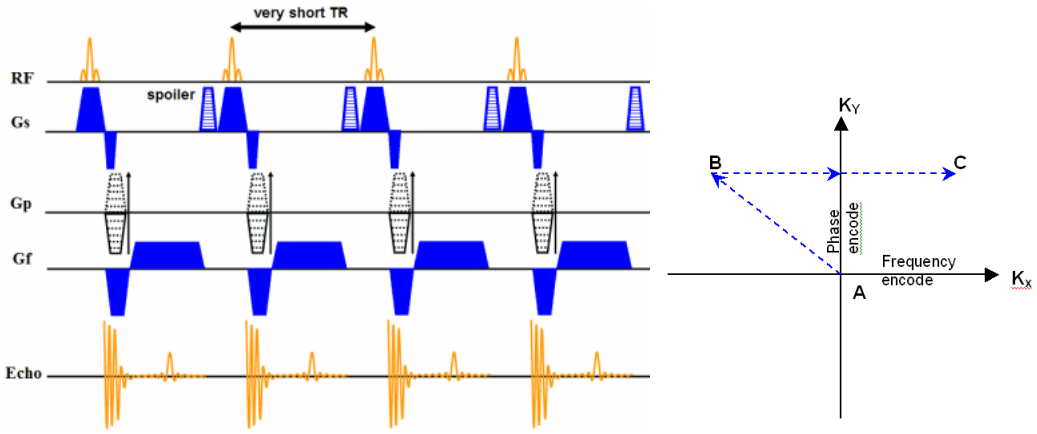

Figure 1.2.9: 2D pulse sequence diagram of a generic spoiled gradient echo sequence. RF radio frequency selective pulse tilting the magnetization with a given flip angle within a slice, G_s the slice selection gradient, G_p the phase encoding gradient, G_f the frequency encoding gradient. Corresponding k-space is illustrated in the right, from http://www.mr-tip.com.

The gradient recalled echo (GRE) MRI sequence is considered the simplest sequence in MRI. Figure 1.2.9 illustrates a generic spoiled 2D single-echo gradient echo sequence. An asymmetric bipolar readout gradient (which is the same as the frequency-encoding gradient) is required to create an echo (a gradient-echo in this case). Each cycle (TR) record one line of data in k-space with different steps[5] as follows:

1. GRE sequence starts with the B_{RF} producing a flip angle of between 0 and 90 degree: a flip angle lower than 90°, results in a faster recovery of longitudinal magnetization that allows shorter TR/TE and acquisition time.

2. A slice selection gradient G_s is applied together with the RF pulse.

3. A phase encoding gradient G_p is applied simultaneously to a dephasing G_f to phase spins at the center of the acquisition period; this ensure translation from the center of k-space from A to B in Figure 1.2.9.

[5] The term "k-space" refers to a temporary memory of the space covered by the phase and frequency encoding data.

4. When switching the polarity of G_f, spins are rephased ; Nx data points are equidistantly sampled from B to C via the center of k-space during the readout step.

5. Note that an extra slice gradient is applied before the next RF pulse. It is called the "spoiler" and aims to destroy residual transverse magnetization to prepare the next cycle.

6. The excitation is then repeated as many times as necessary (Ny) to fill the raw data matrix along the direction G_p.

The k-space concept is essential in MRI. It relates to the amount of dephasing that the magnetization acquires subject to the gradients. Considering the case of 2D encoding, we have:

$$k_x = \frac{\gamma}{2\Pi} \int_0^t G_f \cdot d\tau \tag{1.2.7}$$

and

$$k_y = \frac{\gamma}{2\Pi} \int_0^t G_p \cdot d\tau \tag{1.2.8}$$

The measured signal can be expressed as:

$$s(k_x, k_y) = Constant \times \iint (\rho(x, y) \times \exp(2\Pi i(k_x x + k_y y))) \, dxdy \tag{1.2.9}$$

Fourier transform is then used to transform the measured k-space complex data $s(kx, ky)$ into image space $\rho(x, y)$. This image data is then manipulated for different clinical utility, and with TR and TE to provide the desired contrast. For example, a magnitude image is used to provide the desired contrast, while phase images can be used to measure flow or magnetic field. The resulting complex signal can be written as

$$\rho(\theta) = \rho_m(\theta) \exp(-i\triangle\varphi) \tag{1.2.10}$$

where $\rho_m(\theta)$ is the magnitude given by

$$\rho_m(\theta) = \rho_0 \sin\theta \exp\left(\frac{-TE}{T2^*}\right) \times {}^{[1-\exp(\frac{-TR}{T1})]}/_{[1-\cos\theta \exp(\frac{-TR}{T1})]} \tag{1.2.11}$$

If the local magnetic field is not homogeneous, the local frequency varies by $\triangle\omega$, and $\triangle\varphi$ represents the accumulated dephasing after a time TE:

$$\triangle\varphi = \triangle\omega \, TE \tag{1.2.12}$$

GRE Phase MR image and its relationship to susceptibility

MRI provides a complex image, with an amplitude and a phase. Amplitude image can be modulated to generate contrast. The phase image is more complex to analyze and has thus been discarded from MR-based analysis till recently. Generally speaking, the phase describes the orientation across time of the magnetization vector in the transverse plane, see Figure 1.2.10. MR signal is received using a quadrature detection, which results in two data streams with a 90° phase difference. The digitized values from these signals are the *real* part and the *imaginary* part of each complex data point in k-space. Magnitude and phase images result from the Fourier transform of data and are defined as $\sqrt{x^2+y^2}$ for the magnitude and as $\tan^{-1}\left(\frac{y}{x}\right)$ for phase image. As presented in the previous section, the phase can provide information on the local magnetic field.

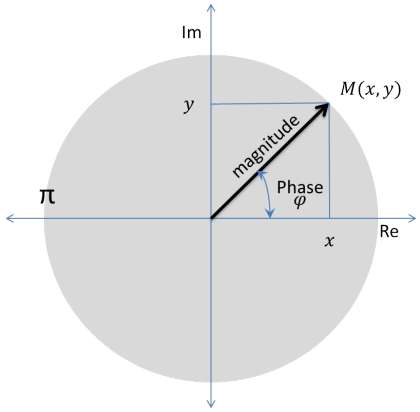

Figure 1.2.10: Magnitude and phase illustration in complex representation

An example of a T2* magnitude image and corresponding phase image as given by MRI reconstruction for a gradient echo sequence is provided in Figure 1.2.11.

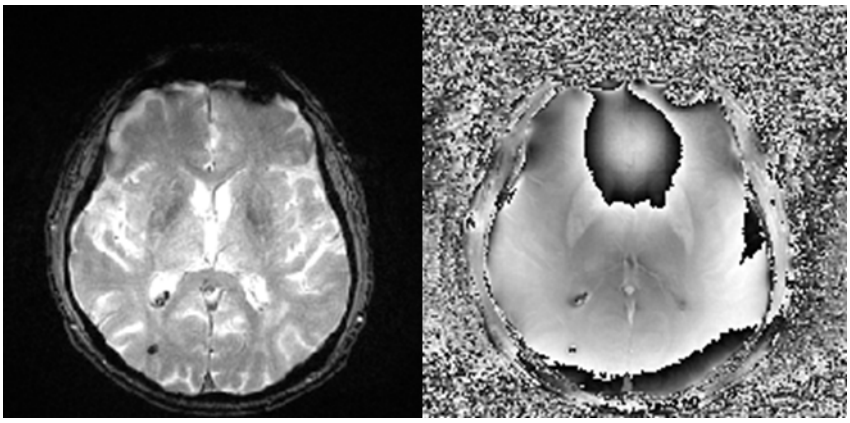

Figure 1.2.11: Example of magnitude T2* image and corresponding phase image, from MEMENTO dataset used in this work [Kaaouana et al., 2015]. The signal amplitude (left) provides a T2* contrast with hyper-signals for CSF, isosignal for WM and GM and hyposignals for susceptibility inclusions. The phase image relates to magnetic field inhomogeneity that is especially inhomogeneous around susceptibility inclusions.

From the Larmor equation, the relationship between the magnetic field B and the dephasing $\triangle\varphi$ is given by

$$\triangle\varphi = -\gamma \triangle B\, TE \tag{1.2.13}$$

since

$$\triangle B = g \triangle \chi B_0 \tag{1.2.14}$$

where g is a geometric factor depending on the susceptibility distribution [Hoffman, 2006]. Consequently, the relationship between dephasing, local susceptibility variation and magnetic field B_0 can be written as

$$\triangle\varphi = -\gamma g \triangle \chi\, B_0\, TE \tag{1.2.15}$$

$\triangle\varphi$ is dependent on the local tissue susceptibility.

Susceptibility artifact in MRI

If we consider an applied magnetic gradient G_x, the field at a position x is given by:

$$B\,(x) = B_0 + G_x \cdot x \tag{1.2.16}$$

the corresponding Larmor frequency using previous equation is given by:

$$\omega(x) = -\gamma(B_0 + G_x \cdot x) \tag{1.2.17}$$

When the magnetic field is disturbed by the presence of a magnetic material, the net precession frequency of the spins in or around the material is influenced not only by the applied gradient field, but also by the field $\triangle B$, induced by the material and ω becomes:

$$\omega(x) = -\gamma(B_0 + \triangle B(x) + G_x \cdot x) \tag{1.2.18}$$

$$\omega(x) = -\gamma\left(B_0 + G_x \cdot \left(x + \frac{\triangle B}{G_x}\right)\right) \tag{1.2.19}$$

or

$$\omega(x') = -\gamma(B_0 + G_x \cdot x') \tag{1.2.20}$$

where

$$x' = x + \frac{\triangle B}{G_x} \tag{1.2.21}$$

Consequently, as the spins now precess with an angular frequency $\omega(x')$ (rather than $\omega(x)$), the spins influenced by $\triangle B(x)$ are mapped to an incorrect location x' (instead of x) during image reconstruction thus causing distortion. More specifically, this issue can be detected in areas with strong magnetic susceptibility difference [Haacke and Reichenbach, 2011]. An example is illustrated in Figure 1.2.12.

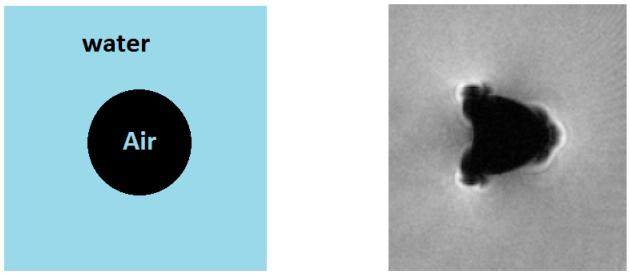

Figure 1.2.12: Demonstration of the effect of magnetic susceptibility of a cylindrical water/air interface; distortions and intensity loss in the GRE acquired image: B_0 = 7T, TR / TE = 500/15 ms, matrix = 256 x 256 [Belaroussi, 2005].

Along time, these spins get out of phase with each other. At the voxel level, phase dispersion within a voxel results in a decrease of the net signal of that voxel because of T2* dephasing. Therefore, geometric measurement in gradient echo MRI and its derivatives (including T2*W, SWI) fundamentally suffer from inherent *blooming artifacts*: haemosiderin deposits exert a high susceptibility effect on the local magnetic field, which results in a larger area of signal loss.

1.3 State-of-the-art: identification and detection of CMBs

In this section, we will first introduce different imaging techniques used for CMBs identification and then, describe the two proposed visual rating scales and state-of-the-art automatic methods used for CMBs identification.

1.3.1 CMBs imaging techniques

In order to better identify CMBs, new MRI sequences and reconstruction techniques were proposed, as described below.

T2*-weighted GRE T2*-weighted gradient recalled-echo (GRE) sequence has a high sensitivity for differences in magnetic susceptibility and is the most commonly used for CMBs detection as illustrated in (a) on Figure 1.3.1 (a). However, CMB identification is very sensitive to MRI sequence parameters such as field strength, slices thickness, TE, interslice gap, TR, flip angle or matrix size. A higher field strength allows higher resolution and more susceptibility effect, but rating may become barely feasible. Longer TEs enhance susceptibility effects but also other susceptibility artifacts and may thus hamper identification of CMBs near air-tissue interfaces. Interslice gap needs to be chosen carefully with respect to CMBs size, as some can be missed if the interslice gap is too large.

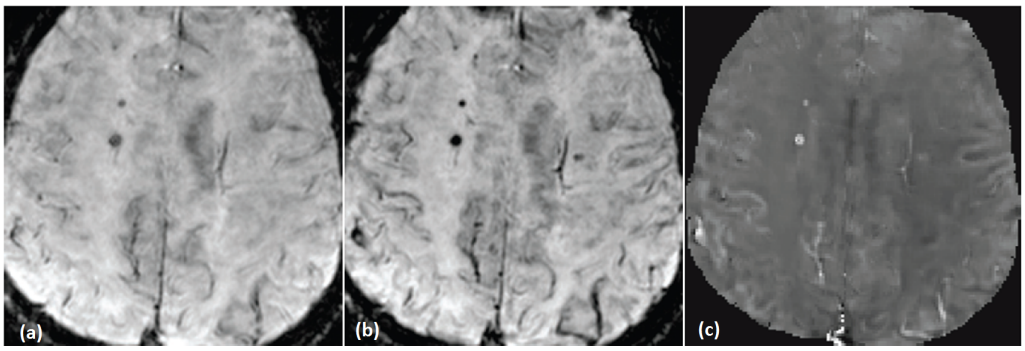

Figure 1.3.1: The same CMBs are shown at TE=38.7ms on T2*W (a), SWI (b) and QSM (c) [Liu, 2011].

Susceptibility weighted imaging (SWI) The sequence used for susceptibility weighted imaging (SWI) is based on a high resolution 3D gradient-recalled echo T2*-weighted sequence with a long echo time. In SWI, both magnitude and phase maps are combined in post-processing to create the «susceptibility-weighted» image. In this processing, thin section magnitude images are multiplied several times by a high-pass filtered phase images. This process increases the contrast between paramagnetic substances (such as CMBs) and surrounding tissue, as can be seen on Figure 1.3.1 (b). The visibility of CMBs and cerebral blood vessels (which contain paramagnetic deoxyhaemoglobin) is further enhanced by the generation of minimal intensity projection (mIP) over a number of slices [Haacke and Reichenbach, 2011]. SWI is very sensitive to susceptibility effects because of the combined T2* and phase inhomogeneity contrast. It is thus very sensitive to sequence parameters such as echo time TE and voxel size, and it increases with the magnetic field strength B0 leading to an enhanced sensitivity at higher field. The main advantageous result of SWI is an enhanced contrast as compared to T2* leading to a facilitated visual detection of magnetic susceptibility inclusions.

Quantitative susceptibility mapping (QSM) Quantitative susceptibility mapping (QSM) [de Rochefort et al., 2010b] is an advanced post-processing technique based on the analysis of the phase images that aims at quantifying susceptibility by solving an inverse problem. The inverse problem of QSM is to recover the susceptibility distribution of the human body from the measured local magnetic field inhomogeneity that is expressed by the convolution of the susceptibility distribution with the magnetic field generated by a unit dipole. The inverse problem is ill-posed due to the presence of zeros on a cone in the Fourier representation of the

unit dipole kernel. Liu et al [Liu et al., 2012] were the first to investigate the feasibility of characterizing CMBs using QSM and suggested to use total (TS) instead of CMBs size since TS is not sensitive to echo time and field strength, while apparent size is. The main advantages of QSM in the context of CMB quantification compared to T2*-weighted or SWI approaches are that noise decreases as TE increases (up to the limit of T2*) and that it provides a quantitative index directly linked to the total amount of paramagnetic substance. However, this technique is still under investigation and not yet suitable for clinical routine. For illustration, a QSM map showing CMBs is given in (c) Figure 1.3.1.

Comparison between imaging techniques Several studies demonstrated that SWI is more sensitive to detect CMBs than conventional gradient-echo T2* sequences [Nandigam et al., 2009], and that currently SWI is the most sensitive technique to visualize CMBs in-vivo [Ayaz et al., 2010]. Contrast enhancement provided by SWI can make the very small CMBs visible [Schrag et al., 2010] compared to conventional GRE T2* MRI [Nandigam et al., 2009]. In fact, phase is very sensitive to susceptibility differences and offers the ability to differentiate between blood products, which are paramagnetic, and calcification or mineralization, which are diamagnetic [de Rochefort et al., 2008].

Although there has been general agreement on the radiological properties of CMBs on T2* GRE images, the emergence of new MRI techniques made it possible to improve CMBs detection but also led to extend MRI criteria for identifying CMBs. As a result, there is a lack of standardized specific criteria for various MRI techniques. Many research units have used in-house CMB rating methods, and although reliability has been reported, the exact methods used (detailed CMB definition criteria, anatomical boundaries, etc.) have usually not been fully described. A standardized approach with clearly described criteria for CMBs and their anatomical location would make it feasible to improve reliability and compare results from different centers.

1.3.2 Visual identification

As CMBs are made of paramagnetic substance, sequences sensitive to susceptibility effects provide a unique tool for their in-vivo detection. However, there is yet no consensus regarding the methods used for their detection. To address that issue, investigators have compared a wide

variety of MRI sequences and designed visual scales rating for CMBs to better standardize their identification.

Rating scales

A CMB rating scale should provide a uniform rating methodology (including clear definition of CMB detection criteria and anatomical regions) and enable reliable and reproducible data collection to allow more informative cross-study comparisons. Two visual scales have been proposed: MARS (The Microbleed Anatomical Rating Scale) see Figure 1.3.2 [Gregoire et al., 2009] and BOMBS (Brain Observer Microbleed Scale) see Figure 1.3.3 [Cordonnier et al., 2009]. The main difference between both is that MARS classify CMBs into individual lobar region as well as deep structures. Both were designed for clinical practice on T2* GRE weighted images and aimed at characterizing the number of CMBs and their distribution in the brain. The first part is a guidance for use, a reminder of the definition criteria for CMBs and CMBs mimics. The second part is a table for anatomical categorization (cerebellum, thalamus...) indicating in each case if there is a definite or possible CMB. MARS had higher reliability for deep CMBs ($\kappa = 0.71$ Vs $\kappa = 0.54$). In general, MARS has better inter rater-reliability ($\kappa = 0.68\,[95\%\,CI\,0.58 - 0.78]$) and intra rater reliability ($\kappa = 0.85\,[95\%\,CI\,0.77 - 0.93]$) compared to BOMBS.

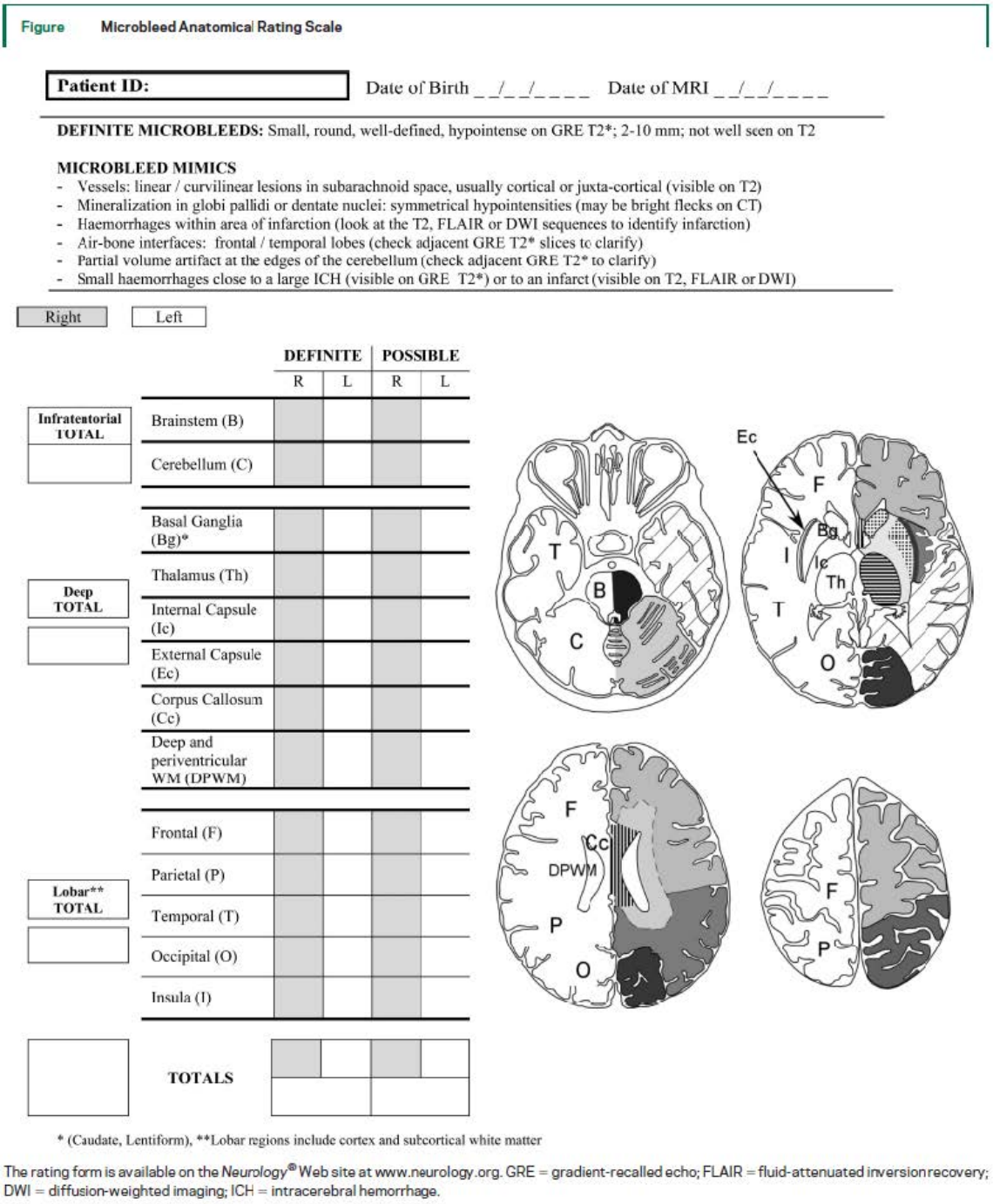

Figure Microbleed Anatomical Rating Scale

Patient ID: Date of Birth _ _/_ _/_ _ _ _ Date of MRI _ _/_ _/_ _ _ _

DEFINITE MICROBLEEDS: Small, round, well-defined, hypointense on GRE T2*; 2-10 mm; not well seen on T2

MICROBLEED MIMICS
- Vessels: linear / curvilinear lesions in subarachnoid space, usually cortical or juxta-cortical (visible on T2)
- Mineralization in globi pallidi or dentate nuclei: symmetrical hypointensities (may be bright flecks on CT)
- Haemorrhages within area of infarction (look at the T2, FLAIR or DWI sequences to identify infarction)
- Air-bone interfaces: frontal / temporal lobes (check adjacent GRE T2* slices to clarify)
- Partial volume artifact at the edges of the cerebellum (check adjacent GRE T2* to clarify)
- Small haemorrhages close to a large ICH (visible on GRE T2*) or to an infarct (visible on T2, FLAIR or DWI)

Right Left

		DEFINITE		POSSIBLE	
		R	L	R	L
Infratentorial TOTAL	Brainstem (B)				
	Cerebellum (C)				
Deep TOTAL	Basal Ganglia (Bg)*				
	Thalamus (Th)				
	Internal Capsule (Ic)				
	External Capsule (Ec)				
	Corpus Callosum (Cc)				
	Deep and periventricular WM (DPWM)				
Lobar** TOTAL	Frontal (F)				
	Parietal (P)				
	Temporal (T)				
	Occipital (O)				
	Insula (I)				
	TOTALS				

* (Caudate, Lentiform), **Lobar regions include cortex and subcortical white matter

The rating form is available on the *Neurology*® Web site at www.neurology.org. GRE = gradient-recalled echo; FLAIR = fluid-attenuated inversion recovery; DWI = diffusion-weighted imaging; ICH = intracerebral hemorrhage.

Figure 1.3.2: Microbleed Anatomical Rating Scale [Gregoire et al., 2009]

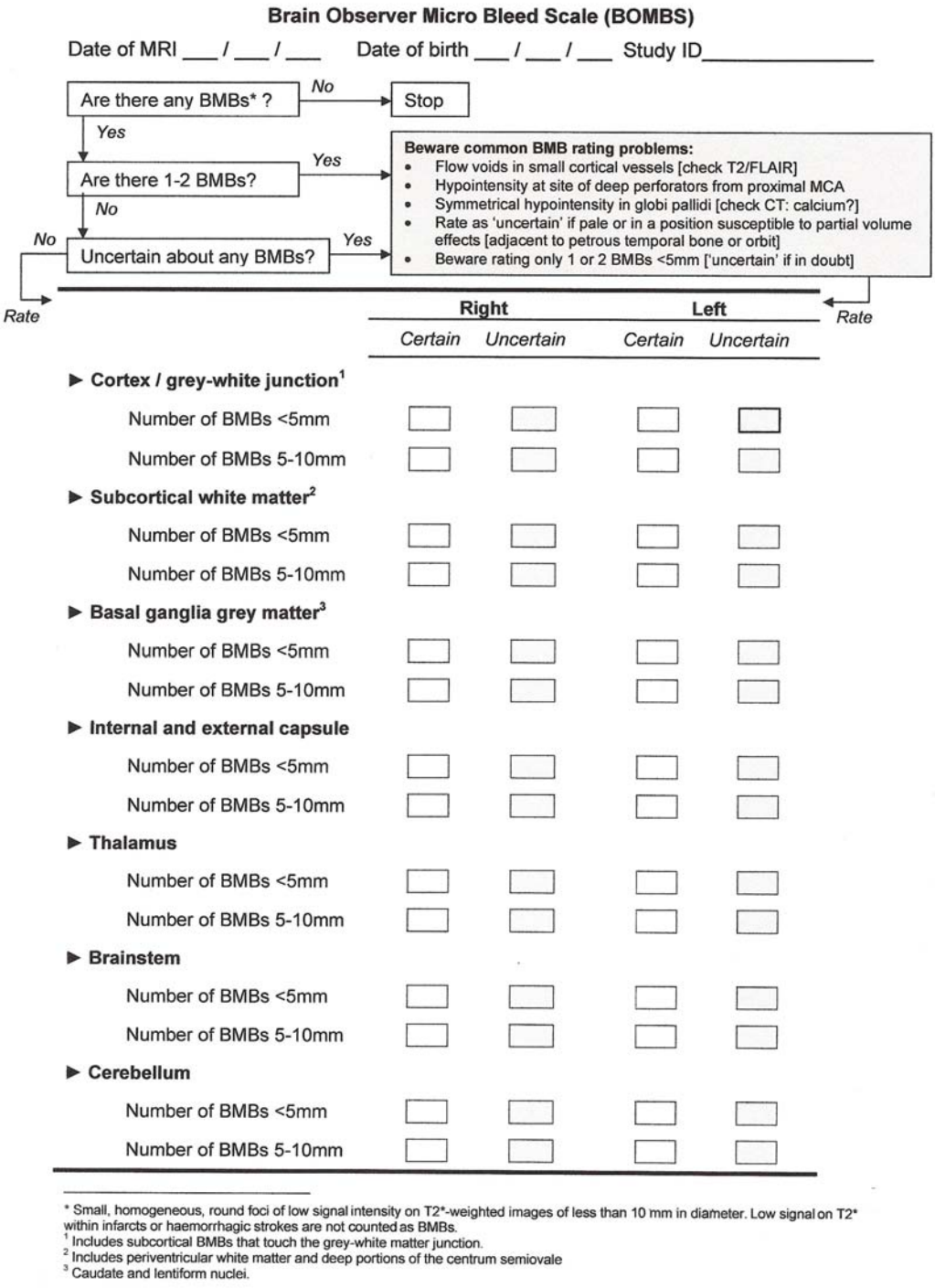

Figure 1.3.3: Brain Observer Micro Bleed scale (BOMBS) [Cordonnier et al., 2009]

1.3.3 Fully/semi automatic identification

Despite of the numerous efforts dealing with brain lesions segmentation and promising results in neuroimaging community, only few segmentation methods dedicated to CMBs have been proposed in the literature. In this section, we will briefly review existing methods for the automatic/semi automatic detection of CMBs.

Atlas based method [Seghier et al., 2011]

Method The first method dealing with CMBs automatic detection, called MIDAS for Microbleed Detection Using Automated Segmentation, was proposed by Seghier et al [Seghier et al., 2011]. It consists of an atlas based segmentation step followed by manual removal of resulting false positives. The segmentation step is an intensity-based statistical classification algorithm included in the framework of the «unified segmentation» [Ashburner and Friston, 2005] available in the SPM software (Statistical Parametric Mapping), available on the website «http://www.fil.ion.ucl.ac.uk/spm/».

The unified segmentation combines registration to a standard template, tissue classification and intensity bias correction in an iterative process that maps voxelwise probabilities of brain tissues/structures such as gray matter (GM), white matter (WM) and cerebral spinal fluid (CSF). It is based on the prior information of an atlas built into a standard space and provided by the MNI (Montreal Neurological Institute) introduced in a Bayesian model allowing the evolution of these maps. It was proposed for 3D T1 weighted datasets with nearly isotropic spatial resolution. In MIDAS, the challenge was to adapt this prior to T2* acquisitions with anisotropic resolution ($0.9x0.9x5mm^3$). The intensity of each brain tissue was modeled by one or more Gaussian(s) (Gaussian Mixture Model). SPM8 software offers the possibility to segment six classes of "tissue": WM, GM, CSF, skull, skin and other (image background). MIDAS introduced; a new class defined for CMBs (see Figure 1.3.4). For the extra CMBs class, prior information was first only based on location, and probability was initialized to 0.1 in the brain parenchyma and zero elsewhere. During the first iteration, constrains on the mixture of Gaussians was optimized using the "expectation-maximization" algorithm; this was achieved by forcing the mean of the Gaussians modeling the 6 tissue classes to be maintained at a specific range. The limiting values of these ranges are empirically chosen to discriminate each class.

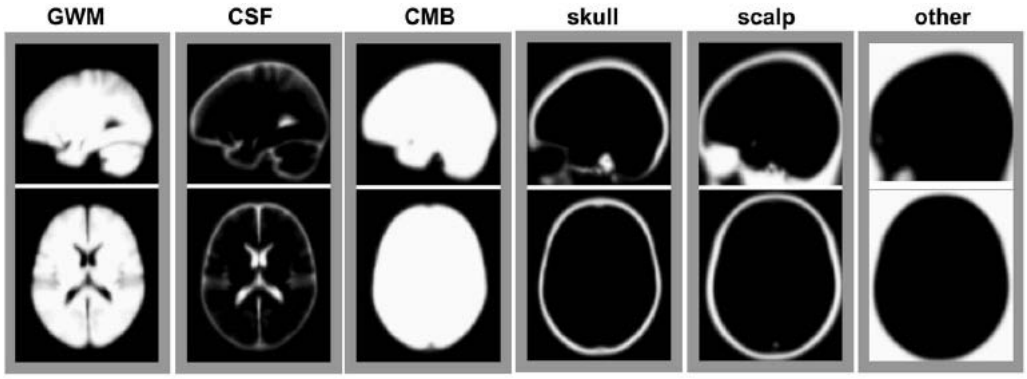

Figure 1.3.4: Illustration of the six tissue priors used in MIDAS during the first iteration of unified normalization-segmentation. GWM = gray and white matter, CSF = cerebro-spinal fluid, CMB = cerebral microbleeds [Seghier et al., 2011].

Before the second iteration of the «unified segmentation», several morphological operations were applied to distinguish CMBs from their mimics (see Figure 1.3.5)

1. Binarization of CMBs class by applying an empirical threshold;
2. Granulometry: size distribution to select round structures with a diameter between 4 and 10 mm;
3. Applying a mask calculated using different resulting maps to exclude the skull, the skin, the image's background and CSF;
4. Applying a «revised» mask to remove false positives: this mask is created from 44 control datasets that underwent the iterative process and identified points as CMBs has been labeled as «false positives». This step eliminates specially susceptibility artifact at the air-bone interfaces (sinuses) or some calcification of the basal ganglia.

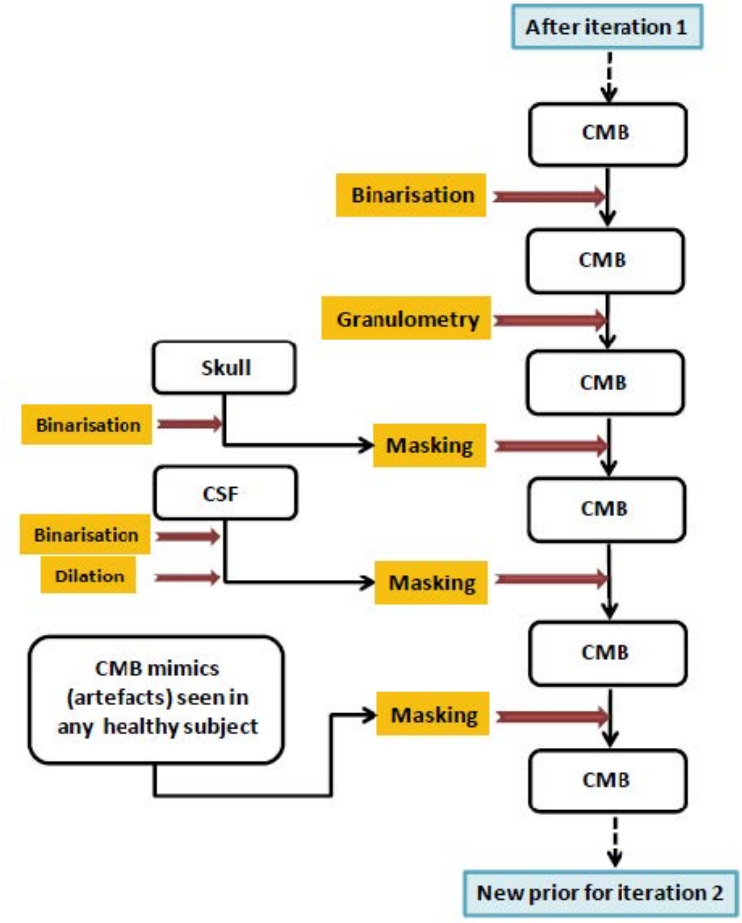

Figure 1.3.5: Illustration of the morphological operators used in MIDAS during false positives elimination step [Seghier et al., 2011].

The second iteration is more specific; as the priors have been refined by applying different masks. The results of MIDAS are then evaluated manually by a neuro-radiologist to remove false positives.

Monocentric data of 30 stroke patients presenting CMBs were used. The segmentation reference was obtained by a consensus between the manual segmentation of two experienced neuro-radiologists.

Results For agreement between MIDAS and the reference standard manual identification (MARS) in patients who had one or more CMBs in lobar regions was 0.43, increasing to 0.65 after manual correction of false positives. Agreement between segmented lesions and reference

is not communicated for this paper. The intraclass correlation coefficient[6] for agreement about CMBs count in lobar regions using MIDAS in comparison to MARS was 0.71, increasing to 0.87 when using the semi-automated method. The Kappa coefficient of identifying patients with two or more lobar CMBs increased to 0.74 using the semi-automated approach.

Among the 22 patients with lobar CMBs in the reference, 17 were classified as having CMBs. The five patients unidentified by MIDAS each had a unique CMB. MIDAS was more efficient for cortical and sub-cortical CMBs and exhibits significantly better performance for patients with more than one CMB. Missed CMBs were either eliminated by the «revised mask» (generated by control subjects), either very small and / or with too low contrast. MIDAS identified patients with CMBs at a sensitivity of 77% and a detection rate of 50% for total true CMBs. The number of false positives was not indicated [Seghier et al., 2011].

Supervised learning approach

Support vector machines (SVM) based method The work described in [Barnes et al., 2011] relies on a semi-automatic approach for the identification and the quantification of CMBs. The method consists of four steps described in Figure 1.3.6.

[6] The Intraclass Correlation Coefficient (ICC) is a measure of the reliability of measurements or ratings.

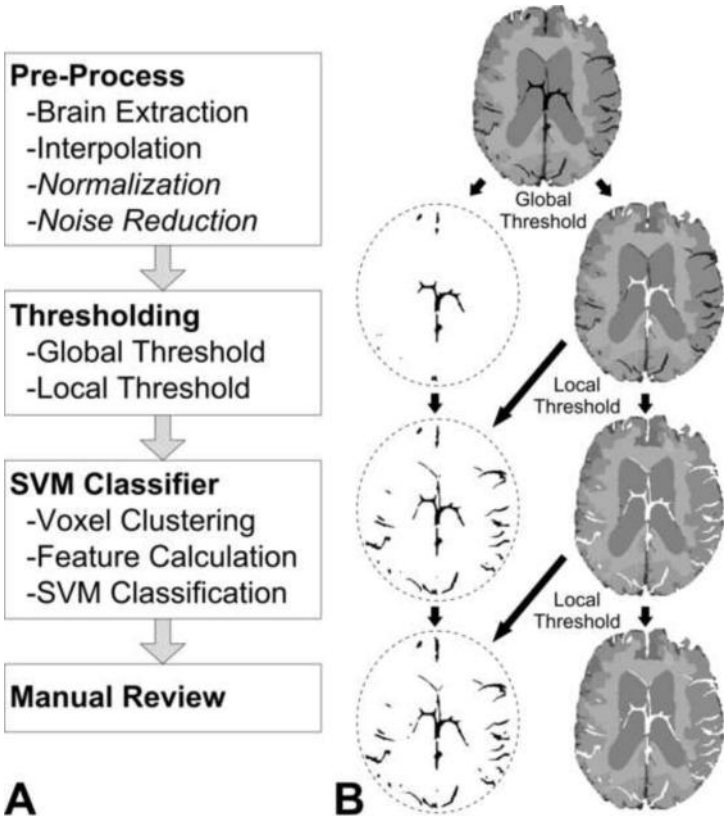

Figure 1.3.6: A) A flowchart of the processing steps, the two pre-processing steps in italics were not used in these datasets but might be useful for other types of data, and B) a detailed schematic of the thresholding step is provided, from [Barnes et al., 2011].

Step 1. Pre-processing: Extraction of the brain was accomplished using information of both magnitude and phase: hypointense areas in the magnitude image where noise was uniformly distributed in the phase image were considered as "empty signal". The images were then interpolated in the x and y directions (acquisition plane) using a zero filling in the k-space; apodization with the Hanning filter reduced distortions due to Gibbs effect.

Step 2. Thresholding: This step consists of two sub-steps. A global threshold was first applied to eliminate large dark areas that may distort the calculation of the local threshold. It was calculated as 2.5 times the standard deviation below the mean of the Gaussian intensity distribution modeling the entire magnitude image. Pixels with intensity below the overall threshold are labeled as «CMBs» and are not taken into account when calculating the local threshold in the next step. A white noise distribution was assumed in the parenchyma for a roughly Gaussian distribution with a small number of low-intensity outliers (such as CMBs)

that do not significantly alter the mean or standard deviation of the region; to find small hypointensities, a local threshold was applied window by window (window size of $21x21x3$ voxels (see Figure 1.3.7)). Its value was calculated from the average $\bar{x}$ and the standard deviation σ of voxel intensities of that window. Local threshold was equal to $\bar{x} - 2.5\sigma$ and its calculation was iterated several times, by removing the voxels with intensities lower than the threshold from the next calculation, then that voxels are labeled as CMBs.

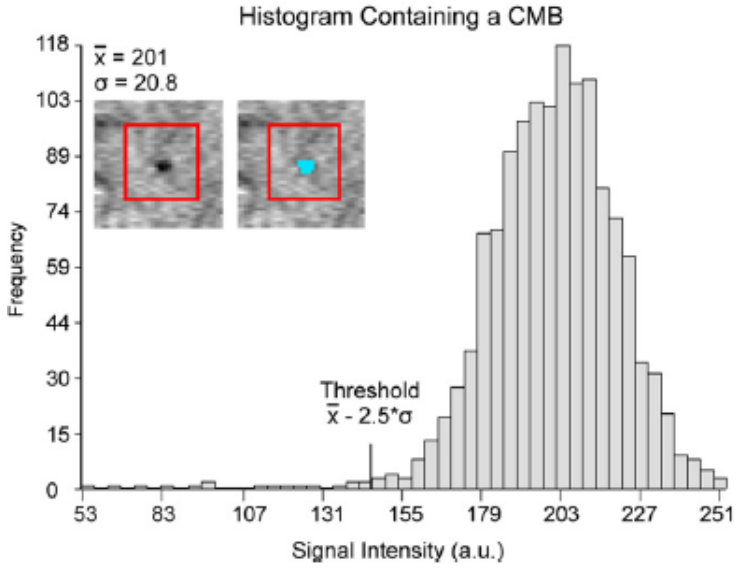

Figure 1.3.7: A histogram of a $21 \times 21 \times 3$ ROI that was used to calculate local thresholds is shown containing a typical CMB. The cutout shows the ROI and CMB and the thresholding results.

The choice of 2.5 when calculating threshold was to ensure to remove parenchyma. The choice of the window size was also important; CMB needs to be small with respect to the window size in order not to bias the mean and the standard deviation values of cerebral tissue calculation.

Step 3. False positives removal: To eliminate false positives resulting from the thresholding step, authors used a supervised learning tool, the support vector machines (SVM). SVM solves non-linear discrimination problems. It constructs a hyper plane or set of hyper planes in a high- or infinite-dimensional space, which can be used for classification. Intuitively, a good separation is achieved by the hyper plane that has the largest distance to the nearest training-data point of any class. The problem can therefore be formulated as a quadratic optimization problem to find the hyper plane that maximizes the margin, see Figure 1.3.8.

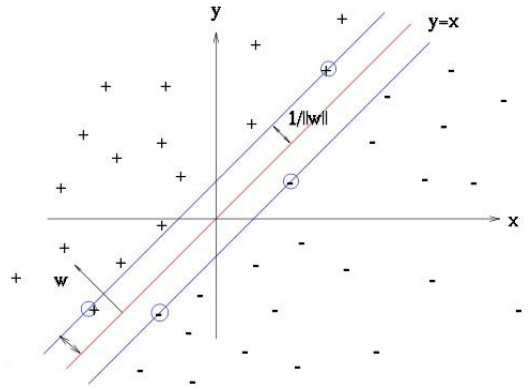

Figure 1.3.8: Maximum-margin hyper plane (in red) and margins for an SVM trained with samples from two classes(+/-). Samples on the margin are called the support vectors (in blue circles). **W** is the normal vector to the hyper plane.

SVM requires to define attributes or features that are specific for CMBs. A learning step was used to select the most discriminating features. A vector of fourteen features was thus used in the method, built from each ROI:

- 5 shape descriptors, to distinguish rounded structures such as CMBs with respect to tubular structures like blood vessels, were defined:
  - compactness: the ratio of surface area to the volume. Spherical shapes have higher compactness compared to elongated structures.
  - 3 eigenvalues of the co-variance matrix on the 3x3 matrix ROI: This matrix describes the mass distribution. A spherical shape would have three equal eigenvalues while a cylindrical shape would have one large eigenvalue and two smaller ones.
  - Relative anisotropy: this attribute combines the three eigenvalues of the co-variance matrix to characterize the anisotropy of the structure. A spherical shape will have a low anisotropy.
- 8 intensity descriptors were used: minimum, maximum, average and standard deviation on the image intensity (magnitude and phase).
- The kernel used was a radial basis function which showed good performance on similar data and has less numerical difficulties than polynomial kernels [Barnes et al., 2011]. The training set consists of 15000 false positives and 120 true positives obtained following the

thresholding step. The CMBs class was weighted by 100 to decrease the large gap between the number of two classes so it does not distort classification result.

The method was based on high resolution SWI acquisitions ($0.5x1x2\,mm^3$) with an echo time of 40 ms which is the recommended TE at 1.5T for SWI [Barnes et al., 2011]. The study was conducted on six subjects having in total 126 CMBs. The reference segmentation was performed independently by three experts; different results were then evaluated by a fourth more experienced neuro-radiologist.

Results This method allowed a high sensitivity (95%) but an increased number of false positives; Among the 126 true CMBs, 120 have been successfully identified but 15807 false positives have been also detected before the SVM step. SVM step was relevant to reduce the large number of false positives but a large number of FPs still remain (645). The supervised learning step also resulted in a higher number of false negatives (23). False positives thus requires a manual review to be eliminated while false negatives were not recovered because recovery would require to repeat the full evaluation.

Random Forest The most recent method was introduced by Fazlollahi et al [Fazlollahi et al., 2013] and it consisted of a machine learning approach for computer-aided detection of CMBs on SWI acquisitions. After contrast enhancement and biais field correction[7]. Its major steps were:

1. CMBs extent are identified in order to extract proper cubic regions-of- interest (ROI) containing the structure: The method has 2 steps:

   a) 3D sphere detection problem is divided into multi-scale 1D line detection along the three dimensions x, y and z;

   b) The center of shapes are identified by combining the normalized line responses obtained in the previous step.

2. 3D Radon [Fazlollahi et al., 2013] and Hessian-based shape descriptors are then extracted within the ROIs: the eigenvalues of the Hessian matrix of the extracted center points are employed to discriminate spherical object: (1) the mean and (2) the standard deviation profiles computed across the Radon angle-dimension, (3) the standard deviation along the

[7] The bias field correction refers to the correction of the inhomogeneity caused by the spatially-dependent response of the receiving coil.

Radon angle-dimension and (4) the global Radon mean. Using the eigenvalue decomposition of the Hessian matrix, other descriptors are defined; (5) the sphericity, (6) largest cross-section, (7) fractional anisotropy and (8) orientation.

3. 2D Radon features are extracted from the corresponding ROIs on mIP images. Same features as in step 2 that aims to address cross-sectional discontinuities due to anisotropic SWI acquisition.

4. Classification: Incorporating a cascade of random forests (RF) classifiers to iteratively reduce false positives: Increasing the RF probability threshold by adding FPs to the negative training examples of the following layer, the method can progressively build a balanced dataset without non informative candidates. A leave-one-out validation scheme was used to train the cascade which has a relatively balanced and informative training set in the final layer.

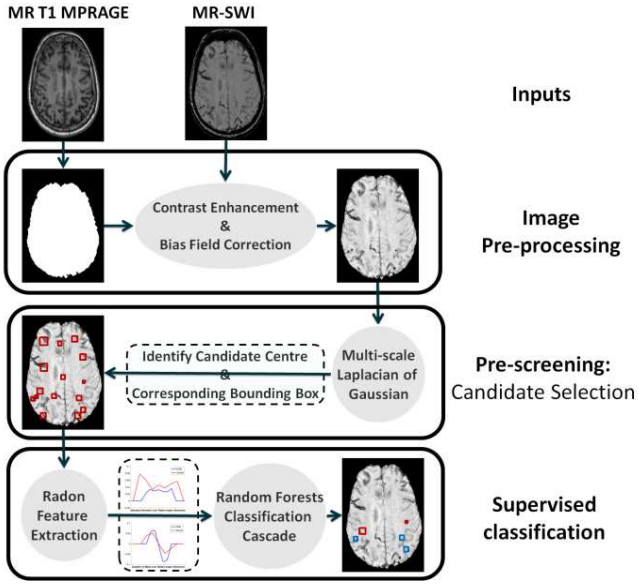

Figure 1.3.9: Outline for a 2-layer classification cascade with leave-one-out scheme in subject level used in [Fazlollahi et al., 2013].

For this study, a subset of 30 subjects with CMBs were included. For each subject, SWI images were acquired on a 3 T Siemens TRIO scanner with 0.9×0.9 mm in-plane resolution and 1.75 mm slice thickness, with TR = 27 ms and TE = 20ms. One expert had reviewed SWI images and in total 64 CMBs with prevalence of 2.1±2.2 per subject were found.

Result For definite lesions, an overall sensitivity of 94% and an average 7.6 false positives per subject were produced. When considering all lesions (definite and possible), the method had a sensitivity of 87% with an average false-positive rate of 20.2 per subject.

Shape based approach

Radial Symmetry Transform (RST) based method Kuifj et al [Kuijf et al., 2012] presented a method for CMBs detection based on shape and size analysis. It relies on the detection of spherical shapes with radius between 0.3 and 2.mm using a function of radial symmetry. This function has been proposed in [Loy and Zelinsky, 2003] and was initially used to detect points of interest on head landmarks (eyes, nose...). It uses image intensity gradient information to highlight spherical structures. In this study, it was computed on both echoes of a dual-echo T2*-weighted GRE 7.0 T MR sequence in 18 participants. 3D T1 acquisitions were also used in pre-processing with TR = 7 ms and TE = 3ms.

Method A symmetry score map was calculated on both echo images. This process will be further detailed in «the segmentation chapter» Resulting maps were then thresholded and only voxels with a score above -20 for TE1 and -100 for TE2 were considered as CMBs candidates. T2*-weighted images were normalized to $[0, 255]$, using values corresponding to the 5% and 95% of the histogram respectively as minimum and maximum. A parenchyma mask was applied to the score map. The mask was calculated using the «Unified segmentation» of SPM applied on the 3D T1 weighted image. The T1 probability map was registered to the T2* space of the first echo. These maps were then thresholded to 90%.

If within a 26-voxel neighborhood around a minimum in both sphericity maps exists, this location was considered a potential microbleed. Finally, if the normalized gray value on the second echo of a potential microbleed was not equal to zero, it was removed from the list, since a microbleed should cause a signal void on the T2*-weighted images. Manual review wad required to remove false positives.

The 18 participants had a total of 54 CMBs. The dual-echo T2* sequence allows two TEs to be acquired in a single sequence; TE1 = 2.5ms and TE2 = 15ms (see Figure 1.3.10). The images were reconstructed to $0.35 \times 0.35 \times 0.3mm^3$ voxels. All scans were independently and visually scored by two neuro-radiologists with more than 20 years of experience. Minimal in-

tensity projection post-processing of both echos were presented simultaneously. Rating of the microbleeds was performed according to MARS.

Both echos were considered during visual rating; without blooming effect, hypointensities were discarded and not considered as CMB.

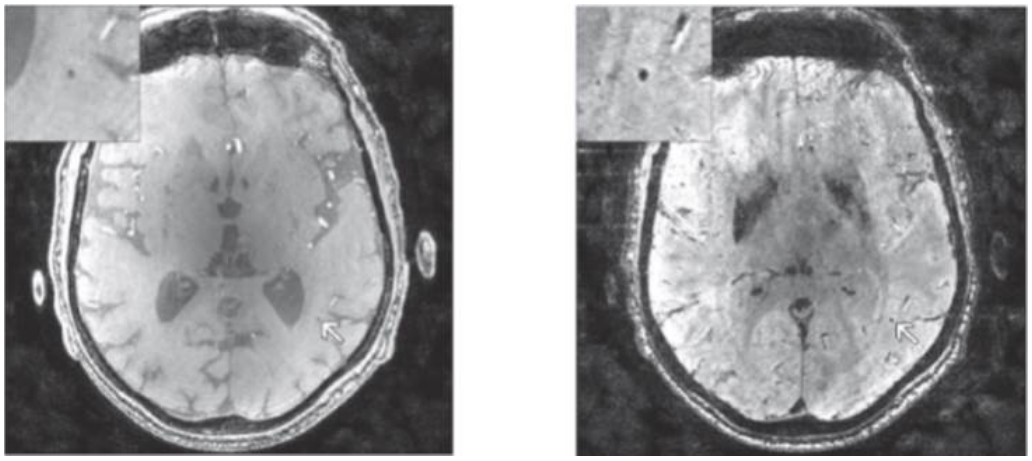

Figure 1.3.10: A typical slice of a 7T T2*-weighted MR scan, showing the first (left) and second echo (right). The white arrows annotate a CMB (enlarged in the upper-left corner) [Kuijf et al., 2012].

Results Visual identification of CMBs from the high resolution 7T images is a tedious process. According to [Gregoire, 2014], the evaluation of CMBs on a single patient takes up to 30 minutes. 353 lesions were identified with the radial symmetry function including 35 true positives, 309 false positives and 12 additional true positives (non identified by neuroradiologists and detected by the automatic method and subsequently recognized by neuroradiologists as true CMBs).

Region growing based method Also based on Radial symmetry transform, Bian et al [Bian et al., 2013] proposed a modified approach for CMBs detection on mIP SWI images within two main steps:

1) initial putative CMB detection using the 2D radial symmetry transform.

2) subsequent false positive reduction by characterizing geometric features of putative CMBs (size, localization, extent in z direction..) through region growing as illustrated in Figure 1.3.11.

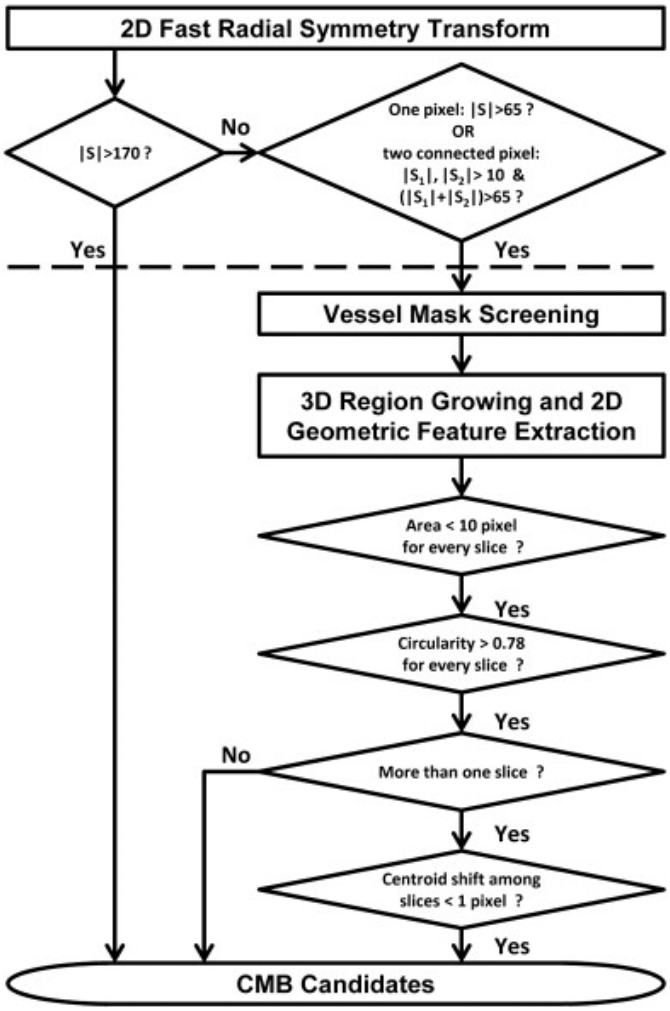

Figure 1.3.11: Schematic diagram for the proposed CMB detection algorithm and selected optimized parameters. (S refers to the intensity of RST map; the processing above the dashed line belongs to the step of initial putative CMB detection, while the below belongs to the step of false positive reduction.) [Bian et al., 2013]

Fifteen patients who had at least 10 potential CMBs on initial screening were included in this study. The patients were randomly divided into two sets: a training set that included 5 patients and a test set that included 10 patients. MR images were acquired on a 3T MR system; High resolution T2*-weighted imaging using a 3D flow-compensated spoiled GRE sequence was performed using TE/TR = 28/56 ms, flip angle 20°, 24 cm FOV, in-plane resolution of 0.5 × 0.5 mm, 2 mm slice thickness and a total slice number of 40. Standard SWI post-processing techniques were applied to the reconstructed k-space and then a minimum intensity projection images through 8 mm-thick slabs (4 slices), with a 6 mm-thick (3 slices) overlap between each

consecutive projection, were generated. CMBs identification used as a reference is the consensus of three independent ratings and were further divided into two groups: definite and possible CMBs.

The method was able to correctly identify 263 of the 304 total true CMBs, resulting in a sensitivity of 86.5%. CMBs of the reference were classified to definite and possible CMBs. Of these correctly identified CMBs, 16.7% (all definite) were directly identified after the radial symmetry transform function and did not undergo region growing and geometric features examination. Separating CMBs into definite and possible CMBs improved the sensitivity of definite CMBs to 95.4%, while the algorithm was less sensitive (77.5%) to possible CMBs [Bian et al., 2013].

Discussion/Comparison of state of the art methods for CMBs detection

Five methods were described in this section that require experts intervention to reach final results. Table 1.3.1 summarizes their results as published. Over all the five methods display a large number of false positives, with varying degrees of sensitivity as shown in Table 1.3.1.

Remaining false positives yielded additional time for manual reviewing which usually required three to ten minutes per patient.

Methods were based on shape, intensity and location criteria. They all appear were very efficient to detect large CMBs, perfectly round and completely surrounded by the parenchyma. However very small CMBs were often missed. When considering each method, some drawbacks may be pointed out. The mask used in MIDAS seems sub-optimal; in fact, the mask to remove artifacts built from control subjects seems unsuited as artifacts localization is more likely to be subject dependent. Furthermore, the result from the SVM method can be biased, since learning datasets are the same as test datasets and generalizability of the SVM approach for new datasets is not proven. Radial symmetry transform gave the lowest number of false positives and it seems more robust and more adapted to the definition of CMBs. However, when binarizing the resulting maps, the applied threshold was not successfully explained and justified, thus, issues regarding its generalization for other data may arise. Moreover, CMBs criteria dealing with multi-contrast (using combined information derived from T1, T2, T2* weighted images), as described in [Greenberg et al., 2009], were not investigated and no method has been validated on a large population with a large number of CMBs.

A fully automatic methods potentially present many advantages: it would automatically ana-

Approach	Validation data	Nb of subjects	True CMBs		sensitivity	False positives		
			total	mean		total	per patients	per CMB
Atlas based	$B_0 = 1.5T$, $GRET2*, TE = 40ms, TR = 300ms$, $FA = 20°, voxel_{size} = 0.93 \times 0.93 \times 6.5mm^3$	30	114	3.8	50%	Nc	Nc	Nc
SVM	$B_0 = 1.5T$, $GRESWI, TE = 40ms, TR = 57ms$, $FA = 20°, voxel_{size} = 0.5 \times 1.0 \times 2mm^3$	6	120	20	81.7%	645	107.5	5.4
RF	$B_0 = 3.0T$, $3D\,SWI$, $TE = 20ms, TR = 27ms$, $voxel_{size} = 0.93 \times 0.93 \times 1.75mm^3$	66	41	2.36	92.04%	690	16.84	6.7
RST	$B_0 = 7.0T, B_0 = 1.5T$, $GRET2*, TE = 2.5/15ms$, $TR = 20ms, voxel_{size} = 0.35 \times 0.35 \times 0.3mm^3$	18	66	3.7	71.2%	309	17.2	4.7
RST-region growing	$B_0 = 3.0T$, $3D\,GRET2*, TE = 28ms$, $TR = 56ms, voxel_{size} = 0.5 \times 0.5 \times 2mm^3$	10	304	30.4	86.5%	449	44.9	1.5

Table 1.3.1: Comparison of results among CMBs detection algorithms.

lyze large cohort facilitating pathology-MRI correlation studies. When it is robust and efficient, it may even decrease the risk of human rater error. An efficient fully automatic segmentation is more reproducible than manual segmentation which is variable and depends on rater's subjectivity.

1.4 Objectives

As seen above, CMB's identification on MRI only still raises issues regarding the exact definition of CMBs and how to discriminate them with high certainty from mimicking objects in the brain. To address the challenge of increasing its specificity, several characteristics of lesions and MR principles can be taken into account.

MR related characteristics: In-vivo CMBs identification can only be performed reliably on T2* GRE acquisitions. Resulting magnitude images are noisy and suffer from spread-wide susceptibility artifact. Susceptibility effect could be enhanced by increasing TE for example, thus potentially allowing to detect more CMBs. However, this would also increase susceptibility related artifacts more remarkably near bone / air interfaces. Phase images may allow decreasing TE-related variations. Furthermore, partial volume effect could significantly alter the signal distribution on T2* acquisitions and this effect increases with slice thickness. Acquisition of smaller slices should thus lead to better CMB identification.

Lesions characteristics: CMBs identification is made challenging by their definition in itself. In fact, CMBs are very small, which makes identification risky on 5mm thick 2D acquisitions. Furthermore, their size vary on a wide range with ill-defined limits, and they can also be multiple and thus overlap on magnitude images. They can easily be confused with blood vessels and other brain lesions such as cavernous malformation. 3D isotropic millimetric resolution would thus be far more suitable for CMBs identification and discrimination from 3D tubular shapes at blood vessels.

Overall, visual identification of CMBs remains problematic even for experienced neuroradiologists; even using validated visual scales proposed in the literature, the identification process is tedious, poorly reproducible and requires three to ten minutes per patient.

However, up to now automated methods for identifying CMBs suffer from very poor specificity and require large manual input. It thus appears crucial to design an automatic method for identifying CMBs with high specificity in order to enable its study in larger groups of subjects and thus better understand their clinical meaning.

The ideal segmentation method would be robust (reproducible), specific, reliable and fast. In fact, this method would perform efficiently on multi-center datasets, in research or clinical environment and allow discriminating even small CMBs from mimics.

In order both to increase specificity and parameter robustness, phase contrast appears as a good candidate to be embedded in a multi-contrast segmentation framework. Well-adapted shape and intensity characteristics are also crucial characteristics for discriminating CMBs.

In this PhD, I thus aimed at proposing and implementing a new tool to increase specificity of CMB identification while ensuring efficiency; First, ways of improving microbleed identification were explored through the use of MR phase images aimed at reliably rating CMBs. Second, the relevance of the developed new characterization method was investigated through a comparison study in a clinical setting. Third, the proof-of-concept of an automatic detection method of CMBs was designed.

* * *

Chapter 2

CMBs CHARACTERIZATION USING PHASE-CONTRAST

As shown in the previous chapter, designing a fully automatic method for CMB detection would be of great interest specially within the context of large imaging studies. Most of the proposed semi-automatic method were highly sensitive but the number of false positives remained too high to make it possible to proceed without observer intervention. Therefore, improving CMBs characterization may be the key to improve both visual and automatic detection. The aim of this chapter is to investigate how GRE Phase may help improving CMBs identification in a multi-center clinical dataset.

2.1 Requirements to process GRE phase images

Phase wraps

As seen above, phase signal can be written as:

$$\varphi(t) = \omega \cdot t + \varphi_0 \tag{2.1.1}$$

with φ_0 a phase constant. As shown in the equation above, phase should increase with time. However, the $\tan^{-1}$ function used to retrieve phase signal yields values within the $]-\pi, \pi]$ interval and phase overall variations are thus hidden. This definition of phase into the interval $]-\pi, \pi]$ results in phase wraps. As shown in Figure 1.2.11, wraps appear as sharp intensity transitions in the phase image. When realistic phase value reaches $\pi + \epsilon$, the encoded value will be $-\pi + \epsilon$.

This is illustrated in Figure 2.1.1. Borderlines, corresponding to closed phase wraps, are called "fringe-lines". In MR phase images, unclosed fringe-lines may occur and are called *open-ended fringe-lines* and they correspond to phase singularities. Singularities often occur in areas with low signal, and are then considered as noise. They can also occur in areas with high SNR; this may result from error during signal combination of different coils to reconstruct the image.

Phase unwrapping consists of finding the transition areas and adding $2k\pi$ (where k is an integer) from the measured phase when necessary to obtain a continuous signal:

$$\varphi_{unwrapped} = \varphi_{measured} + 2k\pi \tag{2.1.2}$$

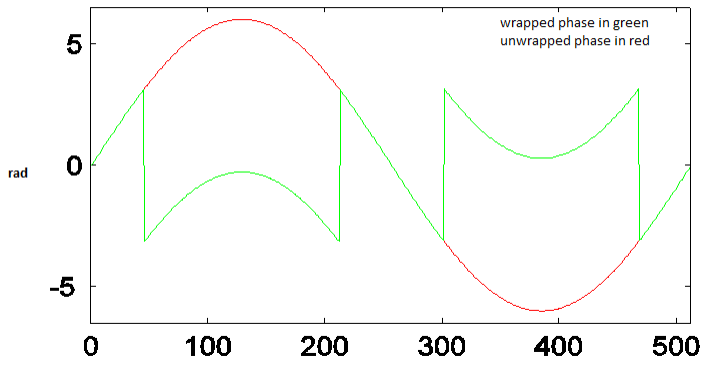

Figure 2.1.1: Illustration of 1D phase discontinuities.

An efficient phase unwrapping ensures that all appropriate multiples of 2π have been extracted. Several methods have been proposed to solve this problem: based on Fourier transform [Schofield and Zhu, 2003] or region growing approach [Witoszynskyj et al., 2009] such as the *PRELUDE* command available in the FSL tool `www.fmrib.ox.ac.uk/fsl`.

Background field removal

After solving the phase unwrapping issue, phase still do not reflect directly the magnetic field variations due to local process. in fact, the measured magnetic field also embeds contribution from the background field that is orders of magnitude stronger than that from intrinsic tissue susceptibility see Figure 2.1.2. Indeed, the background field is induced by sources such as the main field inhomogeneity that can result from imperfect shimming and the air-tissue interfaces. This background field, thus, needs to be removed to retrieve relevant information induced by

local sources. Traditional heuristic methods, including high-pass filtering, were used for the background field removal, although they also tamper with the local field and decrease quantitative accuracy [Schweser et al., 2013]. More recent background field removal methods based on physical principles, Projection onto Dipole Fields (PDF) [Tian Liu et al., 2011] and Sophisticated Harmonic Artifact Reduction on Phase data (SHARP) [Schweser et al., 2010b], demonstrated improved contrast and higher precision on the estimated local field. Both methods model the background field as a magnetic field generated by an unknown background susceptibility distribution, and differentiate it from the local field using either approximate orthogonality or harmonic property.

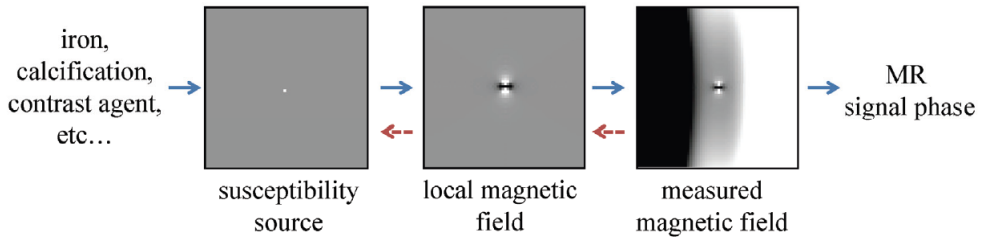

Figure 2.1.2: Relationship between susceptibility source and MR signal phase

However, state-of-the-art methods were not demonstrated to deal with background field removal on multi-center 2D multi-slice data.Due to the relationship between CMBs and internal field (yielded by local sources), we designed a novel method to extract internal field maps from datasets corresponding to routine clinical acquisitions that could be obtained in all centers and thus compatible with harmonized multi-center studies namely 2D simple echo GRE acquisition. This new fast processing technique includes unwrapping and harmonic filtering of phase images. It yields the internal field map, embedding the field generated by inner sources only (such as paramagnetic and diamagnetic structures within the brain). It was first validated on a numerical simulation, modeling paramagnetic inclusions (simulating cerebral microbleeds) and diamagnetic inclusions (simulating cerebral-micro-calcifications). Then, its applicability and robustness was demonstrated on real multi-center 2D datasets acquired in standardized clinical settings to discriminate between paramagnetic microbleeds and physiologic cerebral calcifications. A comparison with state-of-the-art methods showed that the new method performed better on these clinical datasets. In order to provide a proof of concept of its usefulness in

clinical setting, the method was satisfactorily evaluated for its ability to discriminate cerebral microbleeds from brain calcifications using MRI only.

This method and its evaluation was published as "2D harmonic filtering of MR phase images in multi-center clinical setting: toward a magnetic signature of cerebral microbleeds" in Neuroimage[1].

* * *

2.2 INTRODUCTION

Cerebral microbleeds (CMBs) were initially detected in histopathological studies of patients with small vessel disease [Cordonnier, 2011, Greenberg et al., 2009, Cordonnier et al., 2006]. They were described as small foci of chronic blood products in normal brain tissue [Greenberg et al., 2009, Poels et al., 2010, Van der Flier and Cordonnier, 2012]. Their size may vary from very small (~2 mm) to large lesions (~10 mm), while larger lesions are assumed to be more spread hemorrhages. CMBs characterization is of interest within the study of vascular dementia and Alzheimer's disease (AD) [Cordonnier et al., 2006]. However, CMBs identification using MRI remains challenging [Greenberg et al., 2009, Cordonnier, 2011].

CMBs are made of hemosiderin which is a strongly super-paramagnetic iron–storage complex [Cordonnier, 2011], whereas brain parenchyma is diamagnetic. Thus, their strong susceptibility difference with brain parenchyma makes CMBs foci appear as magnetic inclusions, causing local magnetic field inhomogeneity such as would be created by a unit dipole. At the voxel level, this field inhomogeneity leads to intra-voxel phase dispersion and strong T2*-contrast. Its detection is thus commonly based on Gradient Recalled Echo (GRE) T2*-weighted magnitude images, in which CMBs are visible as a loss of signal (hypo-intensity). However, their appearance on these sequences is sensitive to imaging parameters such as echo time (TE) and B_0 field strength;

[1] Kaaouana et al., 2015 : Kaaouana, Takoua, de Rochefort, Ludovic, Samaille, Thomas, Thiery, Nathalie, Dufouil, Carole, Delmaire, Christine, Dormont, Didier, & Chupin, Marie. 2015. 2D harmonic ltering of MR phase images in multicenter clinical setting: Toward a magnetic signature of cerebral microbleeds. NeuroImage, 104(Jan.), 287300.

clinical interpretation is thus made difficult by the resulting blooming artifacts. Furthermore, blood vessels and cerebral micro-calcifications (CMCs) also have strong T2* effects and can be misidentified as CMBs. While localization may help identification, discrimination commonly requires additional T1-weighted or T2-weighted images, or even a CT scan for CMCs [Yamada et al., 1996].

In order to overcome some limitations in CMBs identification, the phase image could also be considered. Usually discarded, the phase is available at no extra acquisition time. Being proportional to the local resonance frequency, phase directly reflects magnetic field inhomogeneity. Using phase information could allow increasing both specificity and sensitivity in CMBs detection. For example, calcifications are more diamagnetic than brain parenchyma and the induced magnetic field perturbation is opposed to that of paramagnetic CMBs; this difference should be accessible through phase information [Gronemeyer et al., 1992, Gupta et al., 2001, Schweser et al., 2010a, Yamada et al., 1996]. As for sensitivity, phase contrast strongly derives from susceptibility distribution and enhanced contrast could be expected on phase images between paramagnetic CMBs and parenchyma.

While phase is sensitive to local susceptibility variations, its analysis is not straightforward because of phase wrapping and strong background effects, as well as the complex magnetic field-to-source relationship. Indeed, reconstructed phase appears "wrapped", as it is only defined within $[-\pi, \pi]$; it thus requires the use of unwrapping techniques to recover a continuous phase information [Feng et al., 2013]. Additionally, local variations of interest may be orders of magnitude lower than those related to the background field inhomogeneity, which is dominated by the air-tissue interface, thus requiring efficient filtering algorithms to extract the contribution of the internal local field inhomogeneity pattern [de Rochefort et al., 2010a].

The first studies exploring the use of GRE phase images to discriminate between calcified and iron-laden tissues relied only on raw phase images [Yamada et al., 1996]. To further enhance detection sensitivity for small inclusions, background contributions have been suppressed using different high pass filters [Gronemeyer et al., 1992, Gupta et al., 2001, Wu et al., 2009, Yamada et al., 1996]. Combining phase and magnitude images, such as in susceptibility-weighted imaging (SWI), has already allowed enhancing detection sensitivity for paramagnetic structures such as veins or hemorrhages [Goos et al., 2011, Haacke and Reichenbach, 2011, Haacke et al., 2009, Nandigam et al., 2009, Reichenbach et al., 1997]. Recent advances in the understanding

of magnetic field distortions yielded more adapted phase processing techniques. Indeed, quantitative susceptibility mapping (QSM) is based on the reconstruction of magnetic susceptibility maps from an observed magnetic field perturbation [de Rochefort et al., 2010a, Liu et al., 2012, Schweser et al., 2011, 2012b]. These approaches have allowed to push further the limits of background field removal and solve the "field-to-source" inverse problem [Langkammer et al., 2012, Li et al., 2011, Schweser et al., 2012b, 2011], enabling to differentiate calcifications from hemorrhages [de Rochefort et al., 2010a, Deistung et al., 2006, Reichenbach and Haacke, 2001, Schweser et al., 2010a] and to provide improved CMBs detection sensitivity and contrast as compared to GRE magnitude images [Klohs et al., 2011, Liu et al., 2012]. These latter approaches generally rely on an inverse filter design based on complex post-processing methods; computing strategies currently remain under investigation. Furthermore, both SWI and QSM were designed for being applied to full 3D dataset and phase unwrapping and background field removal are necessary pre-processing steps for both methods.

To recover the internal field, several background field filtering techniques have been proposed. Assuming that background field variation mostly contains low frequency components within the region of interest while that of internal field contains high frequency components, low pass filtering using Gaussian [Hammond et al., 2008] or box kernel [Rauscher et al., 2003] or low order polynomial fitting [Deistung et al., 2008, Duyn et al., 2007] were first proposed. More recently, approaches relying on fitting external sources to internal field were proposed, using either highly-constrained model-based distributions [de Rochefort et al., 2010a, 2008, Neelavalli et al., 2009, Wharton et al., 2010], or fitting with more degrees of freedom such as in Projection onto Dipole Field (PDF) [Tian Liu et al., 2011]. The PDF approach has demonstrated efficient estimation of background field in an internal region of interest (ROI), but displayed remaining border artifacts [Tian Liu et al., 2011]. Finally, harmonic filtering techniques, such as Sophisticated Harmonic Artifact Reduction for Phase (SHARP) [Schweser et al., 2011], rely on the harmonic property of the background field inside a ROI, leading to a new class of Laplace based filters [Schweser et al., 2012a, 2011].

In the context of multi-center clinical studies, data from various manufacturers and models have to be analyzed jointly, even though phase image properties may differ between acquisition sites. Subtle differences in pulse sequence characteristics, coil sensitivity profiles, localization methods, phase reconstruction algorithms and other site/manufacturer specific characteristics

may combine to produce significant variation in final measurements. These differences must be taken into account to improve final pooled analyses. Furthermore, standard multi-slice 2D scan may result in inconsistent slice-to-slice field maps. These linear terms were observed experimentally on clinical datasets [Lee et al., 2013, Tam et al., 2009]. They may result from different 2D-based processes (shimming, motion, breathing-related artifact, normalization...), either at the acquisition or reconstruction levels, and lead to inconsistent phase maps between slices.

Here, we propose a filter design acting directly on the default reconstructed phase images to estimate internal field maps. This filter relies on a fast and robust 2D harmonic filtering (2DHF) approach that includes unwrapping, background field removal and additional linear artifact (due to slice-to-slice inconsistencies) correction at the same time. The method aims at being applicable on 2D datasets acquired in clinical settings in multi-center framework. Phase was long considered as unreliable information due to, first, its "non-local" nature and, second, its dependency to the two pre-processing steps described above [Schweser et al., 2010a]. The first issue is related to the non-local relationship between magnetic susceptibility distribution and phase. QSM may overcome this issue through the source reconstruction step but some approaches are computationally expensive and not straightforward to apply in multi-center settings. However, for clinical purpose, the main focus is on the type of lesion, namely diamagnetic or paramagnetic; "non-local field perturbation" may thus not be a limitation for clinical application based on internal field maps only. For the second issue, recent techniques such as SHARP were shown to allow robust pre-processing of phase images. 2DHF can be considered as a 2D version of SHARP, introduced as a 3D filtering technique in [Schweser et al., 2011].

The remainder of this article is organized as follows. The multi-center dataset used for validation is first presented, followed by a detailed description of the filtering method. Numerical simulation used for synthetic evaluation and two state-of-the-art filtering approaches used in a comparison study are then presented, as well as implementation issues. Evaluation and comparison results on numerical simulation and patient data are then shown, followed by a proof of concept illustration for the ability of 2DHF to define a magnetic signature for CMBs and CMCs on multi-center 2D datasets acquired in patients with memory impairment.

2.3 MATERIALS AND METHODS

Data on which the method was evaluated will be presented first together with acquisition details. The filtering method will then be described as well as the state-of-the-art filtering approaches and simulation used for validation.

2.3.1 Data acquisition

Data were acquired in the context of an ongoing national cohort in France named MEMENTO that aims at including, from research centers on memory, 2300 persons having cognitive symptoms ranging from isolated cognitive complaints to mild cognitive impairment. The protocol included MRI and PET acquisitions, supervised by the CATI, the French National Platform for Multi-center Neuroimaging Studies (Paris-Saclay, France). Data are provided through a national network composed of 24 centers with MRI systems from different manufacturers, models and field strengths. A sub-sample of the first 382 initial participants included in the cohort have been evaluated for CMBs. 77 subjects with CMBs were found, corresponding to 20% of this population, consistent with the prevalence previously reported in elderly subjects [Cordonnier and van der Flier, 2011]. CMBs identification was performed by a trained rater. The rater was trained to identify CMBs by an experienced neuro-radiologist on another dataset embedding 33 elderly subjects according to the following procedure. The rater identified CMBs according to the guidelines detailed in [Greenberg et al., 2009] and using the "MARS" scale [Gregoire et al., 2009]. Results were then checked for consistency by the experienced neuro-radiologist. For the dataset used in this study, uncertain lesions were double-checked by a trained neuro-radiologist; 23 patients were assessed as having possible CMBs (6%) while 54 were considered as having certain CMBs (14%). For the study presented here, only data of participants with certain CMBs were used. Data acquired on General Electric systems were excluded due to preprocessed phase images. Two participants were also excluded (from the Siemens 1.5T and 3T system datasets) due to open-ended fringe-lines as described in [Haacke and Reichenbach, 2011]. Retrospective analyses were performed on 28 subjects with CMBs from Siemens (four centers, one Trio and three Verio systems, 14 datasets) and Philips (four centers, all Achieva systems, 14 datasets) 3T systems. The protocol included a 3D T1-weighted sequence and a 2D T2*-weighted GRE sequence. Parameters for the 1 mm isotropic 3D T1-weighted scans were: TR/TE/TI/FA/BW=2300ms/2.98ms/900ms/9°/238Hz/voxel for Siemens systems

and TFE shot interval/TE/TI/FA/BW=2500ms/3.3ms/904ms/9°/241Hz/voxel for Philips systems, with 176 sagittal slices. Whole brain 2D T2*-weighted multi-slice GRE sequences were acquired with 2.5mm thick axial brain slices and 1 mm isotropic in-plane resolution with TR/TE/FA/BW=650ms/20ms/20°/199Hz/voxel. Reconstruction matrix was 240×240×65 for Philips systems and 256×256×70 for Siemens systems, with no zero padding. Standard 8 (Philips) or 12 (Siemens)-channel head coils were used. Acquisition time for 3D T1 and 2D T2* were respectively 9:14 min and 4:06 min for Siemens and 9:24 and 4:05 min for Philips. In the Memento cohort, image acquisition has been standardized as much as possible to minimize inter site variability. However, differences between Philips and Siemens sequence parameters still remain, originating either from hardware or software issues, as a compromise was sought between standardization of parameters and acquisition times. First, parallel imaging approaches (GRAPPA vs SENSE) and different coil number, sensitivity profiles and associated correction algorithm (CLEAR for Philips and Prescan Normalize for Siemens) resulted in both differences in contrast and additional constraints for setting the sequence parameters. The field of view was slightly smaller on Philips acquisitions (240x240x162.5 vs 256x256x175mm) with reduced number of slices (65 vs 70) due to longer acquisition time that had to be reduced. The effective TR per slice was also shorter (650ms vs 872ms), which may modify T1 contrast and slice saturation cross-talk. The slice scan order and the number of packages was different: interleaved with 2 packages for Siemens, and set to default with 3 packages for Philips; the Philips default setting maximizes the time between the measurement of each pair of adjacent slices. Additionally, within phase reconstruction, a standard "1D linear phase correction" was applied in the readout direction for Philips datasets, which is based on phase correction factors obtained in a preparation phase and that may cause the "Zebra"-like stripes observed on raw phase images. Other parameters and scaling factors may remain hidden for both Siemens and Philips systems, being integrated within manufacturers' software. Finally, when visualizing images from the two manufacturers, some differences between Siemens and Philips datasets appear obvious, as shown in Figure 2.3.1: background in both raw magnitude and phase and wraps show different aspects together with typical slice-to-slice inconsistency.

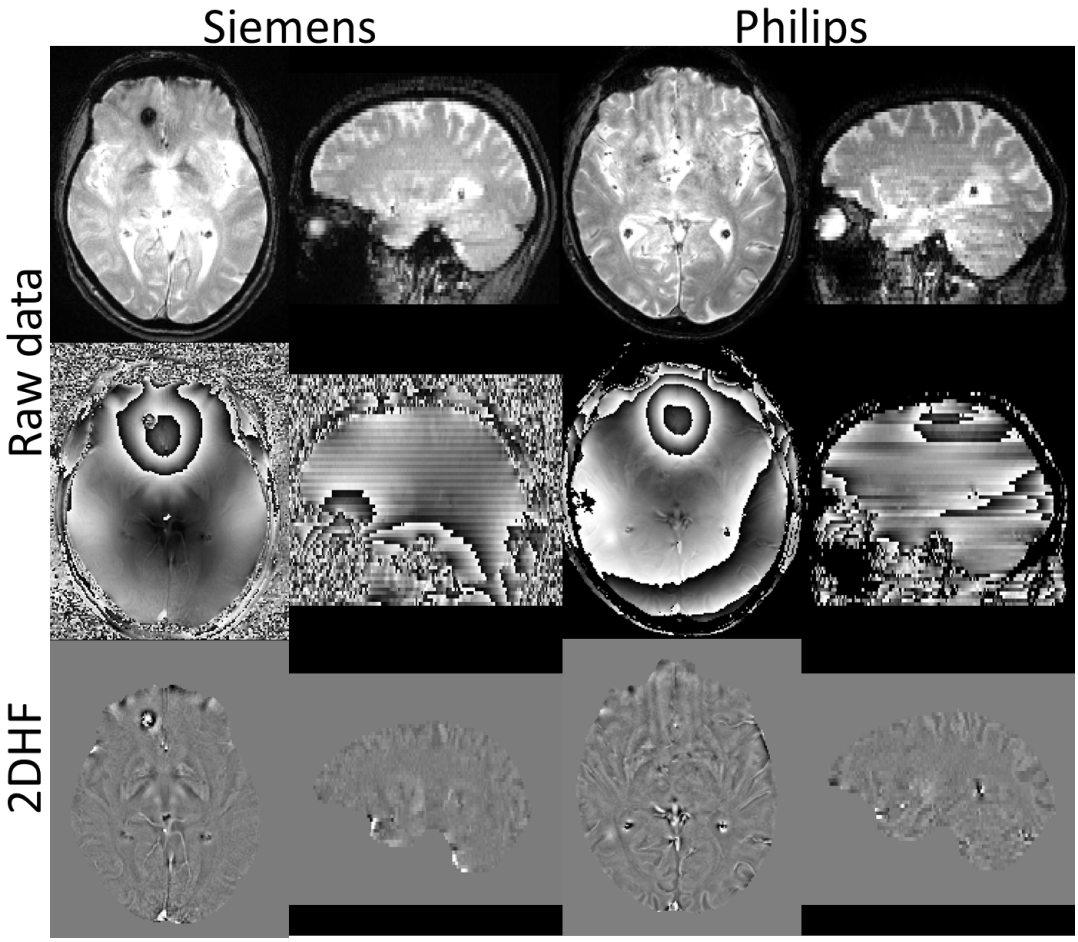

Figure 2.3.1: Illustration of Siemens (left) and Philips (right) raw data (magnitude and phase) and accordingly calculated internal field maps (3rd raw).

2.3.2 Internal field computation with 2D harmonic filtering (2DHF)

Extraction of relevant internal field information from phase images requires two preliminary steps: phase unwrapping and background field removal. In most proposed methods, this problem is solved in two separated steps; which may be iterative [Bilgic et al., 2012, de Rochefort et al., 2010a, 2008, Liu et al., 2012, de Rochefort et al., 2010b]. A particularly relevant phase unwrapping technique based on solving Poisson equation was proposed by Song et al. [Song et al., 1995] and extended in 3D to the QSM context [de Rochefort et al., 2010b]. Harmonic filtering, such as SHARP [Schweser et al., 2011], have shown to be extremely efficient in removing the harmonic component due to background sources. However, these methods were validated on 3D phase maps, and may not deal with potential slice-to-slice phase inconsistency that may

occur in 2D datasets.

The linear approximation of Maxwell equations is considered relevant in the MRI framework [de Rochefort et al., 2008]; the field inside the brain, B, can thus be decomposed as the sum of variations due to internal sources, B_{in}, and variations induced by external sources, B_{out}. From Maxwell equations, the external field is harmonic inside the brain [Li and Leigh, 2001, Schweser et al., 2011], resulting in $\triangle B_{out} = 0$, thus leading to $\triangle B = \triangle B_{in}$ ($\triangle$ denotes the Laplacian). Consequently, external effects can be filtered out through a second order derivative, followed by a second order integration using adequate boundary conditions. Note that any additional linear term is filtered out by the 2^{nd} order derivative.

Unwrapping using Poisson equation and background field removal using harmonic filtering are the basis of the 2D harmonic filter (2DHF) that will be described below and that were applied on the phase image of the 2D multi-slice T2* GRE sequence. Its principle is also given in Figure 2.3.2.

1. Slice-by-slice phase unwrapping was performed by calculating the 2D phase gradient image as the point-by-point difference between neighbors. This 'unwrapping' method does not actually compute the unwrapped phase (φ) but rather yields an unwrapped phase gradient maps ($\nabla\varphi$) prior to the second order derivation.Wraps were then detected using the modulo function which shifts phase values within the range$[-\pi, \pi[$ [Song et al., 1995]. This method assumes that phase gradients are smaller than π and was proven to be efficient for large SNR [Conturo and Smith, 1990].

2. The divergence of the estimated unwrapped phase gradient map was then calculated to get $\triangle B$: using the point-by-point difference between neighbors similarly as for the gradient. In this second step, the Laplacian was then nulled-out outside a brain mask, defining at the same time the 'internal' region-of-interest (ROI).

   The ROI mask was automatically generated with SPM8 software package (`http://www.fil.ion.ucl.ac.uk/spm`). The "New Segment" module was applied on 3D T1 images. Resulting probabilistic maps of gray matter, white matter and cerebro-spinal fluid were registered to the 2D T2* GRE image space [Ashburner and Friston, 2005]; rigid body transformation was computed using the "Coreg" module. These maps were then thresholded above 0.5 to obtain a cerebral mask [Samaille et al., 2012]. This mask was eroded (3-voxels radius 2D element) to ensure that no interface with large susceptibility effect

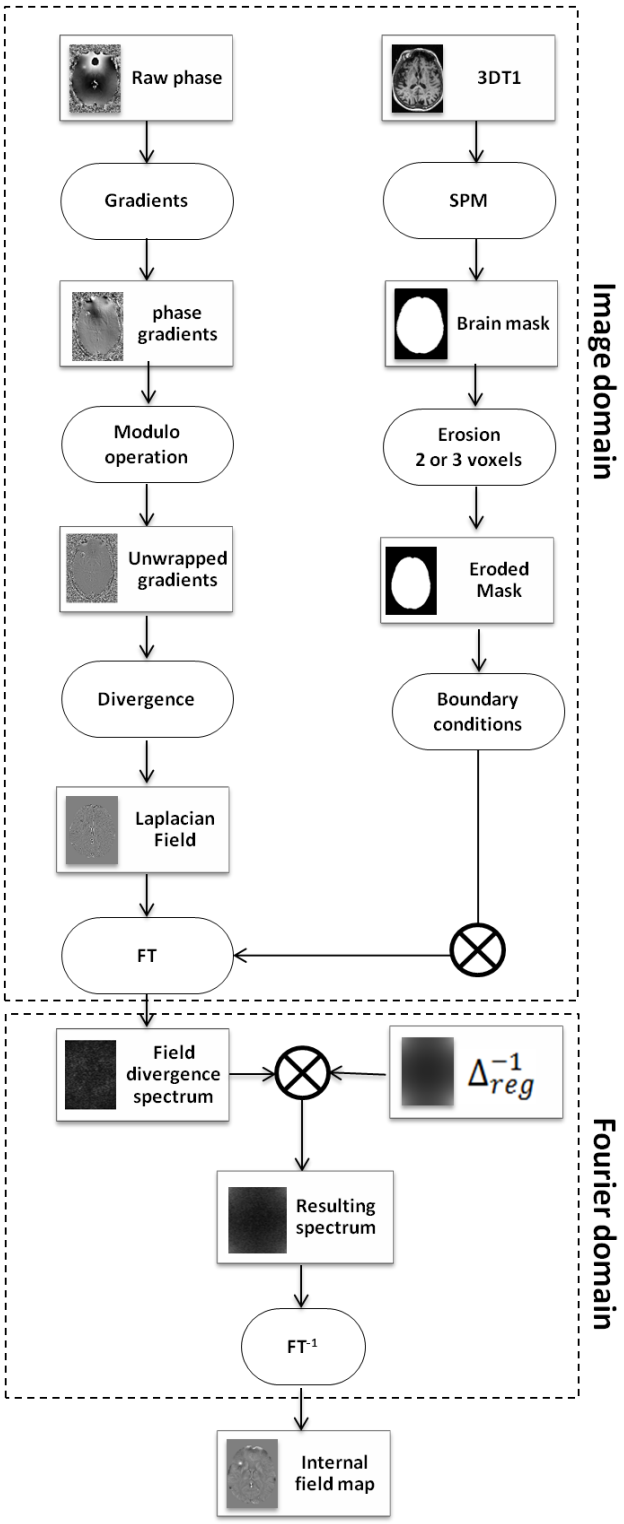

Figure 2.3.2: Schematic illustration of the 2D harmonic filtering framework working both in image and Fourier domains. As can be seen, to estimate the Laplacian, spatial derivative are calculated in two steps allowing the inclusion of unwrapping using modulo operations. A mask, generated with SPM is then used to set to 0 the Laplacian outside the brain. Integration is finally performed in Fourier domain with the adequately regularized inverse filter leading to an internal field map estimate.

was left in the mask and thus impose proper boundary conditions. This allows limiting potential artifacts near interfaces, where second order derivative may also suffer from noise propagation [Schweser et al., 2012a].

3. The internal field map in itself relies on an integration of $\triangle B$ to recover B_{in}. For more efficiency, this step was done in Fourier domain by multiplying the 2D-Fourier-transform of the calculated $\triangle B$ with the Fourier transform of a regularized (Tikhonov regularization) inverse of the 2D Laplacian filter. Let $k^2_{x,y}$ denote the discrete Laplacian filter in the Fourier domain. In order to ensure numerical stability for spatial frequencies close to 0, a regularization parameter α can be introduced within the inverse of the Laplacian, which leads to the following Tikhonov regularized least-squares filter:

$$\triangle^{-1}_{reg} = \left(k^2_{x,y}\right) / \left[\left(k^2_{x,y}\right)^2 + \alpha^4\right] \tag{2.3.1}$$

Apart from the definition of the internal ROI and the inclusion of phase unwrapping, the procedure is equivalent to the following high-pass filter in which α defines a cutoff frequency, as it is the spatial frequency corresponding to the half-width at half maximum:

$$\triangle^{-1}_{reg}\triangle = \left(k^2_{x,y}\right)^2 / \left[\left(k^2_{x,y}\right)^2 + \alpha^4\right] \tag{2.3.2}$$

Note that the 2D harmonic filter can be considered as a 2D version of a small SHARP kernel [Schweser et al., 2011] and should thus guarantee the removal of in plane harmonic components generated by background dipoles within the ROI.

2.3.3 Comparison with other filtering methods

Background field removal techniques may be split into two classes as a function of their underlying assumptions. One method from each class was implemented here for comparison with the 2DHF filtering approach. The first class is based on the assumption that variations of the background field are spatially slower than those of the internal field[Deistung et al., 2008, Haacke and Reichenbach, 2011, Hammond et al., 2008, Rauscher et al., 2003]. The high pass filtering (HPF) method is commonly used [McAuley et al., 2011, 2010, Schweser et al., 2013] and was implemented here for comparison. To obtain high-pass-filtered phase images, complex-valued images were first generated from the magnitude and phase images. They were then low pass filtered slice-by-slice by multiplying with a two dimensional Gaussian filter in Fourier domain. The

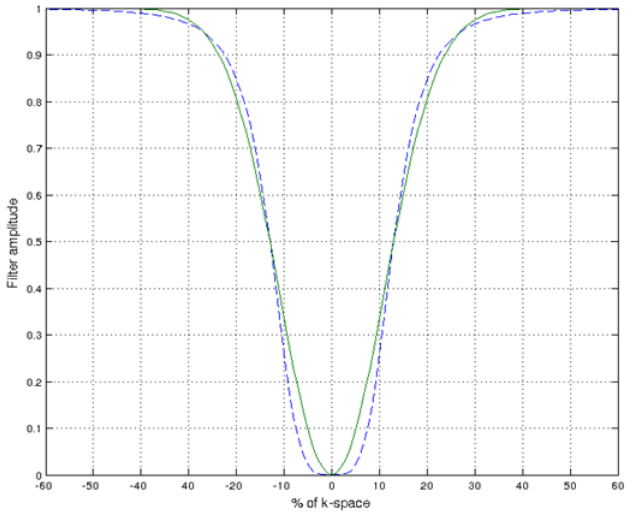

Figure 2.3.3: 2DHF (in blue) and HPF (in green) filters in Fourier domain. A 1D profile through Fourier domain center is plotted, with the same cut-off frequency for the two filters (a = 0.2 for illustration, equivalent to 20% of the central frequencies attenuated).

standard deviation σ of the Gaussian filter was chosen so that the half-width-at-half-maximum of the HPF was the same as the one of the 2DHF filter, namely $\sigma = \alpha/\sqrt{2\ln(2)}$ (see Figure 2.3.3). High-pass filtered phase images were then computed as the phase of the ratio between complex-valued and low-pass-filtered images.

The second class of filtering approaches assume that the field created by the background sources and the field created by the internal sources are orthogonal within the ROI in a suitable base. Among these methods, PDF was used here [de Rochefort et al., 2010a, Tian Liu et al., 2011]. It is based on the observation that the inner product between the field of a dipole located outside the ROI and the field of a dipole located inside that ROI is almost zero [Tian Liu et al., 2011]. Therefore, projecting the measured field within the ROI onto the subspace which is orthogonal to the field of either internal or background sources allows eliminating the contribution of internal sources, resulting in a background field map estimate. A subtraction of this background field map to the total field yields the internal field map. Technically, a susceptibility distribution outside a ROI that optimally matches the field inside the ROI is sought by minimizing an energy function. Prior to applying PDF, phase maps were unwrapped using the unwrapping method described in [de Rochefort et al., 2010a]. The SHARP method [Schweser et al., 2011] also belongs to this class. It is based on harmonic property of the background field inside the predefined ROI which can be eliminated from phase data by the

$Value(ppm)$	1	0.5	0.5	0.5	0.25	0.125	0.0625	0.03125
$Size(Voxels)$	1	4	2	1	1	1	1	1

Table 2.3.1: Susceptibility inclusions (from bottom to top), added to the background model to simulate the paramagnetic CMBs. Susceptibility (value) and spatial extension (size) are given. CMCs had then same absolute values, but with opposite sign (diamagnetic).

spherical mean value operation.

2.3.4 Numerical simulation

A numerical model was designed to evaluate the different filtering approaches. To model a background field created by the head, an ellipsoid with a susceptibility of -9 ppm (part per million) was considered (main axis dimensions were 75 (in head-foot direction), 100 (in right-left direction) and 125 mm (in antero-posterior direction). Two smaller ellipsoids were removed to simulate the strong effects that can be observed close to ear canals (dimension 5x10x16mm). Multiple dipole inclusions were embedded in the central slice: paramagnetic dots were placed in the left hemisphere while diamagnetic dots were placed in the right hemisphere. Inclusions were as indicated in Table 2.3.1 to mimic various susceptibility values and spatial extensions in a range consistent with previously reported susceptibility values for hemorrhage (~1 ppm) [de Rochefort et al., 2010a]. In fact, susceptibility values lower than 1ppm are supposed to mimic partial volume effects with inclusion smaller than the voxel size. Similarly, a 2-voxel inclusion with 0.5 ppm models some partial voluming for the same magnetic moment as a 1-voxel inclusion with 1ppm; a 4-voxel inclusion with 0.5 ppm models some partial voluming with a magnetic moment twice as large as that of a 1-voxel inclusion with 1 ppm, simulating a different intra-voxel configuration. Susceptibility variation was added to tissue effects. In order to mimic realistic experimental parameters, spatial resolution was chosen as 1mmx1mmx2.4mm. To cover the whole brain, a reconstruction matrix of 210x210x256 was used. The field (in ppm) created by this susceptibility distribution was computed using the forward approach [Marques and Bowtell, 2005, Salomir et al., 2003] and will be noted F.

Simulated MR signals were then generated by forming the complex value maps by converting magnetic field to phase ($\varphi = \gamma \times B_0 \times TE \times F$) with γ the gyromagnetic ratio of hydrogen nucleus, $B_0 = 3T$ and $TE = 20ms$. In order to mimic the 2D GRE T2*-weighted scans, random noise was generated from a normal distribution and added on both real and imaginary components,

assuming SNR=30 which corresponds to experimental values. A random constant within slice gradient was added to each slice to mimic the observed slice-to-slice inconsistency (more details are given in Appendix 1).

2.3.5 Regularization parameter

The 2DHF regularization parameter α was empirically set as follows. Four datasets were randomly chosen for tuning, two from Siemens and two from Philips systems. The influence of α on the generated internal field maps was systematically visually evaluated over a large range of values with a fixed step (from 0.01 to 0.30, with 0.05 steps). It was finally set to $\alpha = 0,15$, according to the criteria described below. The setting was then visually confirmed in all 28 subjects. Visual inspection of internal field maps in parameter tuning and comparison analyses was based on the criteria given for brain phase contrast in [Duyn et al., 2007, Haacke and Reichenbach, 2011]:

- Internal field map should provide anatomic information of local details, enabling delineation of many different brain structures and sub-structures;
- Global phase variations should be removed in order to reveal the local phase differences generated by the tissue micro-structure;
- Grey/white matter interface should be clearly visible;
- Numerous anatomical details should be visible in specific regions, such as central brain region, columna fornix, cross-section of the mamillo-thalamic tract, globus pallidus, putamen, and head of caudate nucleus.

As mentioned above, parameter setting for 2DHF can be compared with the equivalent setting for the standard deviation defined for HPF. For high pass filtering, width usually used is (32x32) which is equivalent to a filtering of ~13% of central frequencies. Figure 2.3.3 illustrates the corresponding filters with the same width at half maximum for comparison: 2DHF appears to have a sharper transition region than HPF.

2.4 RESULTS

Simulation results for the 2DHF method will first be shown, together with a comparison with the two state-of-the-art methods HPF and PDF. Results and comparison between methods on clinical data will then be detailed, followed by a proof-of-concept for the discrimination between CMBs and CMCs based on internal field maps obtained with 2DHF.

2.4.1 Numerical Efficiency

All the processes, including brain mask generation, were programmed with MATLAB (version 2011b) and run on a Quad-Core (Intel® Xeon(R) CPU W3520 @ 2.67GHz × 4) with 16 GB RAM. As 2DHF processing method is not iterative, computation time depends only on matrix size. The total computation time of the background field removal process was measured using the MATLAB built-in timer for 28 patients and mean computation time to process a full dataset was 2.2 s. HPF, which is a direct filtering method, had a similar computation time. On the contrary, PDF was approximately 100 times slower (for 512 iterations) than 2DHF in our implementation, because of its intrinsic 3D iterative process.

2.4.2 Simulation results

Results of the simulation are presented in Figure 2.4.1 for the full dataset. As shown in Figure 2.4.1 (a, b, c, d), the simulation correctly reproduces the order of magnitude of the phase shift observed within the brain. Strong background effects resulting from the interface of the large ellipsoid with the background and the air within the smaller ellipsoids were retrieved, leading to denser wraps in region closer to boundaries simulating air-tissue interfaces. The internal field (in Figure 2.4.1, e, f) displays small-scale dipolar patterns around the small simulated lesions. Note that the small lesions can be distinguished in the simulated wrapped phase map, whereas they do not clearly appear on the total field, because of scale differences between their susceptibility effect and that of the object/background interface.

To evaluate the ability to remove large background effects, an overall view of the internal field map as well as the field originating from the simulated background is presented for simulation (Figure 2.4.1, e-h), HPF (Figure 2.4.1, i-l), PDF (Figure 2.4.1, m-p) and 2DHF (2.4.1, q-t). While preserving signal from the simulated lesions at the chosen cutoff frequency (here, 0.15),

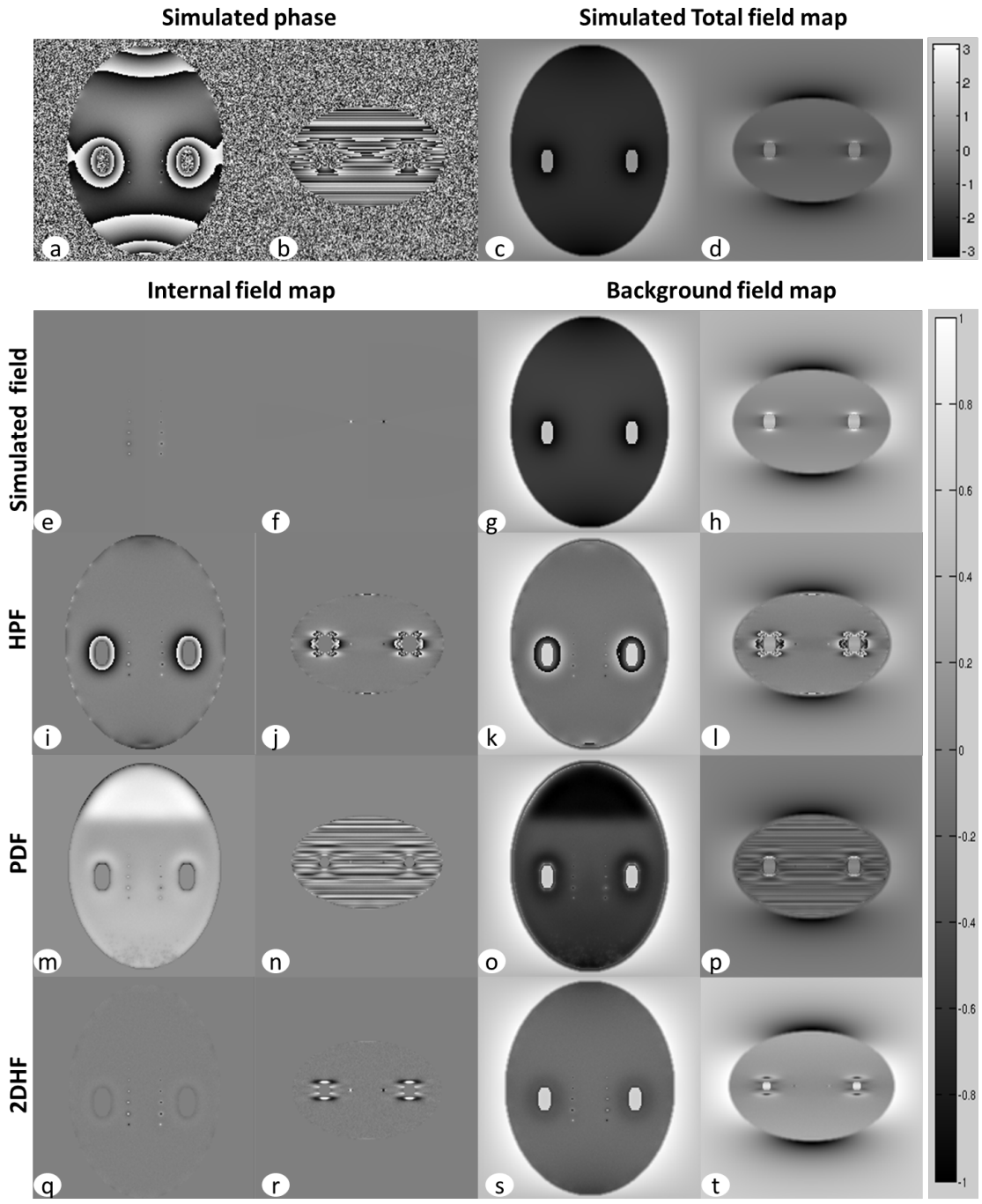

Figure 2.4.1: Background removal efficiency using numerical simulations. (a, b) axial and sagittal wrapped phase map from a central slice of the numerical model showing strong background effects from the ellipsoid shape and large 'air' inclusions. (c, d) axial and sagittal slices of the simulated field including background and internal effects. (e,f) simulated internal field map only, and (g,h) simulated background field map only. (i,j) internal field map calculated with HPF, and (k,l) its residual. (m,n) internal field map calculated with PDF, and (o,p) its residual. (q,r) internal field map calculated with 2DHF, and (k,l) its residual. Sagittal slices are shown with a voxel ratio of 2.5 (see text).

HPF introduced substantial artifacts in the vicinity of boundaries and did not fully suppress phase wraps. Note that more restrictive filter width was evaluated for HPF and appeared to remove large scale inhomogeneities and phase wraps more efficiently but also yielded a reduced phase contrast for the simulated lesions. PDF removed phase wraps and background effect while preserving contrast around simulated lesions. Nevertheless, large in-plane signal non-uniformity appeared in the antero-posterior direction. These large artifacts derive from not taking into account inter-slice inconsistency. 2DHF was much more efficient to remove both wraps and background effect while preserving both contrast and uniformity, but a limited border artifact was created.

Regarding the slice-to-slice inconsistent linear artifact, HPF efficiently filtered it out within the center region of the simulation. On the contrary, PDF did not remove these linear effects. Finally, 2DHF intrinsically filtered it away because the core of the method is based on second order derivatives.

To evaluate the efficiency of the three methods around the simulated lesions, a zoom is presented in Figure 2.4.2. While PDF results displayed remaining effects from slice-to-slice inconsistency (Figure2.4.2, c, g), all 3 methods efficiently extracted similar internal effects around simulated lesions (Figure 2.4.2, a, b, c, d). The similarity of the small scale results for 2DHF and HPF behavior directly stems from the fact that results for both methods are shown here for a similar bandwidth Figure 2.3.3.

Small calcifications may remain invisible on the CT scan [Kristanto et al., 2012]. Figure 2.4.2 shows that even a single-voxel-lesion with a susceptibility variation of +/–0.125ppm appears more paramagnetic than its surroundings in the internal field map with realistic simulated acquisition parameters and SNR; this would correspond to a hemorrhage / calcification almost ten times smaller than the simulated voxel size. Consequently, detection sensitivity of 2DHF can be considered as being of the same order of magnitude as the one reported for CT [Kristanto et al., 2012].

2.4.3 Results and comparison on clinical data

Figure 2.4.3 illustrates the resulting internal field maps obtained from filtered 2DHF phase images for two Siemens and two Philips datasets. Four illustrative examples of phase contrast observed in human brain with CMBs are presented. Compared to raw phase data, 2DHF

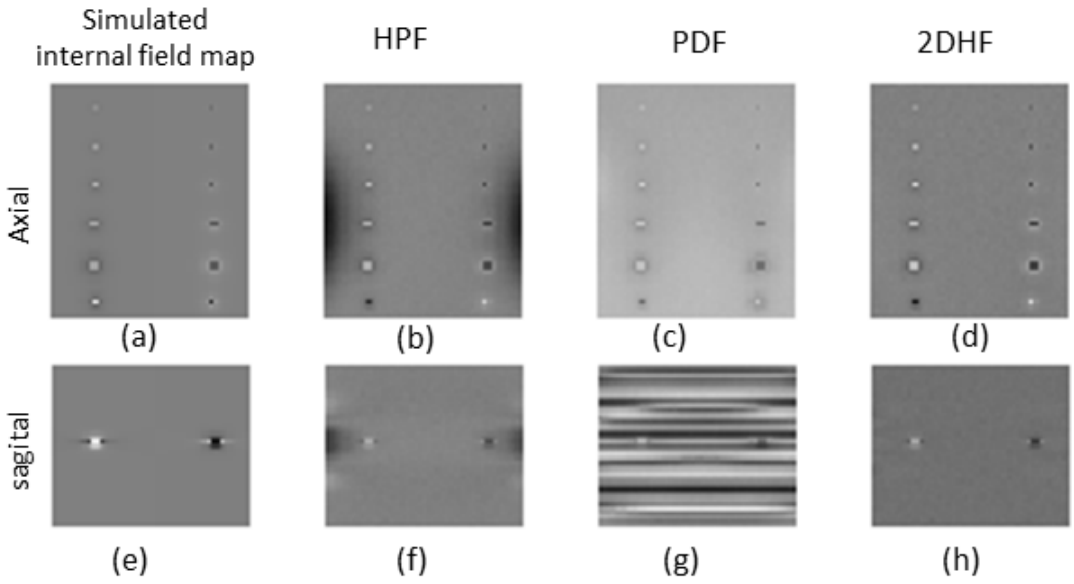

Figure 2.4.2: Internal field extraction efficiency using numerical simulations. Zoom on central slice of the ellipsoid showing the different dipole-like inclusions (see Table 1). Axial and sagittal view of the simulated internal field map (a,e), and internal field map calculated with: HPF (b,f), PDF (c,g) and 2DHF (d,h).

efficiently eliminated wraps and large-scale background effects and enhanced the anatomical structures of interest within the brain where paramagnetic substances such as those in CMBs appeared with a positive phase. The masking step proved efficient to remove most of the 2DHF-induced artifacts at the border, and cortical gray / white matter contrast was visible. Nevertheless, some artifacts remained.

A qualitative comparison of 2DHF, PDF and HPF for clinical datasets is presented in Figure 2.4.4. HPF results were shown here for a cutoff parameter of 32 which is usually chosen in literature [Schweser et al., 2013], in order to allow efficient removal of wraps and background effects [Schweser et al., 2013], resulting in a bandwidth more than twice larger than 2DHF width. As could be expected, the resulting internal phase contrast was much lower for HPF, while 2DHF and PDF displayed similar local content on axial slices with a good contrast for deep gray matter nuclei, blood vessels and CMBs. As in the simulation results, slice-to-slice inconsistency was efficiently corrected by HPF and 2DHF, but an effect remained for PDF which makes sagittal characterization difficult. The difference between 2DHF and PDF was dominated by inter slice inconsistency remaining with PDF, whereas the difference between 2DHF and HPF shows that

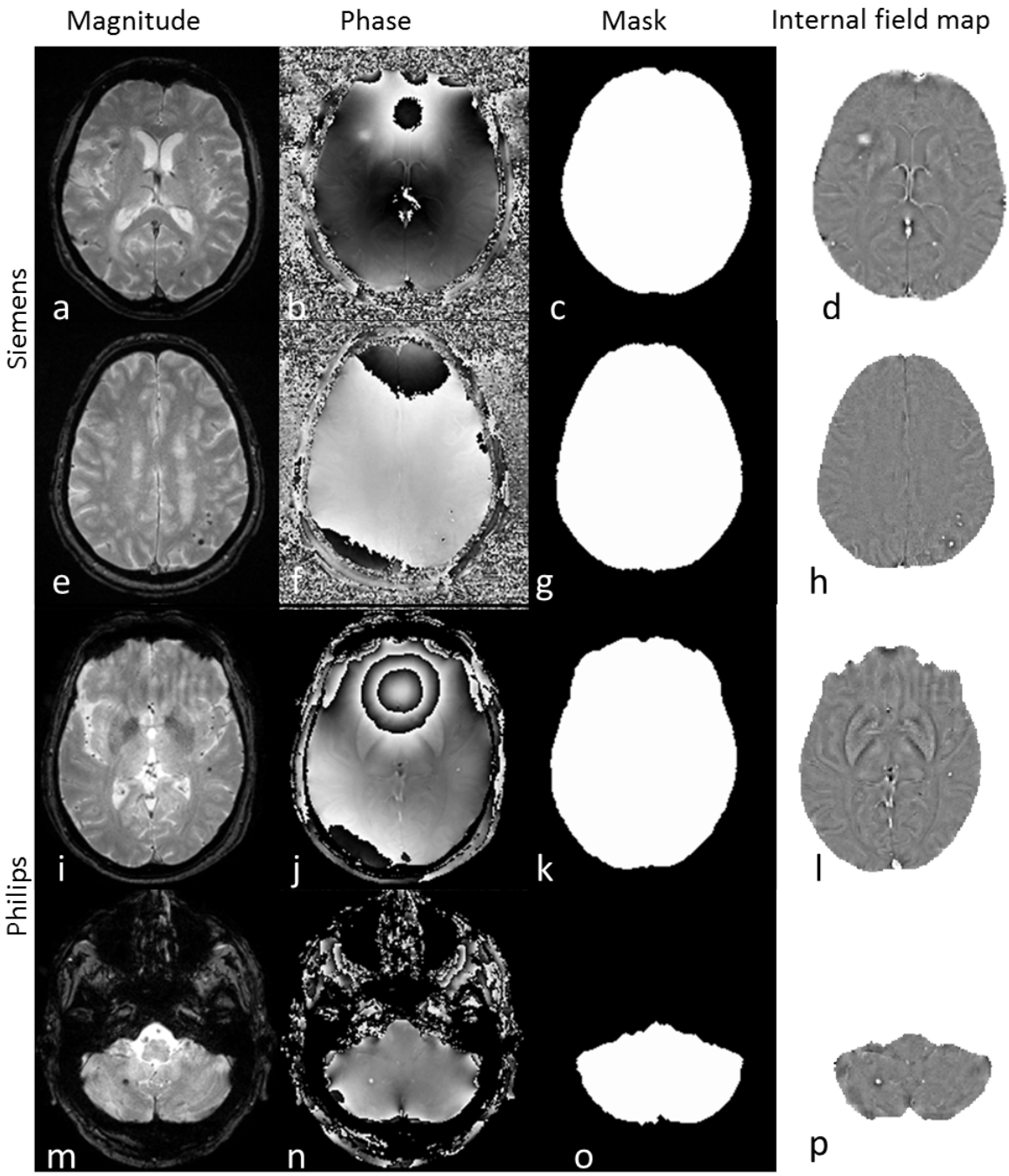

Figure 2.4.3: Application of 2DHF to 2D T2* GRE phase data with CMBs in different locations. For each column: (a,e,i,m) standard T2*W magnitude image, (b,f,j,n) raw phase map displaying strong background effects, (c,j,k,o) brain mask and (d,h,l,p) internal field map. Rows 1 and 2 (respectively 3 and 4): data acquired on Siemens systems (respectively Philips).

2DHF gives a better contrast between lesions and the neighboring tissue.

2.4.4 Application: Magnetic signature of CMBs and CMCs with 2DHF

CMCs can easily be mistaken for CMBs in the magnitude image when they are small, round. In fact, they appear as focal hypointensities on magnitude images. Both CMBs and these mimicking CMCs are dot-like susceptibility inclusions. Figure 2.4.5 illustrates these two types of lesions for Siemens and Philips datasets. For these two patients, a physiologic calcification could be observed inside the ventricles (e.g. in the choroid plexus), visualized as localized round hypo-intensity areas on the magnitude image (Figure 2.4.5, a-d) (lesions indicated on the internal field map with black arrowheads in Figure 2.4.5, h-k). Other hypo-intensity areas, very similar in shape and size, were observed in the brain parenchyma, and assumed to be CMBs (white arrowheads in Figure 2.4.5, h-k). These dot-like inclusions behave like small magnetic dipoles and thus created magnetic field patterns similar to that of a dipole in the internal field map (Figure 2.4.5, h-k). Even if these local field patterns partly appeared in the raw phase map (Figure2.4.5, d-g), phase contrast was mostly dominated by background effects and phase wraps. The 2DHF derived internal field map enabled an efficient extraction of local effects around the signal voids, as shown in the zoomed-regions Figure 2.4.5, l-o), and calcifications appeared to have a negative phase shift while the inclusions considered as CMBs inside the parenchyma had the opposite phase shift. Sign inversion thus shown in the zoomed region by a ring-like effect in the axial view (Figure 2.4.5, l, n) and a dipolar pattern in the sagittal view (Figure 2.4.5, m, o), are emphasized by 1D intensity profiles through this region (Figure 2.4.5, p-s). CT-scans were acquired in a sub-sample of subjects in the MEMENTO cohort for attenuation correction of PET emission data. Despite the fact that these CT-scans were not designed for the diagnosis of calcifications, resolution and contrast remained sufficient to reveal calcifications of about 5mm. Ten subjects were thus visualized with the two modalities and the CT-scan confirmed what was observed on the 2DHF internal field maps in all cases. Two examples with brain CT-scans registered with SPM on the T2* magnitude image are shown in Figure 2.4.6. The first two columns display the subject shown in Figure 2.4.5 (a, b) and the CT-scan confirms the presence of the choroid plexus calcification; the T2*-hyposignal within the parenchyma that was seen as a CMB on the 2DHF internal field map remains invisible on the CT-scan, and the value on this region was below 100UH, thus increasing the probability that this lesion is indeed a CMB. The

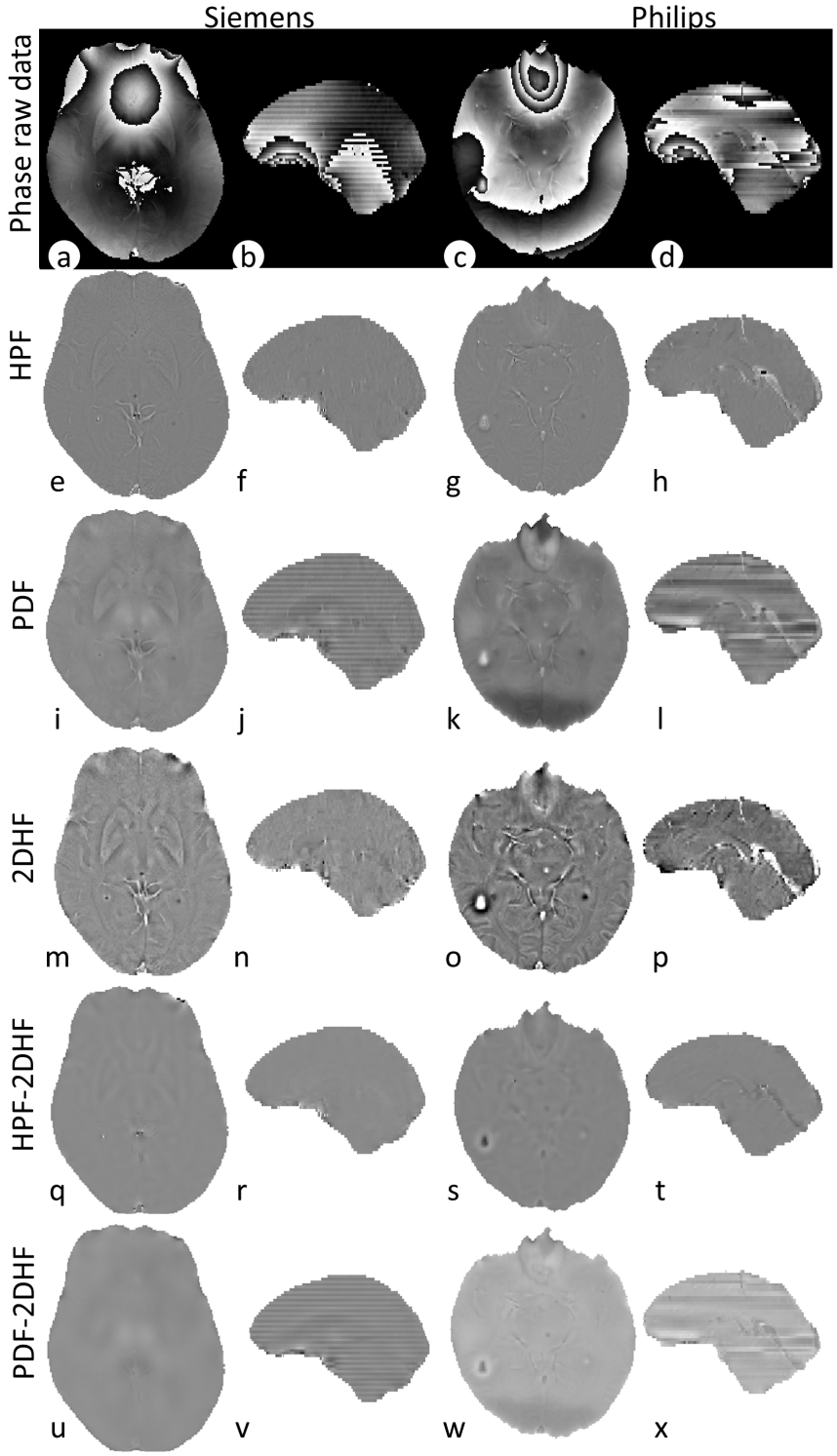

Figure 2.4.4: Siemens (left) and Philips (right) axial and sagittal views of raw phase data (a-d). Internal field maps computed with HPF (e-h), PDF (i-l) and 2DHF (m-p), image difference (HPF-2DHF(q-t)) and (PDF-2DHF(u-x)) displayed on axial and sagittal views.

other two columns illustrate another case with a dubious CMB on the T2* magnitude, that appears as a calcification on the CT-scan and also on the 2DHF internal field map; note that the 2DHF internal field map was computed here without eroding the brain mask, as the lesion was very close to the border.

2.5 DISCUSSION

This work presents a new efficient tool for background field removal in clinical multi-center setting. Unwrapping and local field estimation were simultaneously performed using a 2D version of a harmonic filter (2DHF), applied in Fourier domain. The 2D harmonic filter removes background effects while preserving local phase variations. This method showed good performance in retrieving fine 3D coherent details on 2D datasets on simulated and clinical images and allowed to identify a magnetic signature for CMBs and CMCs. When compared to state-of-the-art methods (HPF, PDF), 2DHF proved to provide more consistent detailed internal field maps for 2D datasets. Although differences between manufacturers are noticeable on raw data, 2DHF method allowed a good estimation of internal field map with preserved details for all 28 datasets.

Creating artifacts at the ROI borders is a common problem in filtering approaches used to remove background effects. In fact, the orthogonality assumption is no longer valid at the borders and these filtering approaches thus often fail to estimate the internal field map close to the ROI borders, in our case the brain boundary. In 2DHF, SPM masking prior to integration allowed limiting artifacts at the brain boundary. Furthermore, hypointensities close to large susceptibility artifacts (e.g. air-tissue interfaces close to the brain boundary) are rarely considered in the identification of CMBs due to the inherent uncertainty induced by the susceptibility artifacts. The remaining border effect at the brain boundary is thus unlikely to cause problems in CMBs identification.

The more common phase filtering approaches, such as HPF, rely on the assumption that the background field contributions only embed low spatial frequency components [Li and Leigh, 2001, Li et al., 2011, Schweser et al., 2013, 2012a, 2011]. Nevertheless, the background field may indeed contain high spatial frequency components and the local field may contain low spatial frequency components, and the resulting internal field map may thus be flawed. Furthermore, internal field maps obtained with HPF highly depend on filter size [Schweser et al., 2013]; for large filter sizes, small structures remain visible but the main part of phase information from

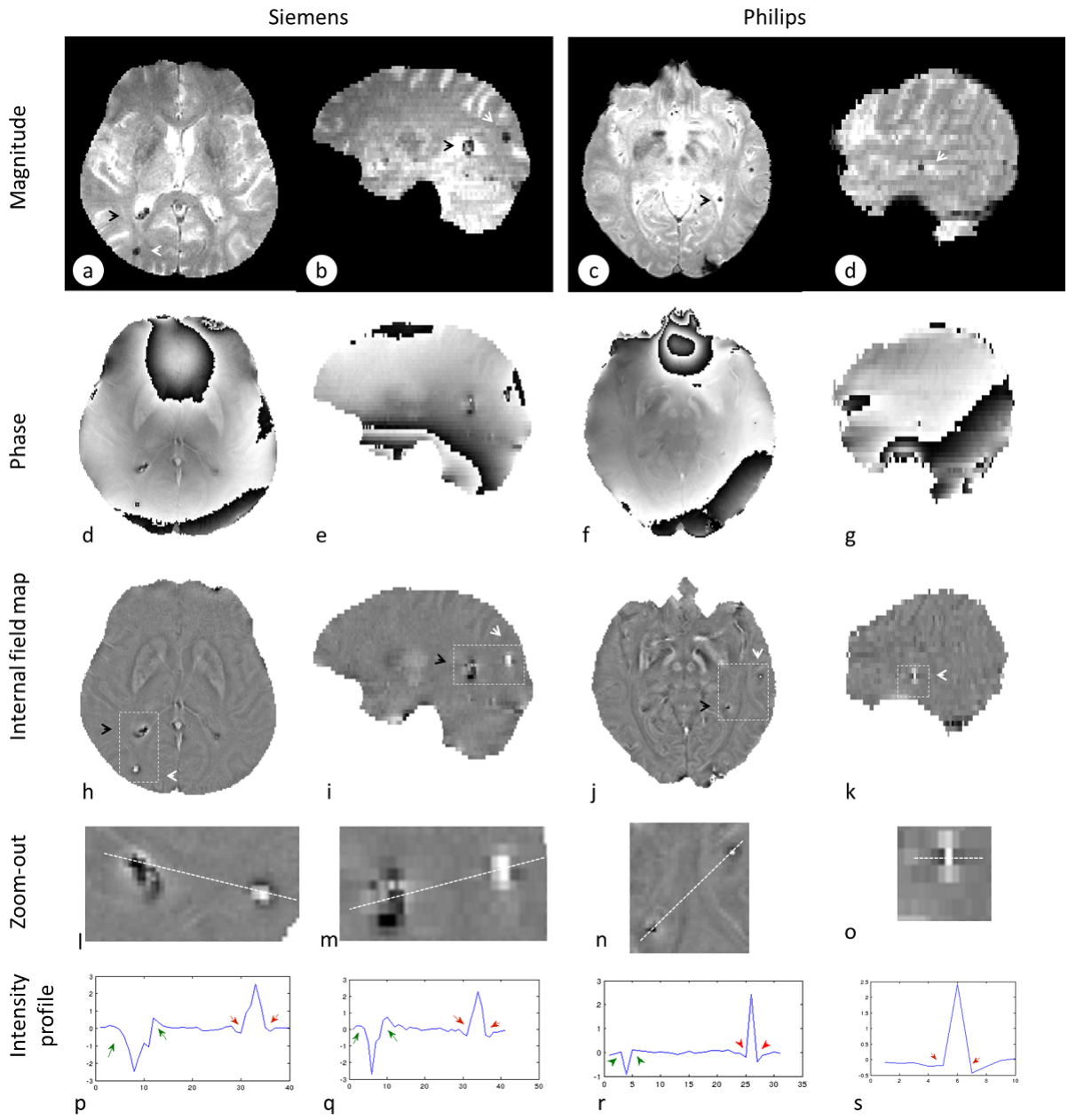

Figure 2.4.5: Siemens (left) and Philips (right) axial and sagittal views. Magnitude image (first row), native phase image (second row) and internal field map (third row). Fourth row shows a zoomed out region corresponding to the white rectangle showing CMB with a dipolar pattern (white arrow) and a physiologic calcification of the choroid plexus (black arrow). Note that panel l was rotated. A 1D intensity profile calculated through CMBs and calcification in the zoomed region is displayed in the last row. Note the intensity sign inversion for both side of CMBs (red arrow head), and the calcification (green arrow head). Double heads arrows on panels (l-o) indicate the location of the lines used to generate the intensity profiles.

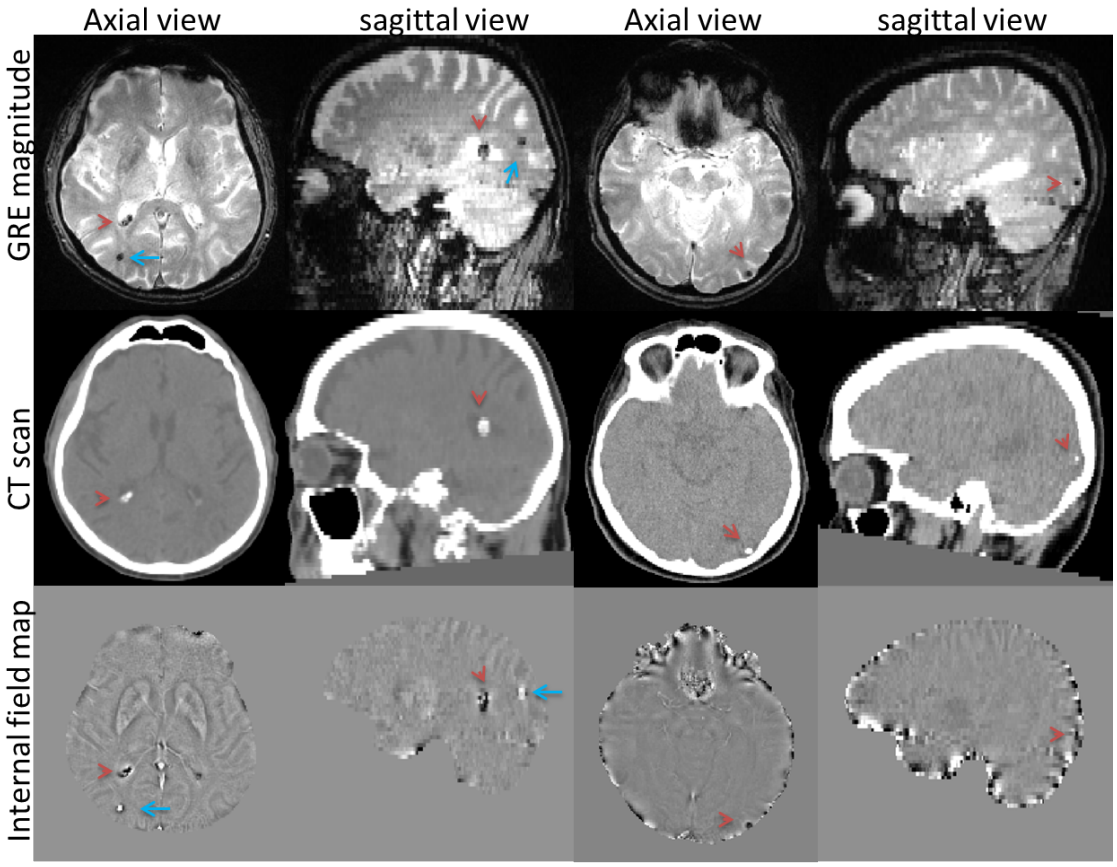

Figure 2.4.6: First example (2 first columns) is an illustration of a brain microbleed (blue arrow) and a physiologic calcification (in the choroid plexus) (red arrow head) on GRE magnitude image where both lesions appear with hypo-intensity (first raw); only the calcification appears as a hyper-dense area on the CT scan (middle raw); it corresponds to the hypo-intensity in the internal field map while the cerebral microbleed appears as hyper-intense. The second example (2 last columns) shows a hypo-intensity considered so far as doubtful microbleed, CT scan shows this lesion as a calcification; it corresponds to the hypointensity in the internal field map (red arrow head).

larger structures is removed. HPF is a heuristic method compared to 2DHF or PDF, which are both based on the assumption that background field is harmonic inside of the brain. This last assumption is derived from Maxwell's equations [Li and Leigh, 2001, Schweser et al., 2011] and is likely to yield less flawed internal field maps than HPF, which was confirmed by the results obtained here.

More sophisticated approaches proposed in the literature, such as PDF [Tian Liu et al., 2011], are computationally expensive. Most of these approaches were validated and recommended for data acquired with fully flow compensated 3D GRE sequences that are not always available in clinical routine. Furthermore, MRI data often suffers from various artifacts, such as motion, breathing or shimming artifacts, yielding slice-to-slice inconsistency in the phase map. Whereas the results obtained here showed that internal field maps generated with PDF showed slice-to-slice inconsistencies, 2DHF could remove this artifact while preserving details in local field maps.

Even though some multi-center studies have been undertaken with 3D acquisitions [Evans, 2006, Shive et al., 2013], large scale multi-center clinical studies are likely to be restricted by various constraints, such as the involvement of both research and clinical centers or an extensive acquisition protocol aiming at studying various aspects of a given pathology in a limited acquisition time. 2D acquisitions may thus be preferred, being faster, more robust to movement, and easier to standardize in multi-center setting. Nevertheless, some intrinsic differences remain between manufacturers, such as the differences between Philips and Siemens regarding the definition of multi-slice interleaved acquisitions or specific reconstruction issues. Although it may be possible to visually identify lesions with PDF in the acquisition plane, the remaining differences between Siemens and Philips derived internal field maps due to different inter-slice artifacts may bias the analysis undertaken with PDF. On the contrary, 2DHF yields 3D-consistent internal field maps in both cases and should thus allow more robust multi-center analyses.

However, background field correction is a three-dimensional problem and reducing it to two dimensions may result in some limitations. Omitting the z-term of the 3D Laplacian corresponds to assuming that all background sources that have an effect on a given xy-slice are located in the same xy-slice. This assumption is not always met, since the effect within the ROI may come from background sources located above or below the given xy-slice. However, when dealing with

2D acquisitions in clinical setting, anisotropy along z is large, slice thickness being most of the time above 2mm, with ~1x1mm² in plane resolution. In our case, voxel size is 1x1x2.5mm3, with a slice thickness of 2.5mm. In 2DHF method, derivations are computed as point-by-point differences divided by the voxel size. It implies that the second order derivative along z would be 2.5^2 times smaller than along x or y, thus reducing the error due to the 2D approximation in this context. Moreover, the internal field map is computed with 2DHF for each slice independently from all other slices; this should enable the use of 2DHF for data acquired in 2D with an inter-slice gap.

Visual identification of CMBs on MR images is a major issue in clinical practice and is made less reliable by the large influence of MR imaging parameters/sequences on CMBs appearance. MR-based imaging techniques have been investigated to better detect them. Susceptibility weighted imaging has been considered as a good candidate to address this issue [Ayaz et al., 2010, Nandigam et al., 2009], SWI retrieving 67% of CMBs missed on conventional T2* GRE. However, vascular structures along z may be highly ambiguous on SWI and are thus considered as a confusing factor for CMBs detection [Hammond et al., 2009]. Moreover, a post-mortem study suggests that iron content in CMBs can be accurately related to prominent phase image features [McAuley et al., 2011]. Preprocessed phase images thus appear relevant in CMBs detection and internal field maps provided by 2DHF are good candidates for improving CMBs detection in clinical settings. Simulated results have demonstrated a very high sensitivity of phase contrast to very small susceptibility variations, either paramagnetic (+0.125 ppm for simulated CMBs) or diamagnetic (-0,125 ppm for simulated CMCs).

Small CMBs may be considered as point dipoles, when observed through internal field maps. In fact, theoretically, when observed far from the magnetic source, the field generated by this source tends to the one of a point dipole with strength proportional to total magnetic moment [Jackson, 1999] p168, regardless of the source's shape. Even if CMBs are not all perfectly focal, 'small' inclusions will always behave like magnetic point dipoles. Since CMBs are paramagnetic, their resulting magnetization is in the same direction as $\vec{B_0}$. Therefore they correspond to positive values in the internal field map, and should appear with a sign inversion around the peak, typical of a point dipole field. This property was correctly retrieved with 2DHF and could be used as an attribute to better discriminate CMBs from confounding lesions and structures.

In the data evaluated in this study, resulting field maps clearly reveal the different orientation

between the "dipole field" generated by intra-parenchymal hemorrhages/CMBs and the one generated by calcifications. Although CT-scans dedicated to the diagnosis of calcifications were not available in this study, CT-scans for attenuation correction of PET emission data were available in a sub-sample of subjects, with sufficient resolution to allow confirming the results displayed by the 2DHF internal field maps in all 10 subjects visualized with both modalities. Other confounding signal voids can be confused with CMBs, such as vascular related signal (veins), rare angiomatous malformations or symmetrical focal basal ganglia iron deposits. The internal field map may play a role together with other sequences and priors in order to differentiate them from CMBs.

We have presented here a new time-efficient and robust filtering method for computing internal field maps from phase images of T2* GRE 2D acquisitions, based on 2D harmonic filtering. Simulation and in vivo results have shown that 2DHF allows generating more appropriate internal field maps than PDF and HPF for discriminating CMBs in our multi-center dataset acquired in clinical setting. It removes 2D acquisition and / or reconstruction artifacts while keeping fine details with limited border effect. Furthermore, 2DHF allows visualizing the dipole field patterns created by CMBs and CMCs. Thus, being fast and applicable to standard clinical 2D acquisitions, 2DHF could provide an efficient tool for making CMBs detection and discrimination more efficient from MRI acquisitions in clinical setting.

Some issues remain for phase-based lesion characterization. Some recent experimental findings have shown that phase contrast does not only depend on magnetic susceptibility and chemical shifts, but also on tissue anisotropy and its orientation with respect to the main magnetic field [Li et al., 2012, Schweser et al., 2010a]. These intricate dependencies make the understanding of magnetic susceptibility variations from phase images even more challenging. Recently, QSM has been assessed as an alternative tool for CMBs measurements. Its major claim here was to overcome the blooming effect and thus give a precise estimate of CMB's extent. Indeed, total susceptibility of CMBs measured with QSM has been shown to be consistently related with size measurements [Liu et al., 2012]. An increased detection sensitivity of CMBs when compared with GRE magnitude imaging was demonstrated. However QSM techniques are still under investigation, have mainly been focused on 3D acquisitions and need further validation to be applied in clinical setting. Furthermore, micro-structure-related offsets also yield artifacts in the reconstructed susceptibility maps [Wharton and Bowtell, 2013].

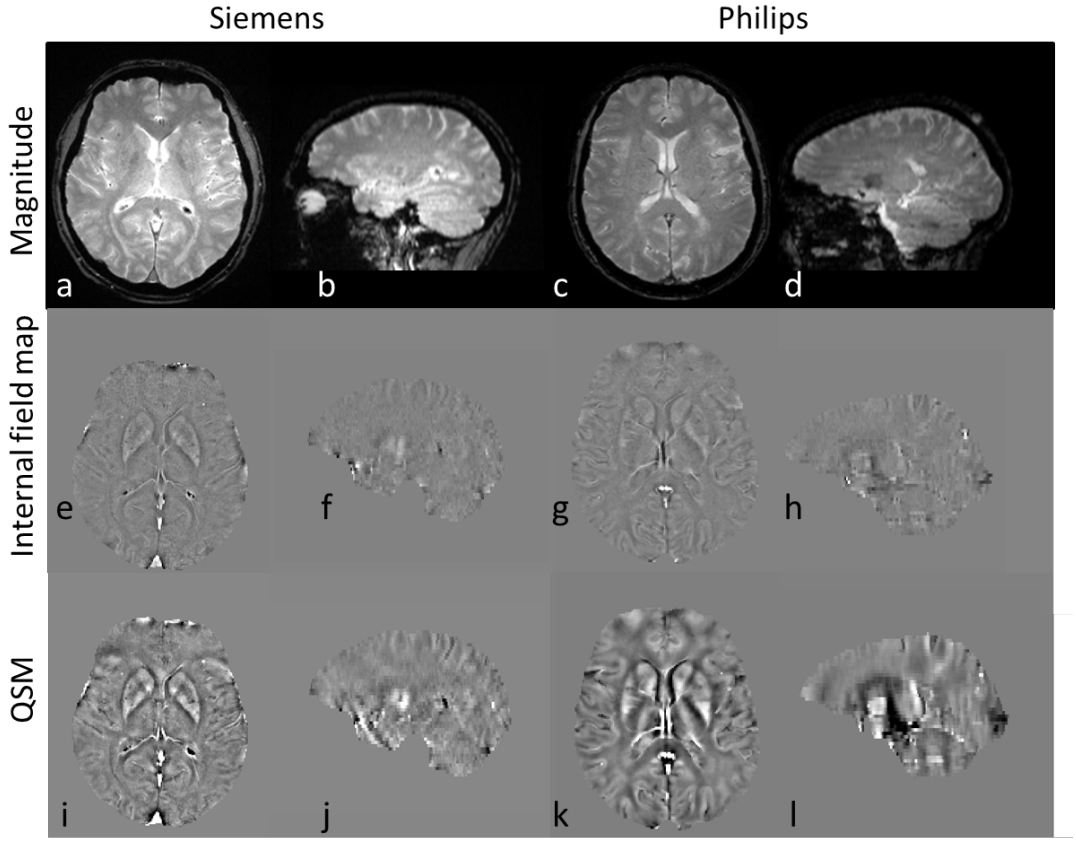

Figure 2.5.1: 10 Proof-of-concept: Susceptibility maps for Siemens (left) and Philips (right) datasets: QSM ((i-l) were reconstructed from internal field maps (e-h) generated by 2DHF.

In this study, the filtered phase was not yet used for QSM reconstruction. Further study will be necessary to investigate the influence of 2DHF on subsequent QSM analysis and the feasibility of reconstructing QSM maps from 2D datasets. Figure 2.5.1 illustrates a reconstructed QSM map with the method described in [de Rochefort et al., 2010b] for Siemens and Philips datasets, as a proof of concept of the feasibility of computing QSM maps from 2DHF-generated internal field maps. Magnitude image, internal field map generated by 2DHF and QSM map are displayed. An extended study will be necessary to evaluate the robustness of parameter setting in our complete dataset. Further details on QSM reconstruction using IFM are given in Appendix 2.

2.6 ACKNOWLEDGMENTS

The research leading to these results has received funding from the program "Investissements d'avenir" ANR-10-IAIHU-06 The Memento study is undertaken through the sponsorship of "Bordeaux CHU" and the financial support of "Fondation Plan Alzheimer". The funding sources had no role in the design and conduct of the study; collection, management, analysis, and interpretation of the data; preparation, review, or approval of the manuscript; and decision to submit the manuscript for publication.

The authors would like to thank Marie-Odile Habert and Sullivan Marie for their help with the CT-scans.

* * *

2.7 Conclusion

We have thus shown here that this new method could yield complementary information to better characterizing CMBs from MRI only. However, clinical usefulness still remains to be evaluated, either by a direct use in clinical rating or by an introduction as additional information in a multi-contrast segmentation framework.

To do so, we investigated clinical usefulness through a comparison study based on clinical ratings of randomly displayed images (either conventional T2* GRE magnitude, SWI or IFM) obtained from the same acquisitions. This will be presented in details in the following chapter.

Chapter 3

CLINICAL VALIDATION: A COMPARISON STUDY

Overview

The 2DHF method we propose thus makes it possible to process 2D phase images from multi-center clinical studies. Resulting internal field maps (IFM) appear a good tool to discriminate CMBs from cerebral calcifications. However, cerebral calcifications are not the only structures/lesions that mimic CMBs. To be of interest for clinical routine, the advantages of IFM for CMBs identification still remain to be assessed. We thus undertook a comparison study in order to evaluate if IFM yields similar or better performance for CMBs identification by experienced raters compared to more standard images. A pilot study was first undertaken with Anne Bertrand, neuro-radiologist, in order to select the most efficient images for clinical routine from a set of candidate images. A set of subjects with varying numbers of CMBs was then assessed by a team of raters with a wide range of background and expertise. The comparison study resulting for these experiments was submitted to Neuroimage Clinical[1].

* * *

[1] Improved cerebral microbleeds detection using their magnetic signature on T2*-phase-contrast: a comparison study in a clinical setting, Neuroimage Clinical (submitted)

3.1 INTRODUCTION

Cerebral microbleeds (CMBs), described as small foci of chronic blood products within brain parenchyma [Greenberg et al., 2009], were first seen on MRI sequences that are sensitive to magnetic susceptibility of patients with small vessel diseases. Correlation of these radiological findings with histopathological studies has generated considerable interest [Cordonnier, 2011]. CMBs are now commonly reported with MR imaging in the general population as well as in patients with specific disorders [Conijn et al., 2011]. CMBs' prevalence is highly variable among reports: from 47% to 80% in patients with intra-cerebral hemorrhage [Lee et al., 2004, Naka et al., 2004], from 8% to 71% in patients with ischemic stroke [Naka et al., 2004, Tsushima et al., 2003], from 17% to 46% in patients with cognitive decline and dementia [Cordonnier et al., 2006, Hilal et al., 2014] and 20% in healthy elderly population [Cordonnier, 2011]. Deep brain CMBs are associated with hypertensive arteriopathy (HTA), while superficial CMBs are associated with cerebral amyloid angiopathy (CAA), although they may also be present in patients with isolated cerebral small vessel disease [Park et al., 2013].

CMBs identification using MRI remains complicated [Cordonnier, 2011, Greenberg et al., 2009]. As made of hemosiderin, they can be described as strongly super paramagnetic iron–storage complexes [Cordonnier, 2011], whereas brain parenchyma is diamagnetic. Thus, this magnetic susceptibility difference with surrounding brain parenchyma makes CMBs appear as magnetic inclusions, causing local magnetic field inhomogeneity such as would be created by a unit dipole. At the voxel level, this field inhomogeneity leads to intra-voxel phase dispersion and strong T2*-contrast. CMBs' detection is thus commonly based on Gradient Recalled Echo (GRE) T2*-weighted magnitude images, in which they appear as areas of signal loss. However, their appearance on these sequences is sensitive to imaging parameters such as echo time (TE) and B_0 field strength. Furthermore, blood vessels and cerebral micro-calcifications (CMCs) also have strong T2* effects and can be misidentified as CMBs. While localization may help identification, such as for some physiologic calcifications commonly found in specific areas (e.g. pineal gland, choroid plexus, basal ganglia), discrimination between small blood products and calcification sometimes require a CT scan [Yamada et al., 1996].

Specific GRE-based solutions have been proposed to address these issues or related ones, including different scan protocols and/or different signal processing methods such as Susceptibility weighted imaging (SWI) [Cheng et al., 2013, Goos et al., 2011, Nandigam et al., 2009,

Vernooij et al., 2008], Enhanced Susceptibility weighted angiography (ESWAN) [Guo et al., 2013], Quantitative susceptibility mapping (QSM) [Klohs et al., 2011, Liu et al., 2012, McAuley et al., 2010], internal field maps (IFM) [Guo et al., 2013, Kaaouana et al., 2015]. SWI has already been considered for the diagnosis of CMBs. It is based on combining phase and magnitude images from 3D high resolution GRE images to allow enhancing detection sensitivity for paramagnetic structures such as veins or hemorrhages [Goos et al., 2011, Haacke et al., 2009, Haacke and Reichenbach, 2011, Nandigam et al., 2009, Reichenbach et al., 1997]. A comparison between SWI and GRE T2* reported that conventional GRE T2* magnitude missed 67% of CMBs compared to SWI [Nandigam et al., 2009]. In patients with CAA, [Cheng et al., 2013] and [Vernooij et al., 2008] reported that SWI was more reliable and sensitive for CMBs detection than conventional GRE T2* magnitude. Ayaz et al [Ayaz et al., 2010] reported that SWI is more suitable for longitudinal studies of CMB when studying 75 MCI over 4 years. The new ESWAN sequence (enhanced T2*-weighted angiography, combining a 3D GRE T2* multi-echo acquisition with a specific reconstruction algorithm) has been investigated for CMBs detection by quantifying phase values of CMBs in 75 MCI patients. The QSM reconstruction technique, aiming at quantifying susceptibility should allow for an estimation of the spatial extent of lesions, by removing the blooming effect; a validation study on 3D multi-echo GRE T2* acquisitions on 10 patients suspected of having experienced a stroke reported that the total susceptibility (TS) of CMBs was more consistent than CMBs size measurement [Liu et al., 2012]. Nevertheless, SWI, ESWAN and QSM techniques require a 3D multi-echo GRE T2* acquisition which may not be available in large cohorts. Internal field maps (IFM) can be computed with standard parameters from phase images of routine T2* GRE 2D single echo acquisitions. A method based on 2D harmonic filtering [Kaaouana et al., 2015] has been shown to allow for generating appropriate internal field maps for discriminating CMBs and visualizing the dipole field patterns created by CMBs; this magnetic signature could be used in CMBs' characterization.

Overall, CMBs' detection still suffers from high inter and intra-observer variability as well as large variation of reported prevalence between studies. This can be explained by confounding structures and artifacts as well differences in acquisition technique used in each study. Most of the new techniques that were proposed to address these issues were designed and applied to high resolution 3D acquisitions. As a result, previous studies comparing rating performance for advanced images vs standard magnitude images did in fact combine the advantages of 3D vs 2D

acquisition with those of the new pre-processing techniques. Here, we aimed at evaluating the specific advantages of advanced image reprocessing technique for CMB's identification by trained raters. In fact, 3D GRE T2*-weighted acquisitions may not always be possible in clinical setting and 2D acquisitions are still the safer mean to ensure uniformity in multi-center clinical studies and to guarantee reasonable acquisition time. Thus, routine 2D multi-slice GRE acquisitions were used as inputs in this study, resulting in several types of images that can be used for CMB rating: magnitude images, SWI-like images, and preprocessed phase images (IFM and QSM).

The paper is organized as follows. In the first part, the dataset used for this comparison study is presented, followed by a description of the advanced pre-processing techniques and comparison experiments. Results are then detailed in the second part, regarding the reliability of the reference built specifically for this study and the performance of the method both on a "single lesion" and "subject" point of view.

3.2 Material and Methods

3.2.1 Evaluation dataset

The evaluation dataset was extracted from data acquired for the ongoing French national cohort named MEMENTO [Chene et al., 2014]. MRI and PET acquisitions, provided by a network of 24 centers with MRI systems from different manufacturers, models and field strengths, are monitored by the CATI, the French National Platform for Multi-center Neuroimaging Studies (http://www.cati-neuroimaging.com/). A sub-sample of the first 382 MEMENTO participants were evaluated for CMBs [Kaaouana et al., 2015], and 77 subjects with CMBs were identified. This prevalence of 20% for this population (mean age was 55) was consistent with the prevalence reported for elderly subjects [Cordonnier and van der Flier, 2011]. For the current evaluation study, 15 subjects were selected to keep six subjects with numerous CMBs [13-30 CMB], five subjects with few CMBs [1-4 CMB] and four subjects without CMB. MRI data for these 15 subjects was acquired on either Siemens (four centers, Verio systems, seven subjects) or Philips (three centers, Achieva systems, eight subjects) 3T systems. The acquisition protocol was described in [Kaaouana et al., 2015].

3.2.2 Methods

CMBs are made of hemosiderin and are detected on GRE images because of the local magnetic susceptibility variation they yield. Besides, GRE phase images are proportional to magnetic field variations and thus sensitive to local susceptibility variations. Both magnitude and phase images will thus be considered in this study.

However, phase image analysis for local field variations is not straightforward. In fact, phase wraps appear on the images because phase is defined in the $[-\pi, \pi]$ interval and local variations are hidden in large scale field variations resulting from background effects, dominated by the magnetic susceptibility sharp edge of the air-tissue interface. Extraction of relevant internal field information requires two preliminary steps: phase unwrapping and background field removal [Haacke and Reichenbach, 2011]. These two pre-processing steps are embedded in the two methods chosen for this study, SWI and IFM, as described below.

3.2.2.1 Susceptibility Weighted Imaging (SWI)

SWI relies on combining phase and magnitude images [Haacke et al., 2009], phase information being used to enhance blood-related contrast on magnitude image (e.g. veins). Phase images are first high pass filtered (HPF) to extract local information and then transformed in a phase mask with values in the$[0; 1]$ interval. In this study, the HPF phase image was obtained through the following steps. Complex-valued image was first generated from magnitude and phase images. It was then low-pass filtered slice by slice with a two dimensional Gaussian filter in Fourier domain. The HPF phase image was then estimated as the phase component of the ratio between complex-valued and low-pass-filtered images. The HPF phase image was then transformed in a consistent phase mask which was then applied N times on the original magnitude image to highlight voxels with high phase value. The standard-deviation of the Gaussian filter, σ, and N were empirically chosen on the evaluation dataset in order to optimize the setting for CMB detection on 2D data. The σ parameter was set to 36 pixels [Haacke and Reichenbach, 2011] and N to 8.

3.2.2.2 Advanced phase image (IFM and QSM)

A 2D-based method for phase unwrapping and harmonic filtering, based on solving Poisson equation [Song et al., 1995], has been proposed as an efficient mean for obtaining the IFM [Kaaouana et al., 2015]. This method was shown to solve the potential slice-to-slice phase

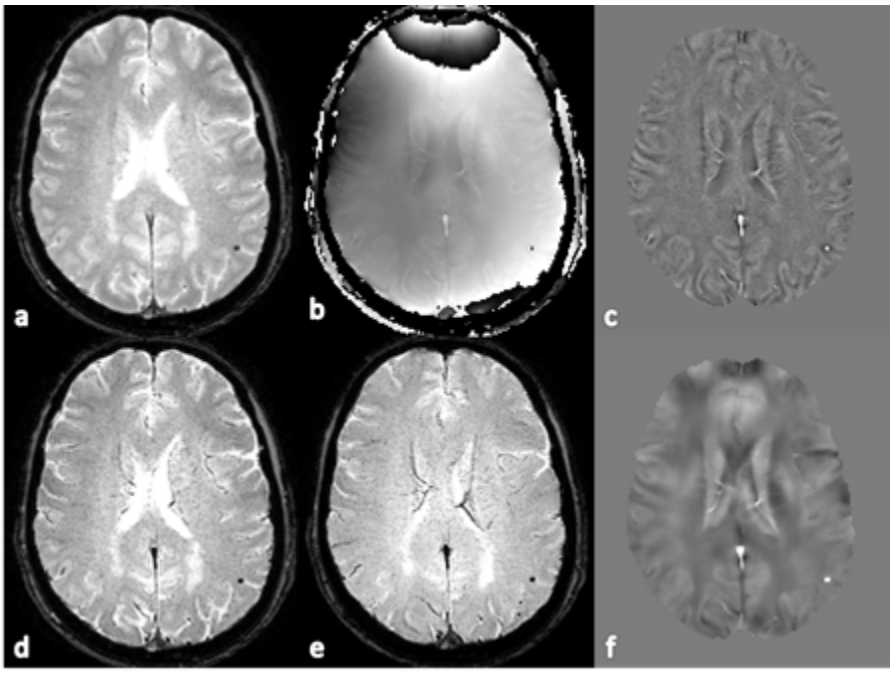

Figure 3.2.1: Magnitude image (a) raw phase image (b), IFM resulting from 2DHF (c), SWI (d), miP-SWI on 3 consecutive slices (e) and QSM map are displayed.

inconsistency that may occur in 2D multi-slice T2*GRE datasets. The magnetic field observed inside the brain, B, can be decomposed as the sum of the magnetic field due to internal sources, B_{in}, and the one induced by external sources, B_{out}. From Maxwell's equations, Bout is harmonic inside the brain ($\Delta B_{out} = 0$), resulting in $\Delta B = \Delta B_{in}$ (Δ denotes the Laplacian). Consequently, field variations due to external sources can be filtered out through a second order derivative, followed by a second order integration using adequate boundary conditions. In the process, the Laplacian of the field B_{in}, which locally depends on susceptibility distribution, is set to 0 outside the brain to remove external susceptibility effects. Paramagnetic dot-like inclusions appear as a dipolar field on the resulting IFM (see Figure 3.2.1 and [Kaaouana et al., 2015]). CMBs can be better discriminated by this magnetic signature.

IFM is not sufficient to fully evaluate the extent of each CMB, or even to isolate very close CMBs. QSM may be a good tool to assess CMBs with a more quantitative measure. From the above 2D IFM, QSM maps were derived using the method described in [de Rochefort et al., 2010a]. In-house optimization of hyper-parameters was used to better adapt the method to our 2D datasets.

3.2.3 Evaluation experiments

In order to determine the CMBs' influence of the type of image identification, rating was performed by several raters in different conditions. A pilot experiment was first carried-out in order to evaluate the experiment settings (see Figure 5.0.6 in appendix 3 for more details). Three types of images were finally considered as good candidates for CMB rating in clinical setting: T2* magnitude image, SWI-mIP image (mIP being done on 3 slices) and IFM image.

3.2.3.1 Rating comparison

Rating was performed independently by six raters with various levels of expertise: a trained clinical research assistant, a trained engineer, two junior neuroradiologists and two senior neuroradiologists. All observers were blinded to the image type and to clinical information. In order to facilitate detection, interactive setting was possible for visualization contrast though a specific Graphical User Interface (GUI) built with GUIDE in MATLAB (see Figure 3.2.2 and Figure 3.2.3). Because of the known variability of CMBs' detection, a certainty score was introduced, to allow categorizing CMBs as "definite" or "possible". The aim of this categorization was both to facilitate the rating in case of uncertainty and to differentiate the amount of variability that came from well-defined and badly defined CMBs. CMBs was defined as small round dots of signal loss that could not be followed on consecutive slices like vessels, on sequences that are sensitive to magnetic susceptibility. Their size may vary from 2 to 10mm.

3.2.3.2 Building-up of the reference

After the series of ratings was completed, a reference was built by two trained neuroradiologists, one of whom did not participate to the comparison experiments. All the CMBs that were detected by any rater from any image during the comparison experiments were reassessed independently by each trained neuro-radiologists, taking into consideration the three image types simultaneously though a specific GUI (reference GUI). These two sets of 15 reference images were then combined to create a set of 15 consensus images by a given explicit scoring rules (Table 3.2.1). Briefly, if a lesion is identified by both observers and at least one observer considers it as definite, then it is rated as "definite CMB" in the consensus. If it is identified by a single observer as "possible" then it is discarded from the reference; if it is identified by a single observer as "definite", then it will be considered as a "possible CMB".

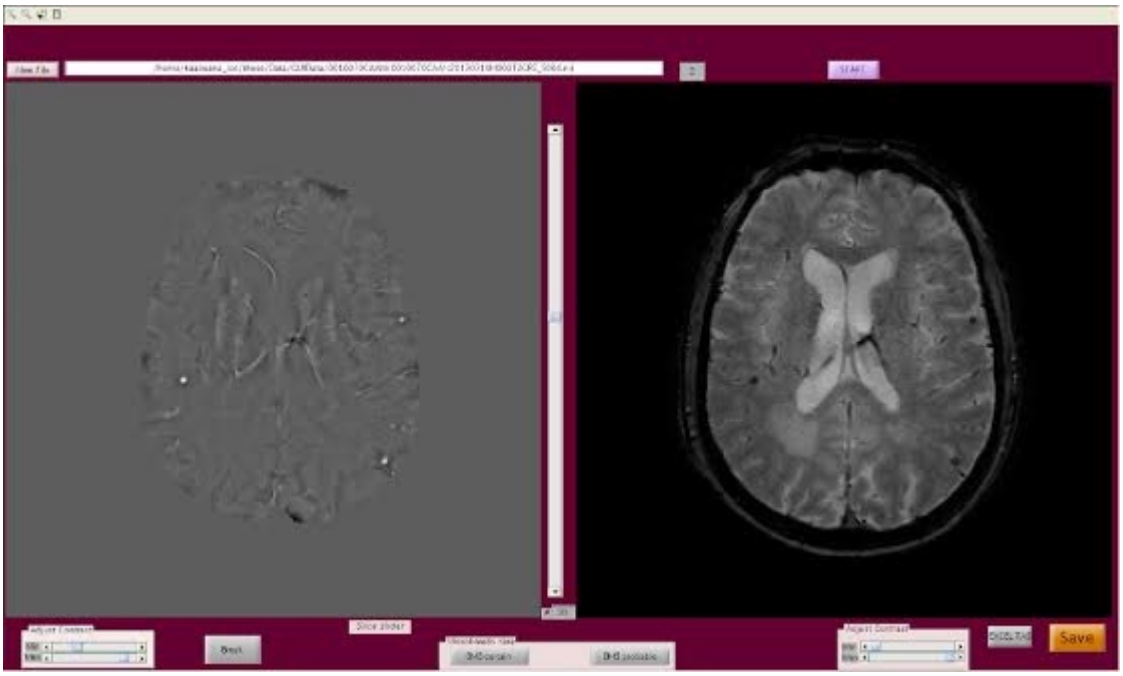

Figure 3.2.2: Evaluation GUI when IFM (on the left) is displayed (Magnitude image is on the right).

Figure 3.2.3: Evaluation GUI when SWI-mIP is displayed.

		Exp.1		
		0	1	2
Exp.2	0	0	0	1
	1	0	1	2
	2	1	2	2

Table 3.2.1: Reference consensus building up, scoring rules: 0 for discarded lesion, 1 for "possible CMB" and 2 for "definite CMB".

3.3 Results

Due to the well-known inter-rater variability when rating CMBs, the reliability of the consensus reference was first evaluated, in order to assess each following rating with respect to a meaningful reference. The evaluation experiments were analyzed on a lesion-based point of view through the rating results of the six raters with respect to the reference. Two types of identification were analyzed: 1. all CMBs detected (either definite or possible); 2. CMBs detected as definite only. Finally, in order to assess clinical usefulness, clinical practice was taken into account. In fact, the influence of few CMBs on clinical assessment is uncertain, whereas clinical practice focuses on subjects with numerous CMBs. Consequently, ratings and reproducibility analyses were carried out on a subject-type point of view, by classifying patients in three groups: no CMB (G1), few CMBs (G2, less than 10 CMBs) and numerous CMBs (G3, more than 10 CMBs). Furthermore, rating times were also analyzed, in order to evaluate clinical feasibility of IFM with respect to more standard T2* magnitude and SWI-mIP.

3.3.1 Reference

In order to evaluate the reliability of the consensus reference, CMBs detected by both expert raters were compared. Results are given in Table 3.3.1, through the number of detected CMBs (all or definite CMBs) for the two expert raters, the number of overlapping or discrepant CMBs detected by both raters and the consensus computed by the scoring rules described in Table 3.2.1.

Cohen's kappa coefficient was computed to compare the number of CMBs detected by each rater for each subject. When considering all lesions, the kappa value was 0.5 (p-value=0.01) and for definite lesions only, the kappa value was 0.54 (p-value=0.02). Overall, the agreement on CMBs detection was satisfactory. Apart from one subject (subject 3 with 13 discrepant CMBs), the discrepancy between both raters was negligible (median for "no CMB": 0, "few CMBs": 0

	expert.1		expert.2		Overlap / discrepancy			consensus	
subject	d	all	d	all	d/d	d/p	d/no	d	all
2	0	2	0	0	0	0	0	0	0
12	0	1	0	0	0	0	0	0	0
13	0	1	0	0	0	0	0	0	0
15	0	4	0	0	0	0	0	0	0
6	0	0	1	1	0	0	1	0	1
5	0	2	1	1	0	1	0	1	1
10	2	5	2	2	2	0	0	2	2
1	4	7	1	2	1	1	2	2	4
8	3	6	4	4	3	1	0	4	4
9	12	12	12	16	11	0	2	11	13
11	15	15	15	15	14	0	2	14	16
7	16	17	12	16	11	3	3	14	17
3	17	18	15	17	9	1	13	10	23
4	19	24	16	24	12	6	5	18	24
14	30	30	12	36	12	18	0	30	30
Total	118	144	91	134	75	31	28	106	135

Table 3.3.1: Reference building-up: CMBs detected by expert raters and consensus result. "d" refers to "definite" CMBs and "all" to the sum of definite and possible CMBs. "d/d" is the number of CMBs only detected as definite by both raters. "d/p" is the number of CMBs detected as definite by one rater and possible by the other, "d/no" is the number of CMBs detected as "definite" by one observer while not detected by the other, see Figure 5.0.6 appendix 4 for more details.

and "numerous CMBs": 2.5. Examples of between-raters discrepancies are illustrated in Table 3.3.1.

3.3.2 Rating results: lesion-based point of view

Blind ratings were analyzed with respect to the consensus reference, in order to evaluate the performance of each image type independently for lesion detection. Because of the large variability in lesion number between subjects, (TP), false positives (FP) and false negatives (FN) were computed for each rater over all the CMBs detected on all subjects. Note that "all" refers to "definite" and "possible" merged together. Overall count of CMBs detected for each raters are given in Table 3.3.2 for the three image types (T2* magnitude, SWI mIP and IFM). Total number of CMBs, TP, FN and FP are detailed for each rater.

Overall, IFM yields small improvements with respect to T2* whereas SWI-mIP yields systematic higher numbers of false positives. TP were lower for SWI than for T2* and IFM (78 vs 88-89). Both FN and FP were higher for SWI (FN: 57 vs 48-46, FP: 34 vs 16-9). Furthermore, ranges for TP, FN and FP were smaller for IFM than T2*(TP: 32 vs 54, FN: 32 vs 54, FP: 73

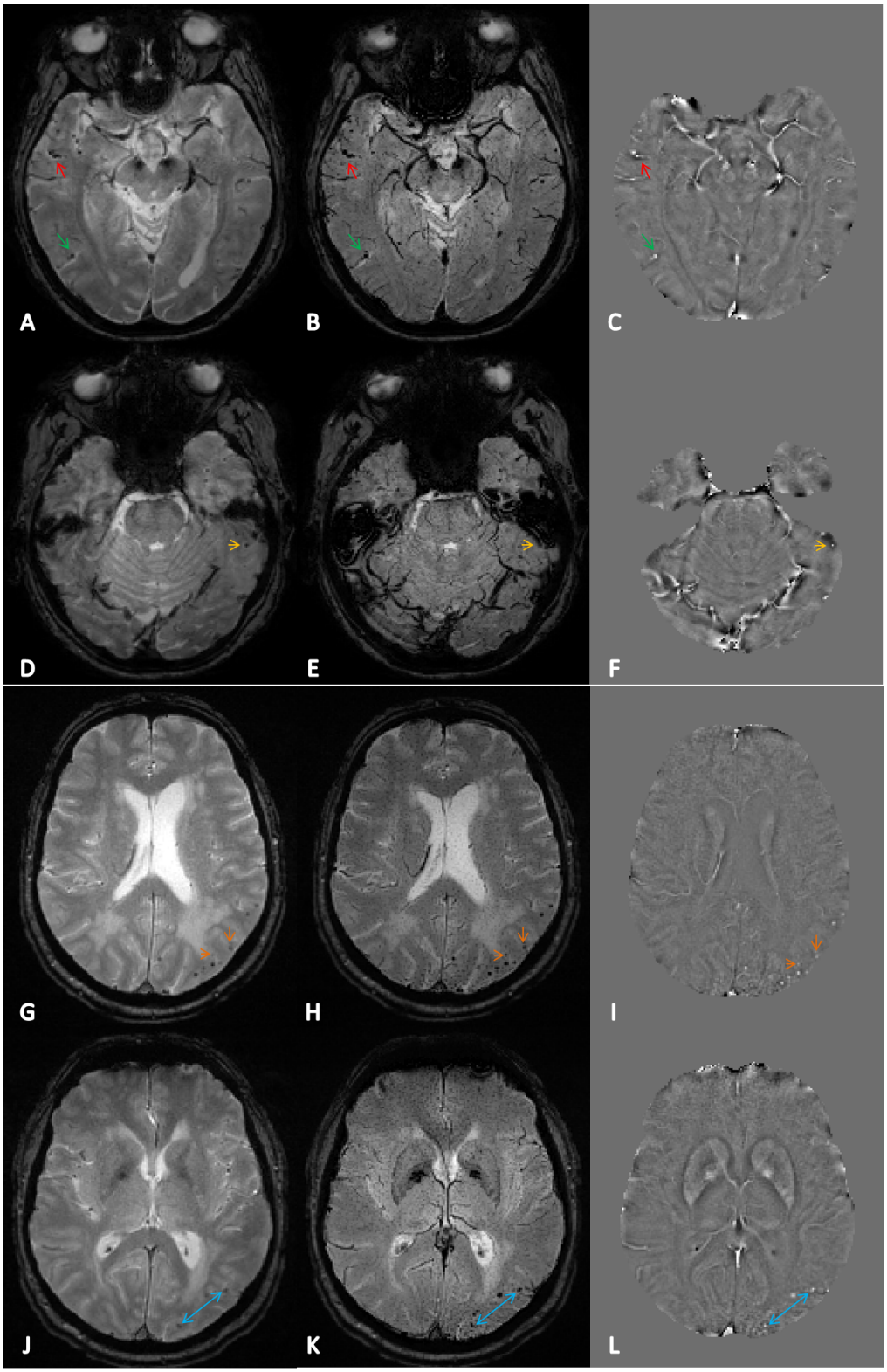

Figure 3.3.1: between-raters discrepancies during reference building-up; First column: magnitude images, second column: SWI-mIP images, third column: internal field map. First two rows: discrepancy cases from subject 3. Lesions shown here by red and green arrows are doubtful due to their shape that can be seen either as two adjacent round CMBs or as a relatively linear structure like a blood vessel. The CMB showed by the yellow arrow is very close to susceptibility artifact. Last two rows: discrepancy cases from subject 14. CMBs pointed by orange and blue arrows may have been ambiguous because of low contrast.

	Total number			∑TP			∑FN			∑FP		
	T2*	SWI-mIP	IFM	T2*	SWI-mIP	IFM	T2*	SWI-mIP	IFM	T2*	SWI-mIP	IFM
CRA	63	70	82	51	42	73	84	93	62	12	28	9
Exp.Junior1	82	81	89	74	65	86	61	70	49	8	16	3
Exp.Senior1	132	113	107	99	78	95	36	57	40	33	35	12
Trained. Ing	100	115	101	83	82	92	52	53	43	17	33	9
Exp.Senior2	107	119	84	92	78	78	43	57	57	15	41	6
Exp.Junior2	213	268	181	105	99	105	30	36	30	108	169	76
Median	104	114	95	88	78	89	48	57	46	16	34	9
Min	63	70	82	51	42	73	30	36	30	8	16	3
Max	213	268	181	105	99	105	84	9”	62	108	169	76

Table **3.3.2**: Total number of detected CMBs and comparison with the reference: True Positive (TP), False Negative (FN) and Positives ratio (FP).

vs 100).

When comparing performances between raters, we note that two raters tend to underestimate the number of CMBs (CRA and Exp.Junior1) and one tends to largely overestimate it (Exp.junior2). Interestingly, this difference is lessened by the use of IFM with respect to the two other image types (total count range: 99 for IFM vs 150 for T2* and 198 for SWI-mIP).

In order to better understand the detection pattern between raters, ratings for definite CMBs were also analyzed. Detailed results are given in Table 3.3.3.

Overall, the results are in accordance with 3.3.2. Total number of detected CMBs and comparison with the reference: True Positive (TP), False Negative (FN) and Positives ratio (FP). More specifically, IFM yields a higher number of definite CMBs than the other two image types (81 vs 72 and 66 for T2* and SWI-mIP, respectively) and smaller number of FN (25 vs 34 and 41) and FP (4 vs 9 and 19). Value ranges follow the same trend (TP: 23 vs 39 and 16, FN: 23 vs 39 and 46, FP: 14 vs 20 and 70). IFM thus seems to mitigate inter-rater variability for definite lesions (range for total number: 36 vs 55 and 108).

3.3.3 Rating results: subject-type point of view

In order to evaluate the three image types with respect to clinical usefulness, rating results were evaluated for each subgroup ("no CMB", "few CMBs", "numerous CMBs") (Table3.3.4).

The overall trend is confirmed for the subgroups, IFM yielding more specific results ((0 vs 2 and 2 for T2* and SWI-mIP, respectively for G1) and (1 vs 4 and 5 for T2* and SWI-mIP, respectively for G2) and (7 vs 13 and 27 for T2* and SWI-mIP, respectively for G3)), even if the performance is more balanced between methods for "no CMB" and "few CMBs" groups.

In order to better assess clinical usefulness, image types were compared regarding to their ability to correctly classify the subjects in the three groups of interest. The number of correctly classified subjects for each rater and each image type is given in Table 3.3.5.

Overall T2* magnitude and IFM classify better than SWI-mIP (median value: G1: 3/4 and 4/4 vs 2.5/4, G2: 2/5 and 2/5 vs 2/5, G3: 5.5/6 and 5/6 vs 4.5/6). IFM yields more similar results between raters than T2* magnitude and SWI-mIP (ranges: G1: 2 vs 3 and 3, G2: 2 vs 2 and 1, G3: 1 vs 4 and 4).

Table 3.3.6 indicates recorded rating time. Ratings from IFM took longer in most cases, but the relative difference decreased from participants with no CMBs to participants with numerous

	Total number			∑TP			∑FN			∑FP		
	T2*	SWI-mIP	IFM	T2*	SWI-mIP	IFM	T2*	SWI-mIP	IFM	T2*	SWI-mIP	IFM
CRA	56	54	66	47	38	62	59	68	44	9	16	4
Exp.Junior1	72	73	81	67	60	78	39	46	28	5	13	3
Exp.Senior1	87	74	88	81	66	84	25	40	22	6	8	4
Trained. Ing	76	87	91	67	65	85	39	41	21	9	22	6
Exp.Senior2	91	108	74	77	69	70	29	37	36	14	39	4
Exp.Junior2	111	162	102	86	84	85	20	22	21	25	78	17
Median	82	81	85	72	66	81	34	41	25	9	19	4
Min	56	54	66	47	38	62	20	22	21	5	8	3
Max	111	162	102	86	84	85	59	68	44	25	78	17

Table 3.3.3: Total number of CMBs identified as "definite" and comparison with the reference: True Positive (TP), False Negative (FN) and False Positive (FP).

		∑TP			∑FN			∑FP		
		T2*	SWI-mIP	IFM	T2*	SWI-mIP	IFM	T2*	SWI-mIP	IFM
G1 (N=4)	Median							2	2	0
	Min							0	0	0
	Max							10	5	4
G2 (N=5)	Median	4	3	4	9	9	8	4	5	1
	Min	3	2	2	4	7	6	0	3	0
	Max	8	5	6	9	10	10	31	7	19
G3 (N=6)	Median	82	76	85	41	48	38	13	27	7
	Min	48	38	70	22	27	23	5	12	2
	Max	101	96	100	75	85	53	67	160	53

Table 3.3.4: Rating results for all detected CMBs for each subject group (see Table 5.0.1 in appendix 5 for more details).

	G1 (N=4)			G2 (N=5)			G3 (N=6)			Total		
	T2*	SWI-mIP	IFM	T2*	SWI-mIP	IFM	T2*	SWI-mIP	IFM	T2*	SWI-mIP	IFM
CRA	3	1	2	2	3	2	2	1	5	7	5	9
Exp.Junior1	3	3	4	2	2	2	4	3	5	9	8	11
Exp.Senior1	1	2	4	3	2	4	6	5	6	10	9	14
Trained. Ing	4	2	4	4	3	2	5	5	6	13	10	12
Exp.Senior2	3	4	4	2	2	2	6	5	5	11	11	11
Exp.Junior2	1	3	2	2	2	3	6	4	5	9	9	10
Median	3	2,5	4	2	2	2	5	4,5	5	9,5	9	11
Min	1	1	2	2	2	2	2	1	5	7	5	9
Max	4	4	4	4	3	4	6	5	6	13	11	14

Table 3.3.5: Number of correctly classified patients using the three types of images.

	T2*	SWI-mIP	IFM	mean
G1 (N=4)	70	68	84	74
G2 (N=5)	58	47	54	53
G3 (N=6)	172	173	193	179
mean	100	96	110	

Table 3.3.6: Mean rating recorded time results by image type and subject-type in seconds.

CMBs. In the worst case, it took only 1.2 times longer. Interestingly, for all image types, it took less time to do the rating for participants with few CMBs than those with no CMB.

3.4 Discussion

We presented here a comparison of CMB detection performance when using three different kinds of images built from the same 2D GRE dataset: T2* magnitude image, SWI-mIP image, and IFM image. Ratings were performed in random order by six raters with varying background and level of expertise. Blind rating results were evaluated with respect to a reference built from a consensus between two raters, with good, agreement between both. Overall, 2D-dedicated phase processing used for IFM computation proved a very promising tool to improve CMBs detections in clinical setting; on lesion-based point of view, it yielded increased sensitivity and specificity compared to T2* magnitude and SWI-mIP images. On a subject-type point of view, even though performances were closer between the three image types, IFM yielded less inter-rater variability when identifying patients with numerous lesions than both other methods, with only a small increase in rating time, pointing toward clinical usefulness.

Here, our goal was to compare between CMBs detection on different techniques computed from the same 2D acquisition. Previous studies [Vernooij et al., 2008] compared 2D T2* magnitude images and 3D SWI, even though differences may be mainly due to the differences between 2D and 3D acquisitions. The aim of studying post-processing while keeping a single acquisition was motivated by the fact that 2D GRE T2* multi-slice sequences are more common in large multi-center cohorts than 3D multi-echo GRE T2*. For this kind of cohorts, IFM may thus be an efficient mean to improve CMBs detection. The method we used here, 2DHF, removes 2D acquisition and / or reconstruction artifacts while keeping fine details with limited border effect.

False positives in CMB detection can be explained by CMBs mimics, which have similar morphology and signal properties. Partial Volume Effect (PVE) is one of the main sources of mimics, but PVE-related mimics are more likely to occur adjacent to the petrous temporal

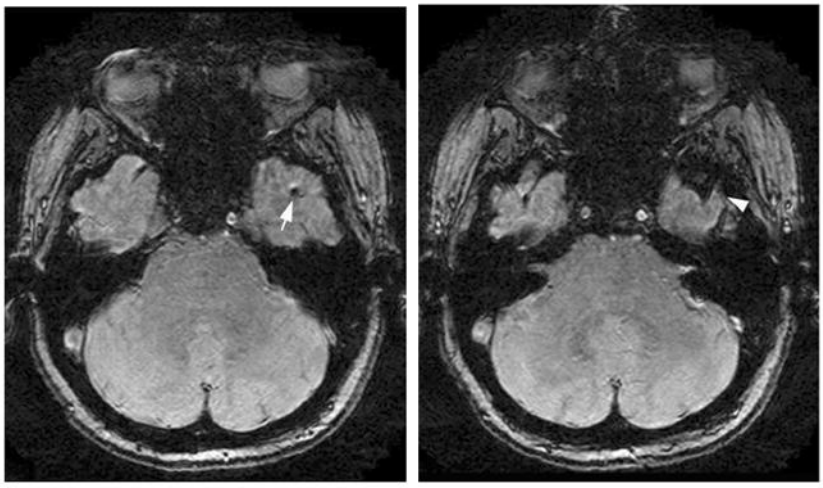

Figure 3.4.1: An axial T2*-weighted MRI image demonstrating partial volume artifact as a potential CMB mimic. The axial T2*-weighted MRI image on the left shows a round focus of signal loss (arrow) that could be interpreted as a left temporal CMB. The image just caudal to this (right) indicates that this hypo-intensity is due to partial volume artifact from the adjacent left sphenoid bone (arrowhead) [Greenberg et al., 2009].

bones, para-nasal sinuses, frontal bones, orbit and occipital bone [Werring, 2011, Gregoire, 2014, Greenberg et al., 2009]. An example of a partial volume artifact that mimic a CMB is illustrated in Figure 3.4.1. We notices that experienced raters better distinguish between PVE-related mimics and CMBs according to anatomical criteria.

Another frequent source of false positives is the appearance of venous structures non-parallel to the acquisition plane which are thus seen in cross-section as round objects. SWI-mIP may help to differentiate these vascular-related mimics, the projection allowing to highlight the 3D tubular shape, as illustrated in Figure 3.4.2.

Although the use of SWI with 3D-acquisitions is known to increase the contrast of CMBs, allowing to detect smaller CMBs, here SWI proved to increase FPs on 2D datasets. In fact, it may reveal flow voids from small blood vessels and enhance some hyposignal artifact, thus creating new mimics. Thus, the increased sensitivity brought by SWI is balanced by a decreased specificity. Moreover, the blooming effect is enhanced by SWI compared with magnitude images; this could lead to an underestimation of the CMB number when multiple close CMBs, biasing clinical decisions. Finally, high pass filtering technique has been shown to be sub-optimal for background field removal, crucial for SWI [Kaaouana et al., 2015]. This could yield an enhancement of some artefactual voxels resulting in an increased number of FPs.

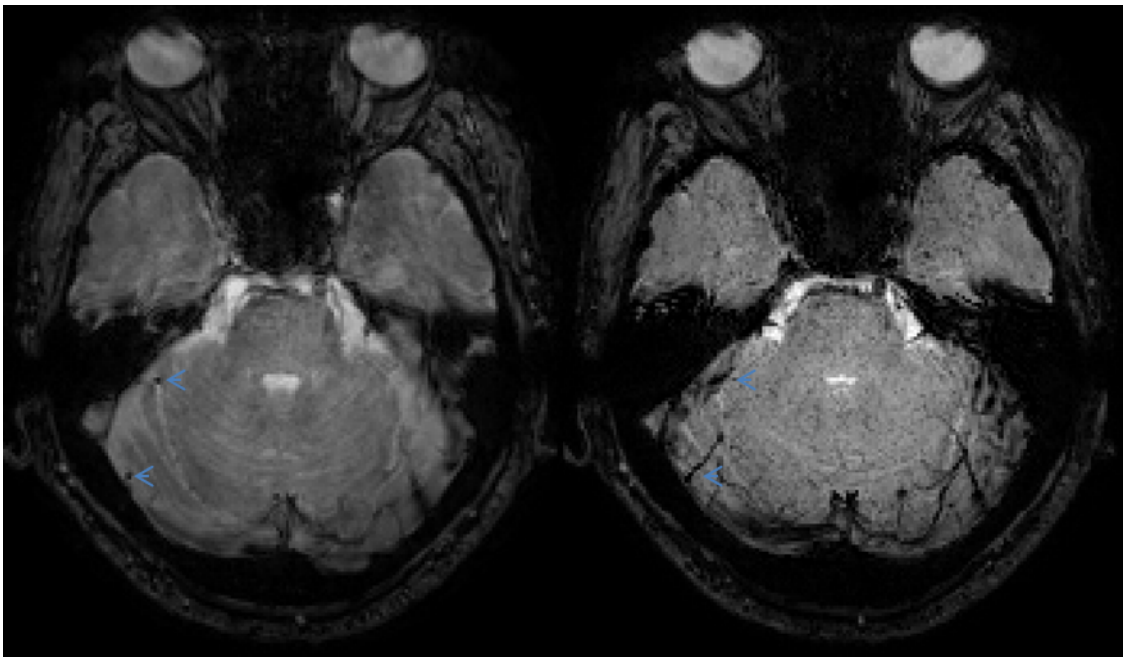

Figure 3.4.2: Example of FPs detected on magnitude image; these two hypointensities, pointed by blue arrows, were recognized as vascular-related mimics on SWI-mIP image because of their tubular shape.

The efficient calculation of IFM with the 2DHF method requires to express boundary conditions defining the "internal" region. These boundary conditions are thus derived from a mask of the region of interest, namely the brain. However, the border of the brain co-localizes with an area of strong susceptibility interfaces, thus leading to potentially strong border effects. To reduce the likelihood of these border effects in 2DHF, the brain mask was eroded. Theoretically, this may lead to miss the outer cortical part in some places, and thus cortical CMBs, as shown in the example in Figure 3.4.3. The use of both IFM and T2* magnitude images may help reduce the number of missed cortical CMBs.

QSM was not kept in the pilot experiment by the neuro-radiologist. In fact, applying QSM incorporates solving the dipole inversion which is intrinsically three dimensional and thus a strong anisotropic resolution may lead to large error propagation into the resulted QSM maps. Moreover, available techniques imply the setting of regularization/threshold which is a challenging issue for multi-center data. Here, the regularization parameter was empirically chosen. QSM needs more investigation and validation and clinicians may need more training to interpret resulted maps.

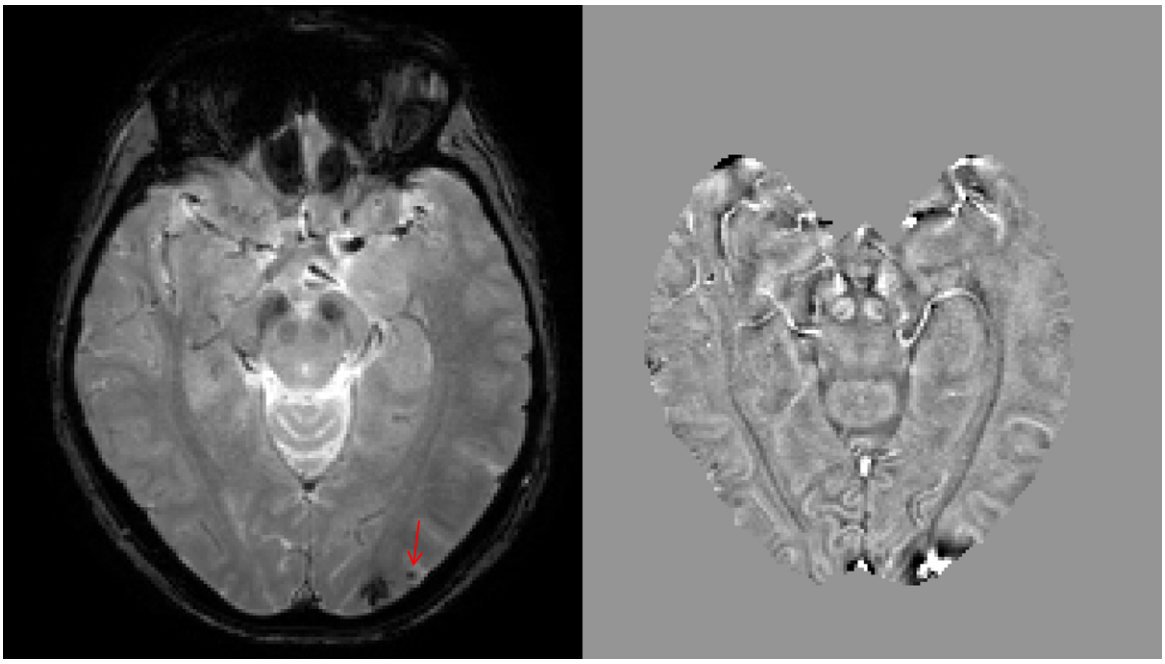

Figure 3.4.3: CMB on the outer cortical part not visible on IFM; Magnitude image shows 2 lesions (a spread lesion in the occipital lobe and a CMB (red arrow)). The hemorrhage was still seen in the IFM while the CMB disappeared due to masking operation.

Similar to SWI, IFM enhances the contrast of paramagnetic structures (Figure 3.4.2), which results in a increased number of TPs with respect to magnitude image. However, compared to SWI, IFM further yields a magnetic signature of CMBs. In fact, these inclusions behave like small magnetic dipoles and thus create magnetic field patterns similar to that of dipoles; this dipolar magnetic field appears as a ring-like effect in the axial plane in IFM. The sign of the ring like pattern varies if the lesion is either paramagnetic or diamagnetic and allows to discriminate between CMBs and cerebral micro calcifications related mimics [Kaaouana et al., 2015]. Overall, IFM thus improve sensitivity (with respect to magnitude image) and specificity (with respect to SWI-mIP).This results in a better characterization of subjects between "few CMBs" and "numerous CMBs", the last group being the more important for clinical practice.

Sensitivity and specificity of CMB detection appeared to be highly rater related among raters. Three types of rater behavior were noted: two raters identify less CMBs on all image types and thus tend to under-rate (CRA and Exp.Junior1); one rater largely over-rates (Exp.Junior2); the last three raters had a similar tendency for medium rating (Trained.Ing and the two Exp.Seniors). For the two "under-raters", IFM is more sensitive and more specific than

T2* magnitude and SWI-mIP. By contrast, for the "over-rater", sensitivity is very high for all image types, but most extra CMBs were identified on SWI-mIP and specificity is twice better for IFM than T2* magnitude and SWI-mIP. For raters the most experienced raters, all image types have a comparable sensitivity but IFM shows better specificity.

Regarding rating times, IFM proved efficient, even though it was a new image type for all raters. This time may be reduced with a better visualization of the magnetic signature and more practice. Important difference in rating time was noticed between the three groups; volumes with higher CMB number needs more assessment time. Raters may tend to double check volume without CMBs which can explain the longer time to do the rating for participants with no CMB than those with few CMBs.

For reference building-up, consensus was obtained with a specific scoring rule, in order to take into account the intrinsic variability of CMB detection (definite and possible CMBs). In fact, although the two observers reassessed the CMBs by considering all image types simultaneously, agreement was not perfect and a few cases of non-negligible disagreement were noticed. Even though relying a third observer or consensus meetings may have been more standard approaches, both may suffer from subjective bias, whereas our approach considered both observer equally.

Although studies on CMBs are increasing at an exponential rate, there is still a lack of precise standardized criteria for rating them, leading in a low inter-rater reproducibility within a project and an even lower inter-subject consistency. In fact, the main reasons of between-raters discrepancy are low contrast, distance with respect to sulci and lesion size. Better integrating new neuroimaging tools is likely to lead to considerable improvements with respect to these issues.

In this study, we have shown that IFM appears as an interesting add-on to magnitude image for the detection of CMBs. As expected, it allows discriminating mimics from real CMCs, visible "ring like" effects making it more specific in deep white/grey matter. On the contrary, magnitude only and SWI-mIP seemed to increase false positives detection. IFM offers a simple and practical solution to assess the presence, number and distribution of CMBs on standard clinical multi-center dataset. Further clinical studies on more subjects would help better assess the advantages of each type of images with respect to clinical usefulness, together with histological studies in order to infer the physical meaning of the magnetic signature. Finally, a comparison on 3D isotropic datasets would allow a better assessment of advantages of IFM with respect to SWI

when these datasets are available.

3.5 ACKNOWLEDGMENTS

The research leading to these results has received funding from the program "Investissements d'avenir" ANR-10-IAIHU-06 The Memento study is undertaken through the sponsorship of "Bordeaux CHU" and the financial support of "Fondation Plan Alzheimer". The funding sources had no role in the design and conduct of the study; collection, management, analysis, and interpretation of the data; preparation, review, or approval of the manuscript; and decision to submit the manuscript for publication.

* * *

Conclusion

Apart from indicating the usefulness of IFM in CMBs identification, this study allowed us to better understand the advantages and drawbacks of each of the candidate images. This will be of great interest when designing the segmentation tool, as it will give extra clues regarding the features of interest for the segmentation of CMBs. More precisely, SWI-mIP proved a good tool to distinguish elongated from punctual structure, by taking advantage of the projection process; however, elongated structures perpendicular to the projection direction could be mistaken for punctual ones if only one projection is kept. T2* magnitude image offers a better assessment of the distance between low signal lesions and sulci, and, overall, a better localization with respect to the parenchyma. IFM allowed disentangling more complex mimics thanks to the dipolar effect. The segmentation method would thus benefit of a design that would enable extracting features from multi modal input, either through a heuristic approach or within an optimization

framework.

Chapter 4

AUTOMATIC SEGMENTATION: Proof-of-concept

4.1 Introduction

The main objective of this thesis is the development of an automatic tool for CMBs detection on multi-center datasets in a clinical setting. State-of-the-art approach, as were shown, yield high false positives rate and need manual review to be reliable for clinical measures. This low specificity reveals the necessity to improve CMB characterization. The use of complementary phase information, very sensitive to hemosiderin, could thus reveal relevant additional features for CMB detection. In fact, existing methods were validated either on T2* magnitude or SWI images, the last one embedding phase image only to enhance susceptibility-related contrast. It has been shown in the previous chapter that IFM computed with 2DHF yield more specific information and improves CMB detection. The objective of our work is now to include IFM in a segmentation framework in order to improve specificity while keeping high sensitivity.

Challenges for designing an automatic identification method are related to CMB's nature: being a susceptibility artifact, other susceptibility artifacts may be mistaken to CMBs although their apparent shape may not be strictly round. Their size is variable ranging from very small to an unclear limit with macro hemorrhages. Furthermore, size

is a tricky criterion due to *the Blooming effect* that makes CMBs appear larger on T2* magnitude than on T2-weighted images. Adjacent CMBs may also overlap and either be mistaken for macrobleeds or badly separated. CMBs have a lot of mimics such as blood vessels, calcifications, cavernous malformations. Their appearance is sensitive to many imaging parameters such as echo time, field strength.

To solve all these issues while ensuring robustness and high specificity, the developed method has to rely on the differential diagnosis criteria of CMBs as giving in chapter 1.

Moreover, the comparison study presented in chapter 3 should help to better understand how each image type should be included in the segmentation method. In fact, IFM appears more specific than conventional T2* W and mIP-SWI, but T2*is useful for cortical CMBs that may be missed by applying brain mask. SWI helps to enhance small CMBs of low contrast and mIP-SWI better discriminate CMBs from veins if not parallel to projection direction. Figure 4.1.1 illustrates solutions that could translate each differential diagnosis criterion for an automatic identification scheme.

The development of a framework that embeds such features is a work in progress. The goal of this chapter is, thus, to present a proof-of-concept of the automatic identification tool for CMBs on a multi-center dataset. This tool should facilitate their study in large cohort context and, thus, improve the general understanding of their role in AD. The main novelty in this work is to include the multi-contrast aspect more specifically, the magnetic signature of CMBs on IFM as shown in [Kaaouana et al., 2015].

4.2 Proof-of-concept design

Considering shape, intensity and localization priors for CMBs, The first step aimed at looking for candidates CMBs. For this, we apply an empirical large threshold on T2* magnitude image, internal field map, SWI and mIP-SWI. This step allows to decrease the computational cost of processing the whole image and to prepare features extraction. A statistical threshold was used, keeping only outliers of a Gaussian distribution modeling

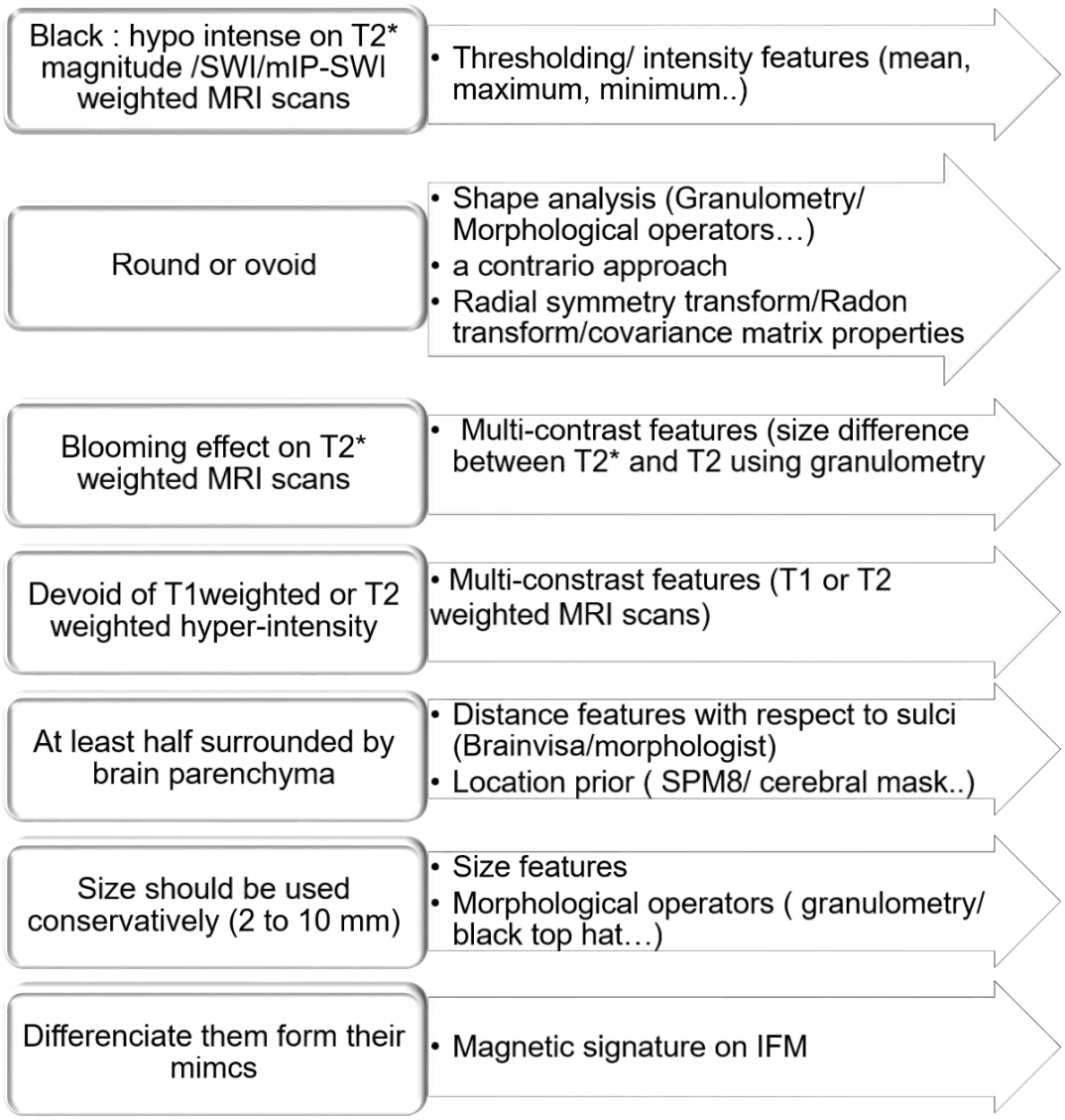

Figure 4.1.1: Image processing techniques that could translate the differential diagnosis criteria described in [Greenberg et al., 2009].

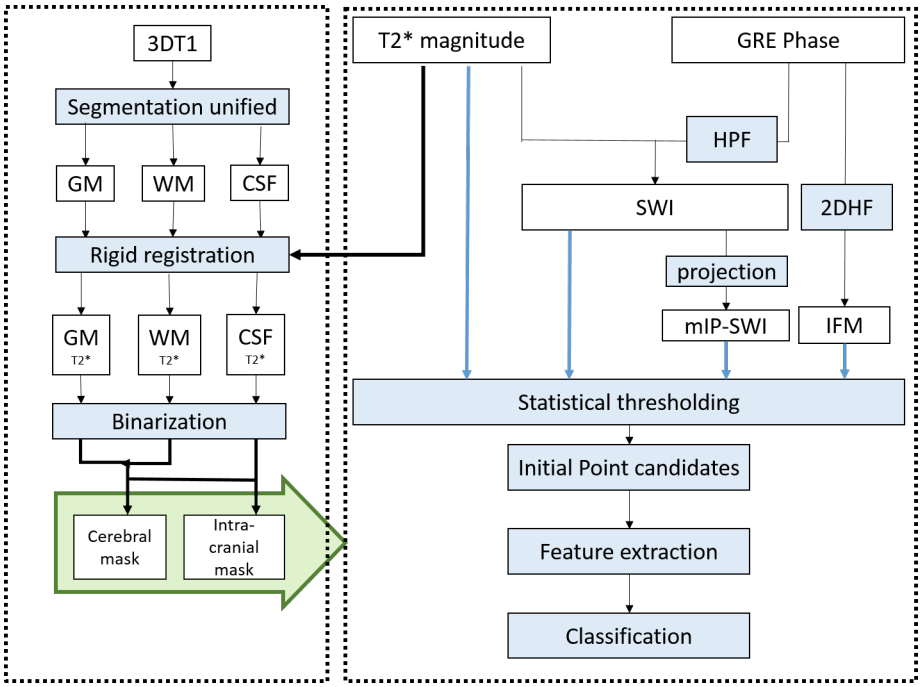

Figure 4.2.1: Illustration of segmentation scheme

intensity for the four types of images.

The second step consists of classifying these hypo-intense objects into three classes: definite CMBs, possible CMBs and other structures or artifacts resembling CMBs. To do this, a multi-contrast strategy was developed, based on a machine learning classification method with geometry, intensity related features. In Figure 4.2.1 the general model of our system is shown.

Prior localization information was derived from a brain mask generated during a pre-processing step described in the first section. The second section presents the proof of concept of the method including feature extraction and classification step. Preliminary results are presented in the third section while the fourth section will discuss these results and describes how this preliminary work could be extended to obtain the final framework to be used in clinical practice.

4.3 Pre-processing

MRI raw datasets often suffer from acquisition defects that need to be corrected before any further processing. The most common issue stems from B_1 field inhomogeneity that results intensity inhomogeneity over the magnitude image. Although manufacturers propose built-in solutions intensity inhomogeneities remains an issue. Image processing algorithms such as segmentation or texture analysis may not produce satisfactory results if this issue is not dealt with. On our multi-center Memento datasets, bias correction were performed using SPM tool.

Neuroimaging has greatly benefitted from the development of sophisticated and efficient algorithms for cerebral tissue segmentation which is now often done as a preliminary step. To do so, we used the "Unified Segmentation" method described in [Ashburner and Friston, 2005]. It uses a voxel-based approach with a statistical inference on the Gaussian Mixture Model. It is available in SPM which is a toolbox for Matlab developed by the FIL institute of Neurology, UCL (University College London) and is freely distributed on `http://www.fil.Ion.ucl.ac.uk/spm/`.

Most of the pre-processing steps we will describe below rely on Matlab batches using the SPM8 software.

4.3.1 3D T1 segmentation

The purpose of the "unified segmentation" is to extract probability maps of different cerebral tissues: white matter (WM), Grey matter (GM), cerebro-spinal fluid (CSF), skull, skin and the background. It is based on an atlas prior of each tissue in a standard space (MNI). It is usually performed on T1 weighted datasets because of the high isotropic resolution and good WM/GM contrast they embed. This method combines image registration (warping in Figure 4.3.1), tissue classification (segmentation in Figure 4.3.1), and bias correction as shown in Figure 4.3.1.

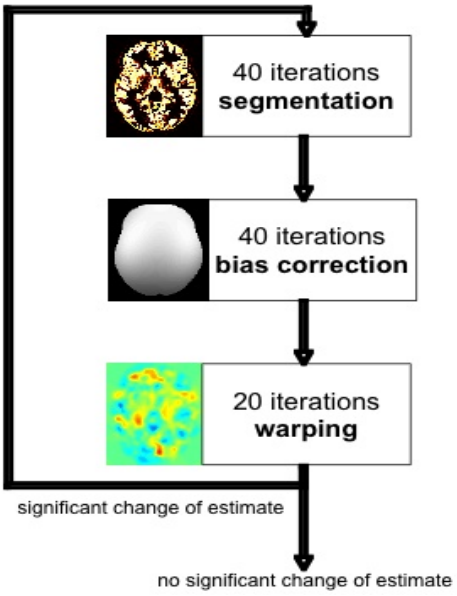

Figure 4.3.1: Unified segmentation illustration.

As mentioned before, non uniform intensity. It appears as a local variation of intensity in the same tissue without any pathological cause. Indeed, dealing with this issue is crucial for the intensity-based segmentation methods as these variations may modify signal distribution and therefore alter outliers interpretation. This is why this was included in the unified segmentation scheme. The module used here is New Segment and it is available from the batch editor in the menu SPM > Tools > New Segment; the input image to be segmented is the T1 image. The outputs are the T1 image with corrected bias, as well as the probability maps of GM, WM, CSF, skull and "other" class.

4.3.2 Affine registration

Image registration is the operation of aligning images in order to relate corresponding features. For most kind of image processing on two or more images, it is required that the images are aligned, so that one voxel position represents the same anatomical position in all images. It allows the use of images of different modalities; to compare or combine their respective information.

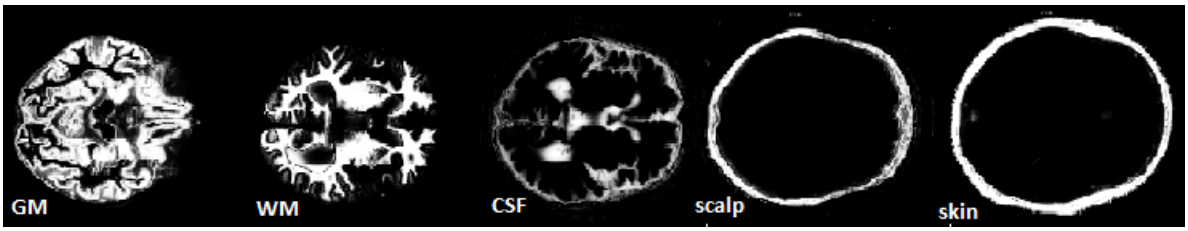

Figure 4.3.2: The tissular probability maps obtained by the "Unified Segmentation" and registered in the T2* space: from left to right respectively GM, WM, CSF, scalp and skin.

Registration aims at finding the transformation that matches exactly two images. This can be achieved by maximizing the similarity between source and target image

$$arg \max_{t \epsilon T} f\left(I_1, t(I_2)\right) \tag{4.3.1}$$

with f the similarity criterion, t the transformation to be applied to the source image (I_2), T the set of possible transformations and I_1 the target image.

The registration step is crucial for matching different contrasts (T1,T2*..) that are not acquired in the same space and with the same geometric parameters (FOV, slice selection...). Here, the registration is applied on images from the same subject which makes it reasonable to assume that the head will not be deformed. Hence, the rigid transformation model (3D rotation (x;y;z) and 3D translation (tx; ty; tz)) is therefore sufficient for our purpose. The Normalized Mutual Information (NMI) is the used similarity measure, as NMI was designed to compare data from different modalities/contrast. This measure is based on a multi-dimensional joint histogram which represents the co-occurrences of all possible voxels intensity combinations in the source and target.

We used the SPM module Coreg > Coreg: Estimate and Reslice. Input were the target image (T2 *image) and source image (the bias corrected T1 image). It is possible to add other images to be registered with the same transformation. Tissue probability maps generated by the unified segmentation were thus added. The output of this step thus were separate images, the 3DT1 and the five probability maps, one for each tissue class ; GM, WM, CSF, scalp and background (others), (see Figure 4.3.2).

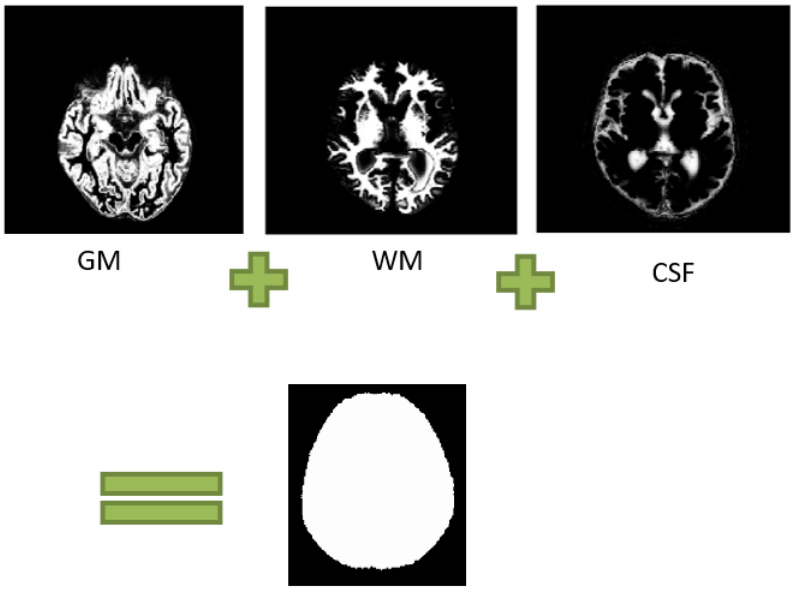

Figure 4.3.3: Intra-cranial mask calculation; First row probability maps obtained by SPM. Second row; final calculated intra-cranial mask when considering GM, WM and CSF.

4.3.3 Intra cranial and cerebral mask calculation

CMBs are only localized into parenchyma we thus define a region of interest to reduce the search area, corresponding to cerebral region. This made it possible to decrease the computational cost of the automatic detection.

For our method, tissue maps WM, GM and CSF registered in the T2* space, were binarized by keeping voxels with probabilities over 0.5 in the T2* space as shown in Figure 4.3.3. Two masks are thus defined: the union of WM and GM and CSF result in the intra-cranial mask while the union of WM and GM results in the cerebral mask. A hole filling is applied to the intra cranial mask to reconstruct a homogeneous region.

4.4 PROOF-OF-CONCEPT: Automatic CMBs identification

Identifying CMBs in an image can be addressed as a segmentation issue. Several approaches have been developed for image segmentation; thresholding, edge-based methods region-based methods. In medical imaging anatomical information can be introduced as

prior information in the segmentation.

Here we will address the issue by first selecting candidate voxels for CMBs and second classifying them according to a set of features.

4.4.1 Candidates selection: multi-contrast statistical thresholding

the aim of this first step is to analyze the images to find all the candidate CMBs. Thresholding was used to obtain initial CMBs candidates. Thresholding was used as the main characteristic of CMBs is their hypointense aspect. In thresholding, pixels are allocated to categories according to a selected range of defined by thresholds. The threshold value,th, is often chosen manually, by trying a range of values of th and directly assessing which value is more adequate to segment the object of interest. The threshold can also be chosen automatically based on data statistics. In our approach, we used statistically derived thresholds defined from means and standard deviations on a population. To decrease the number of detected objects and their size, we used the four images in this thresholding step: T2*, IFM, SWI and mIP-SWI images; the intersection between the four thresholded images was kept.

Statistical thresholding is of particular interest in the CMBs context. It can be used to separate the Gaussian distribution of the intensity of brain tissue from the low intensity outliers, CMBs, on T2*magnitude, SWI and mIP-SWI. The small size of CMBs preserves the Gaussian distribution without altering its mean and/or its standard deviation. However, these images also suffer from large susceptibility artifact that may alter their distribution. The statistical thresholding is performed in two steps:

Step1: The first threshold, th^I_{SA}, aims at identifying the *'large dark susceptibility artifact* (SA)*'* that may alter the real threshold, th_{CMBs} calculation on the image type (I). This threshold is empirically chosen as

$$\Omega_{IC} = \{x \in \Omega_I | \, M_{IC}(x) \neq 0\} \tag{4.4.1}$$

$$th^I_{SA} = \bar{x}_{\Omega_{IC}} - \alpha_{th} \times \sigma_{\Omega_{IC}} \tag{4.4.2}$$

where $\bar{x}_{\Omega_{IC}}$ is the mean intensity within the intra-cranial mask, M_{IC} and σ is its corresponding standard deviation. Voxels with intensity values below this threshold, Ω_{IC-SA}, are excluded when calculating the second threshold[1].

step2:

The second threshold, th_{CMBs}, is calculated using the same formula and it aims at keeping only CMBs:

$$\Omega_{IC-SA} = \left\{x \in \Omega_{IC} | \, I_{IC}(x) < th^I_{SA}\right\} \tag{4.4.3}$$

$$th^I_{CMBs} = \bar{x}_{\Omega_{IC-SA}} - \alpha_{th} \times \sigma_{\Omega_{IC-SA}} \tag{4.4.4}$$

$$\Omega^I_{CMBs} = \left\{x \in \Omega_{IC} | \, I(x) \leq th^I_{CMBs}\right\} \tag{4.4.5}$$

Both steps were performed for the three images,T2* magnitude, SWI and mIP-SWI. Illustration of these steps for each image is given, with their corresponding histograms, respectively in Figure 4.4.1, Figure4.4.2 and Figure 4.4.3.

Internal field map CMBs appear as hyper-intensities on IFM. The goal of the thresholding here is, thus, to separate the Gaussian distribution of background tissue from the high intensity outliers. A single threshold was sufficient. Threshold was, thus, written as

$$\Omega_{Cm} = \{x \in \Omega_I | \, M_{Cm}(x) \neq 0\} \tag{4.4.6}$$

[1]Here, Ω refers to the specified domain

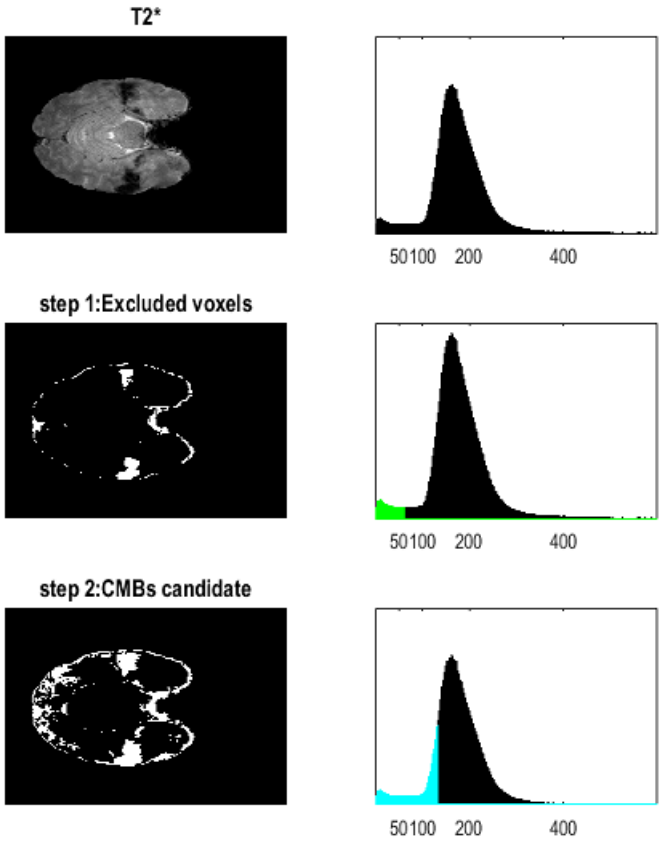

Figure 4.4.1: An example of T2* magnitude thresholding results and the corresponding histograms; in the first row, the T2* raw data and its histogram; in the second row white are the 'large dark susceptibility artifacts' excluded by the first threshold, green in the histogram; Third row are the resulting potential CMBs, Ω_{CMBs}^{T2*}, after applying the second threshold, th_{CMBs}^{T2*}.

$$th_{CMBs}^{IFM} = \bar{x}_{\Omega_{Cm}} + \alpha_{th} \times \sigma_{\Omega_{Cm}} \tag{4.4.7}$$

$$\Omega_{CMBs}^{IFM} = \left\{ x \in \Omega_{IC} | \, I(x) > th_{CMBs}^{I} \right\} \tag{4.4.8}$$

$\bar{x}_{\Omega_{Cm}}$ here, is the mean intensity calculated on cerebral mask (M_{Cm}), that includes Grey White matter without CSF and $\sigma_{\Omega_{Cm}}$ is the corresponding standard deviation. Results are shown in Figure 4.4.4.

CMBs candidates,Ω_{CMBs}, were thus found as

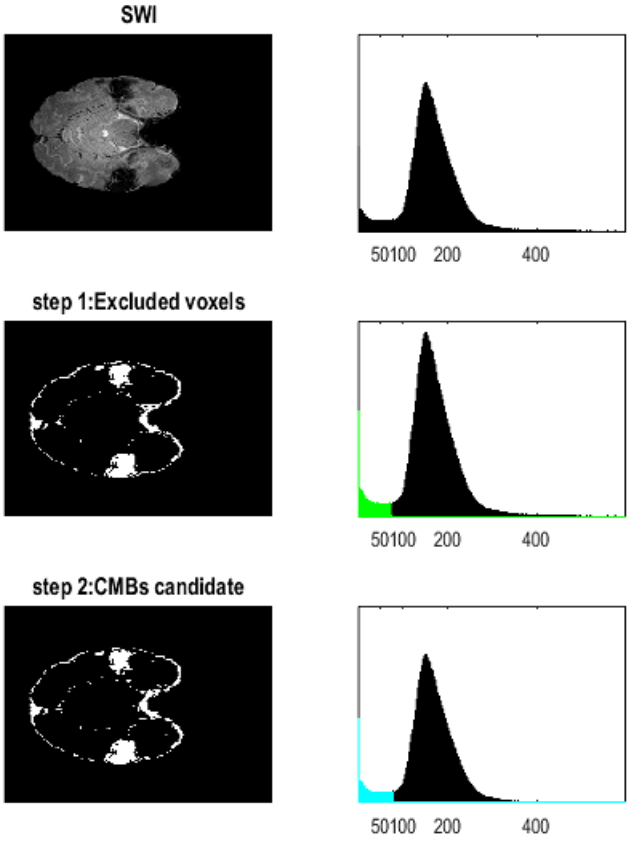

Figure 4.4.2: An example of SWI thresholding results and the corresponding histograms; in the first row, SWI image and its histogram; in the second row white are the 'large dark susceptibility artifacts' excluded by the first threshold, green in the histogram; Third row are the resulting potential CMBs, Ω^{SWI}_{CMBs}, after applying the second threshold, th^{SWI}_{CMBs}.

$$\Omega_{CMBs} = \Omega^{T2*}_{CMBs} \cap \Omega^{SWI}_{CMBs} \cap \Omega^{mIP-SWI}_{CMBs} \cap \Omega^{IFM}_{CMBs} \tag{4.4.9}$$

4.4.2 Classification

Segmentation can be formulated as a classification problem, in our case between "CMBs" and "non CMBs"; Given a dataset of images with known classification the system can predict the classification of new images.

A classifier-based segmentation requires the specification of two main items: the

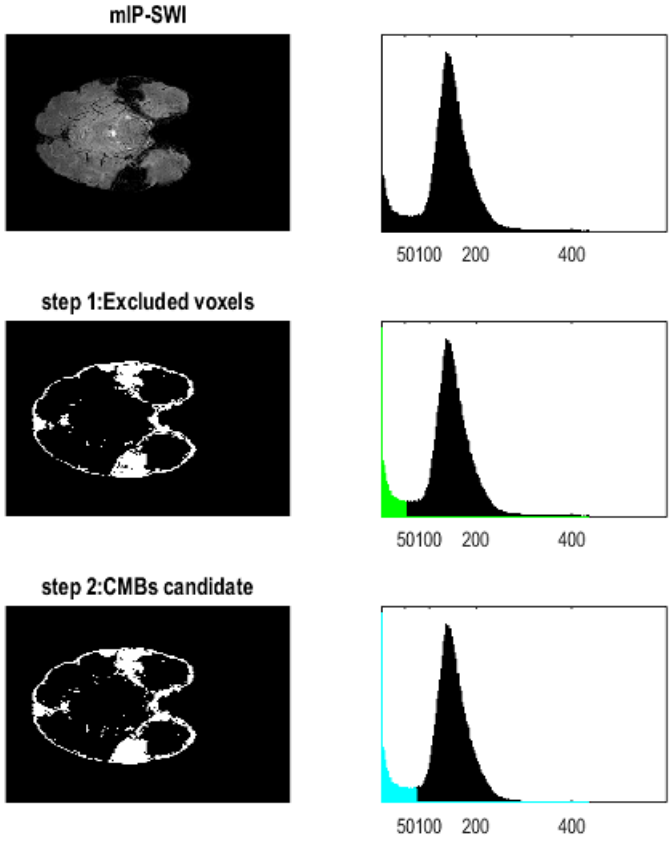

Figure 4.4.3: An example of mIP-SWI image thresholding results and the corresponding histograms; in the first row, the mIP-SWI image and its histogram; in the second row white are the 'large dark susceptibility artifacts' excluded by the first threshold, green in the histogram; Third row are the resulting potential CMBs, $\Omega_{CMBs}^{mIP-SWI}$, after applying the second threshold, $th_{CMBs}^{mIP-SWI}$.

feature vector and the classifiers itself. The feature vector consists of measurements derived from the image.

These features are then used by the classifier, a machine learning algorithm, to classify an unknown subject and its feature vectors given a learning set of feature vectors with or without known classifications. One of the main issues regarding classification is the key feature that allow better discrimination and the classifier model that allows better classification from the defined feature vector. Many classifier methods have been proposed; Supervised Learning uses training data with known labels to learn a model of

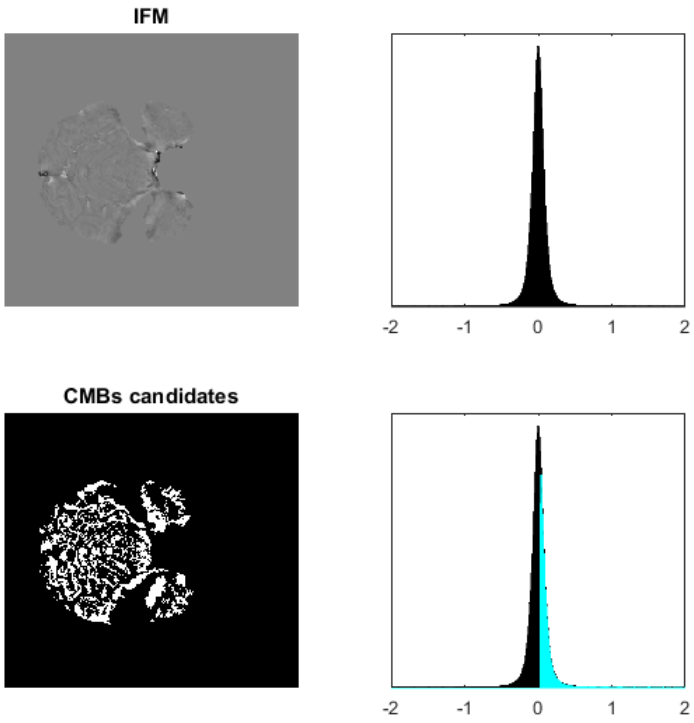

Figure 4.4.4: IFM distribution before and after thresholding.

the data, that is then used to predict new dataset. The well-known supervised learning techniques are generative methods such as artificial neural networks or discriminative methods such as Support Vector Machines (SVM). However, when there are no labeled data for training the classifier, unsupervised learning may be used. In this case the classifier has to find patterns in the data which is otherwise observed as unstructured noise. The most commonly used unsupervised learning techniques is K-means. However, real world problems are often subjective and resulting clusters might not adhere with it, semi-supervised learning may be used by incorporating user suggestions and feedback.

We will detail below the features that will be embedded within the feature vector and the building-up of the classifier based method. The general model of the classification step is shown in Figure 4.4.5.

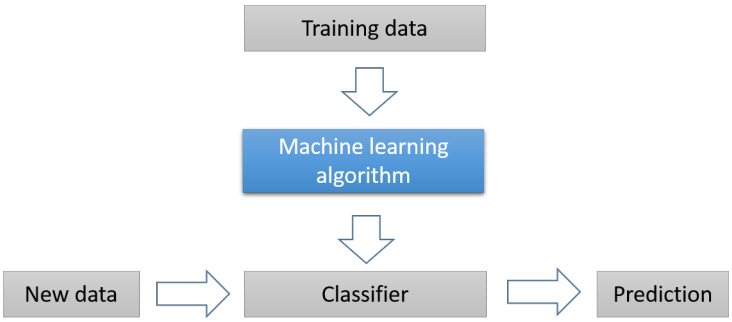

Figure 4.4.5: General model of a classification step.

Feature vector:

13 features were considered here for each candidate object:

- Three intensity features: mean intensity on T2*, SWI and IFM.
- Ten geometric features: mean value of FRST function applied on T2*, IFM, SWI and mIP-SWI; circularity; relative anisotropy; elongation; Effective circular diameter and the three eigenvalues of the covariance matrix.

The geometric features will be described below.

The circular shape of CMBs makes geometry a strong identifying aspect for CMBs detection. The first idea was to use the Function of Radial Symmetry Transform (RST) that was developed by Loy and Zelinsky [Loy and Zelinsky, 2003]. FRST is an image processing technique that can be used to highlight spherical-shaped objects in an image. A Matlab function is available on the website: http://www.nada.kth./~gareth/homepage/gareth_home.html. For each voxel in the image, the 2D FRST results in a so-called sphericity score. This score corresponds to the sphericity of a local neighborhood around the voxel. The neighborhood is evaluated at a distance n of every point; one or N radii can be evaluated, with N the radii vector. It further allows to highlight both hypo and hyper-intensities.

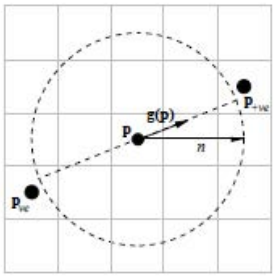

Figure 4.4.6: Illustration of negatively and positively affected pixels [Loy and Zelinsky, 2003].

Using a 3×3 Sobel gradient, the gradient of each pixel is computed. If a pixel p lies on the edge of a circular disk, then the direction of its gradient $g(p)$ is orthogonal to the edge, pointing to (if the circular disk is hyper-intense) or away from (if the disk is hypointense) the center of the circle. The pixel that is at a distance n pixels away from p along the direction of $g(p)$ is defined as a positively-affected pixel, given by

$$P_{+ve}(p) = p + round\left(\frac{g(p)}{\|g(p)\|}n\right) \tag{4.4.10}$$

Whereas the pixel that is at a distance n pixels away from p along the direction opposite to that of $g(p)$ is defined as a negatively-affected pixel, whose coordinates are given by

$$P_{-ve}(p) = p - round\left(\frac{g(p)}{\|g(p)\|}n\right) \tag{4.4.11}$$

where "*round*" rounds each vector element to the nearest integer and n is the radius of the circular features to be detected. These two points are illustrated in Figure 4.4.6.

For each radius n, an orientation projection image O_n and a magnitude projection image M_n are created, by going through all the voxels of the image, first initialized to zero and then incremented or decremented each time p is found as a positively affected or negatively affected as as follows

$$O_n(P_{+ve}(p)) = O_n(P_{+ve}(p)) + 1 \tag{4.4.12}$$

$$O_n(P_{-ve}(p)) = O_n(P_{-ve}(p)) - 1 \tag{4.4.13}$$

$$M_n(P_{+ve}(p)) = M_n(P_{+ve}(p)) + \|g(p)\| \tag{4.4.14}$$

$$M_n(P_{-ve}(p)) = M_n(P_{-ve}(p)) - \|g(p)\| \tag{4.4.15}$$

The radial symmetry contribution for radius n can be defined by this convolution

$$S_n = F_n * A_n \tag{4.4.16}$$

with

$$F_n(p) = \frac{M_n(p)}{max\,\|M_n(p)\|} \left(\frac{\left|\tilde{O}_n(p)\right|}{max\left\|\tilde{O}_n(p)\right\|} \right)^{\alpha} \tag{4.4.17}$$

where A_n is a 2D Gaussian and α is the degree of sphericity. FRST parameters will be more detailed below.

All these parameters need to be adapted to CMBs detection. The CMBs are in hyposignal on T2* magnitude, SWI and mIP-SWI; we thus want to detect using FRST only points from which the vector gradient points out. However, CMBs are hyperintense on IFM and thus, only points from which the vector gradient points away are needed to be hilight. We modified the available Matlab script so that it detects either only negatively affected pixels or only positively affected pixels. The algorithm of the FRST to highlight dark circular shapes is described in the algorithm 4.1.

The Radial symmetry function have a number of parameters that needs to be set:

1. The set of evaluated radii $N = \{n_1; n_2; ..\}$
2. The Gaussian kernel, A_n;
3. The degree of sphericity α ;

Algorithm 4.1 FRST algorithm when considering only dark circular shapes

1. Gradient image calculation using 3×3 Sobel operator
2. "Negatively affected pixels" calculation

$$P_{-ve}(p) = p - round\left(\frac{g(p)}{\|g(p)\|}n\right) \tag{4.4.18}$$

3. Orientation matrix calculation

$$O_n(P_{-ve}(p)) = O_n(P_{-ve}(p)) - 1 \tag{4.4.19}$$

4. Projection matrix calculation

$$M_n(P_{-ve}(p)) = M_n(P_{-ve}(p)) - \|g(p)\| \tag{4.4.20}$$

5. O_n et M_n scaling

$$F_n(p) = \frac{M_n(p)}{max\,\|M_n(p)\|}\left(\frac{\left|\tilde{O}_n(p)\right|}{max\left\|\tilde{O}_n(p)\right\|}\right)^{\alpha} \tag{4.4.21}$$

6. Convolution by a Gaussian

$$S'_n = A_n * \sum_n F_n \tag{4.4.22}$$

7. Sphericity score calculation for all radii $n \epsilon N$

$$S = \frac{1}{|N|}\sum_{n\epsilon N} S'_n \tag{4.4.23}$$

The FRST is a local approach based on the description of the neighborhood of a point. For every pixel, the neighborhood to be evaluated is determined by the radii vector N. According to [Greenberg et al., 2009], the size of CMBs varies between 2 and 10 mm; the aim here is, thus, to find the optimal set of radii that allows to detect CMBs. When considering a set of radii, the final sphericity score obtained is an average score for these radii. In order to better estimate this parameter, a synthetic image was generated with the graphical tool GIMP. Figure 4.4.7 present this synthetic image, which contains different shapes including disks of different radii and different linearity and sphericity. These structures may overlap to mimic overlapping CMBs. R corresponds here to N

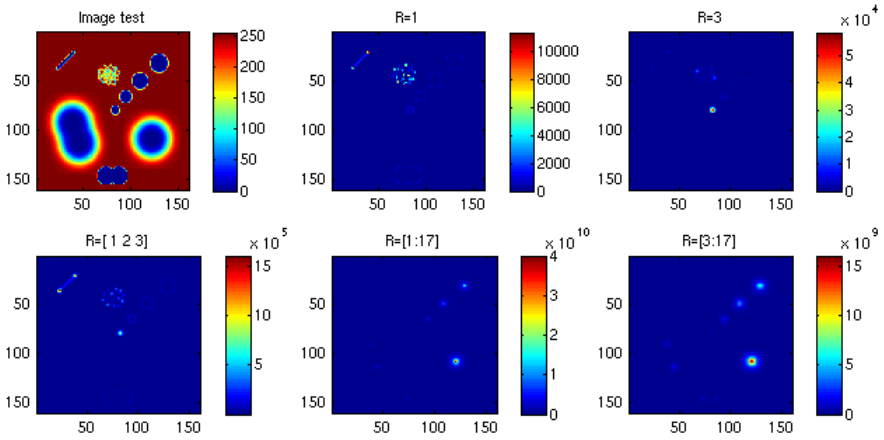

Figure 4.4.7: Illustration of the synthetic image generated by GIMP and the FRST results for different set of radii R.

in the previous part. FRST results on the synthetic image show that for $R = [1]$, the FRST detects the linear structures and the edges of the circular structures with strong gradient. For $R = [3]$, the FRST detects the spherical disk with small size as well as some points inside inhomogeneous structure.

For a range of radii $[1, 2, 3]$, the FRST highlights the linear structures, the spherical structures of strong gradient which size is within this range but also the edges of the spherical which size is larger than the target range. For a range $R = [1 : 17]$, the FRST detects only the spherical structures in the target range of radii (even those with low contrast). By comparing, the result of $R = [3]$ and R = [3,17], we notice that the disk of radius 3 was not detected. In fact, when looking for a wide range of radii, small radii are going to have scores significantly small with respect to larger radii.

The convolution by the Gaussian kernel, A_n is performed at the sixth step of the algorithm 4.1. The use of this kernel aims at spreading the influence of the positively- and negatively-affected pixels as a function of the range n. The chosen 2D kernel is invariant by rotation to have the same sphericity score for gradients with different orientations. Figure 4.4.8 shows the contribution for a single gradient element $g(p)$. By scaling the

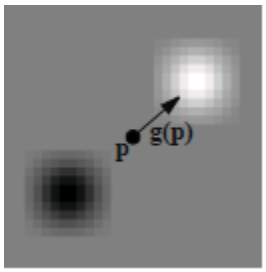

Figure 4.4.8: Illustration of the contribution of one gradient element with $\sigma = 0.25 \times n$ [Loy and Zelinsky, 2003].

standard deviation linearly with the range n, we define an arc of influence that applies to all affected pixels. The width of the arc is defined by scaling the standard deviation of A_n with respect to n.

Here, A_n is chosen to be a 2D Gaussian of size $n \times n$ and standard deviation $\sigma = 0.25 \times n$ as was recommanded by [Loy and Zelinsky, 2003]. Applying the Gaussian spreads out the score of sphericity σ pixels nearby.

Theα parameter defines how strictly radial the radial symmetry must be for the transform to return a high interest value. This parameter is used in the step 5 of the algorithm 4.1. A high α allows to detect very spherical points and eliminates non-radially symmetric features such as linear structures (vessels). Whereas, a small α allows to detect relatively spherical structures. In order to understand the impact of this parameter, we applied FRST with different α values on the same image generated with GIMP. It is important to note that, in the original work presenting the FRST [Loy and Zelinsky, 2003], the author considers that 2 is a suitable value for the most part of the applications.

As shown in the results in Figure 4.4.9, structures that are relatively spherical were detected for $\alpha = 1$ while they relatively disappeared for superior values. For $\alpha = 2$, the FRST starts to discriminate spherical points. We also notice that for $\alpha = 5$ and $\alpha = 7$, small disks are no longer detected although the radii vector was the same.

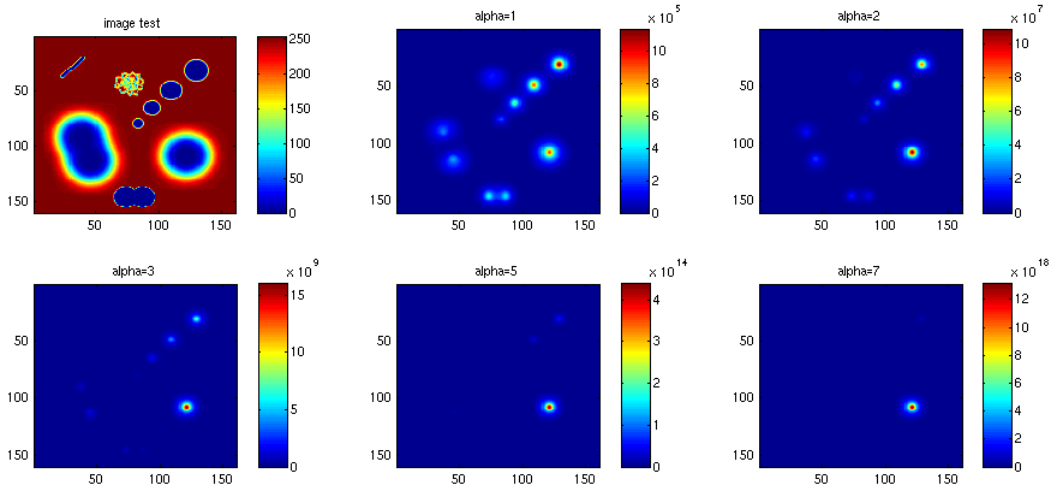

Figure 4.4.9: Illustration of the synthetic image generated by GIMP and the FRST results for different α values.

Parameter	Chosen value
$radii$	$[1, 2, 3]$
α	3
A_n	$\sigma = 0.25 \times n$

Table 4.4.1: FRST parameter setting for Memento datasets.

A choice of $\alpha = 3$ is a compromise allowing relatively spherical points to be detected without missing small disks.

FRST feature

A summary of FRST parameter setting used for memento dataset to hihlight CMBs are given in Table 4.4.1. In order to define the sphericity feature, the mean sphericity values on T2*, IFM, SWI and mIP-SWI were calculated. For IFM, positively affected pixels were considered since CMBs appear as hyperintensity on IFM.

In addition to FRST, CMBs have a very specific shape that discriminates them from blood vessels. To emphasize these characteristics five different 2D shape features were calculated and used as described below

Structure elongation

For 3D structures "Compactness" is approximately a ratio of surface area to volume, spheres having the highest theoretical compactness. For 2D images, we defined the "Elongation" as the D_{min}/D_{max}, CMBs have a very high compactness and veins have a

very low compactness. D is the diameter.

Equivalent Circular Diameter (ECD)

ECD is defined as

$$ECD = \sqrt{4 \times Area/\Pi} \tag{4.4.24}$$

Covariance matrix's three eigenvalues

The covariance matrix was calculated in the connected component bounding box (5x5).

Relative anisotropy (RA)

RA is calculated using the three eigenvalues of the previously calculated covariance matrix

$$RA = \sqrt{\frac{1}{2}} \times \sqrt{\frac{(a-b)^2 + (b-c)^2 + (c-a)^2}{a+b+c}} \tag{4.4.25}$$

where a, b and c are the eigenvalues of the covariance matrix; a is the largest value, b is the median and c is the smallest values.

Circularity C

C is defined as the ratio of the area of the CMB shape to the area of a circle having the same perimeter

$$C = \frac{4\Pi \times area}{Perimeter} \tag{4.4.26}$$

Intensity-based features:

mean intensity on T2* Magnitude image, IFM and SWI images were extracted after normalization.

Classification

Common machine learning tasks were performed in MATLAB using the Classification Learner and functions in the Statistics and Machine Learning Toolbox. It offers the possibility to choose between classification algorithms, to train a classifier and evaluate the accuracy of a classifier (confusion matrices, ROC curves, classification error). It follows the following procedure

1. Feature selection
2. Specifying cross-validation schemes
3. Training a range of classification models, including support vector machines (SVM), boosted and bagged decision trees, k-nearest neighbor, and discriminant analysis
4. Performing model assessment and model comparisons using confusion matrices and ROC curves to help choose the best model for the data
5. Integrating trained models into applications by testing its usefulness on new data.

Several classifiers have been trained on these features to test accuracy. Considering the consensus identification realized in the comparison study (chapter 3), initial candidates were labeled as "definite", "possible" or "false positive". Features for these objects were extracted and used to train several classifiers; the accuracy of each classifier was then assessed. All classifiers were trained to see which settings produce the best model with our data, giving the better accuracy for all classes. Selected model can be improved by feature selection, and by changing some advanced options. subjects without CMBs were excluded from this proof-of-concept to reduce the gap between FP and CMBs classes in the classification step.

4.5 Experiment and preliminary results

Here, preliminary results of thresholding and classification steps are presented.

4.5.1 Thresholding results

For this proof of concept, threshold values for different image types were chosen empirically allowing at maximum 10% FN. Results of this step are illustrated in Table 4.5.1.

images	α_1	α_2	number of FN	number of FP
T2*	2	1	8	129161
IFM	0.5	-	3	56632
SWI	1.5	2	5	42625
mIP-SWI	1.5	2	4	40989
Final image	-	-	13	9195

Figure 4.5.1: Thresholding results.

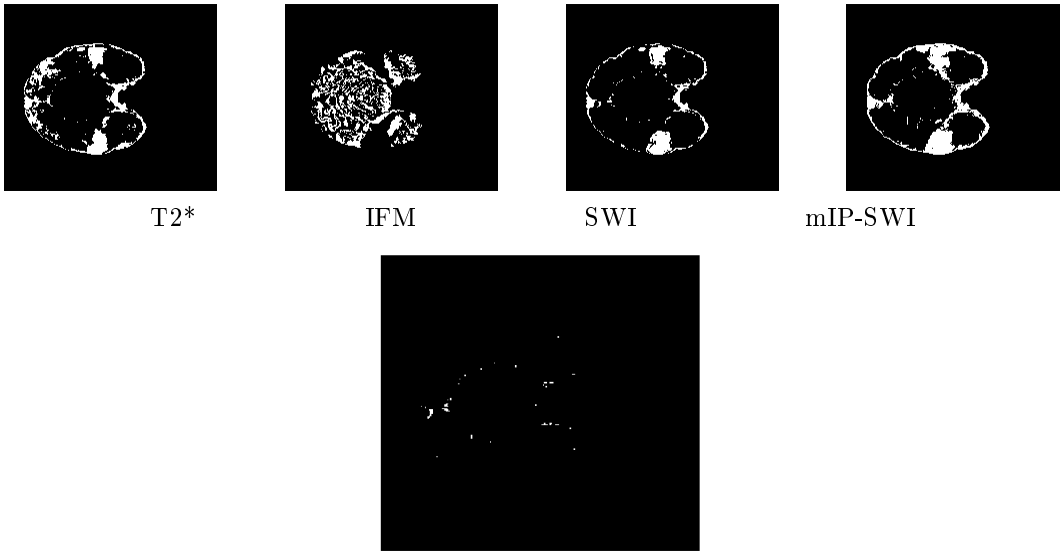

Figure 4.5.2: Illustration of an example of thresholding final result.

Figure 4.5.2 illustrates an example of resulting objects after the thresholding process.

The thresholding step had a high sensitivity of 90%, only missing 13 CMBs out of 136. Using the four images for thresholding results in very small objects better suited for morphological analysis. However, as expected, a very large number of false positives was found.

4.5.2 Classification results

Features were extracted from seven datasets to be used for the training step. The first and second classes were weighted by 500 to decrease the bias due to the large number of false positives with respect to true definite CMBs and possible CMBs. Several classifiers

subject	True CMBs	FN	False Positives
subject 1	17	5	10
subject 2	4	2	5
subject 3	30	12	3

Table 4.5.1: The number of true CMBs and CMBs found with the automatic identification method along with false positives are listed for each of the test subjects.

have been trained on these features. Figure 4.5.3 summarizes training models results ; results of different trained classifiers and their performance accuracy are given in the left panel. The most accurate model is the one generated by "complex tree classifier"; its confusion matrix and ROC curve are given respectively in the middle and right panels. *The basic idea of the tree classification methods is to partition the space and identify some representative centroids using hyperplanes as classification boundaries. Classification trees are a hierarchical way of partitioning the space. We start with the entire space and recursively divide it into smaller regions. At the end, every region is assigned with a class label*[2].

The advantages of this type of algorithm are its fast prediction speed, fast training time, and the simplicity of its interpretation.

Giving three new unknown datasets, classification results are given in Table 4.5.1.

The classification step is able to remove most of the false positives for the three unknown datasets at the loss of sensitivity (almost 50% FN). The predictive model failed to predict true CMBs.

4.6 Discussion & Perspectives

The presented method is a proof-of-concept of the segmentation method to be further completed and then validated on larger data. The general segmentation scheme consist of a first step of selecting initial potential CMBs using a multi-contrast thresholding step and a classification step of these points using a machine learning classifier. T2*

[2]Matlab description.

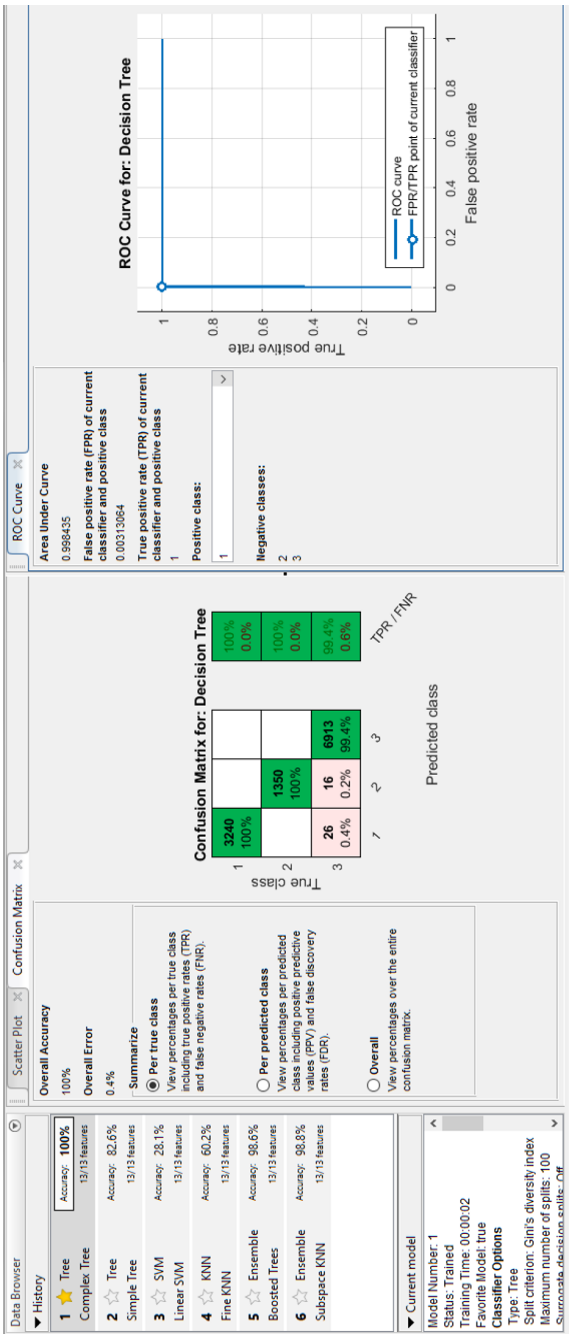

Figure 4.5.3: Assessment of trained model's accuracy using the Matlab learning classifier apps.

magnitude, internal field map, SWI and mIP-SWI were used to extract intensity and geometric features. A feature vector of 13 dimensions was used: mean intensity on T2*, SWI and IFM; mean intensity of FRST function applied on T2*, IFM, SWI and mIP-SWI; circularity; relative anisotropy, elongation, effective circular diameter and the three eigenvalues of the covariance matrix.

False positives rate resulting from segmentation scheme, indicate that the second step is the step needing to be improved for higher specificity and sensitivity; this could be accomplished by including new features more specific for each class;

- CMBs signature on IFM may be used: Correlation with a dipolar pattern can be added in the feature vector.
- Other geometric features may be added: Radon transform and or Hessian matrix.
- Creating a vein mask using mIP-SWI that can be applied after thresholding as a pre-processing step to remove elongated structure and thus reduce computational cost of false positive elimination using machine learning. However, the projection yields localization uncertainty and may be challenging to embed.

No feature selection step was performed or investigated here and further improvements could be achieved by keeping only the most adequate features during the training and testing steps.

Features normalization is an important step and needs more investigation.

Anatomical location prior may also be improved using sulci. Even though it would probably not result in a dramatic improvement in sensitivity, it could be an important step in removing veins.

Interpolation may also should be investigated as small CMB may become easier to detect unless if their shape is altered.

Here, we present a proof of concept of a segmentation approach to deal with CMBs; for this we used 10 datasets with CMBs that were labeled during comparison study. 8 datasets were using for the training step; enlarging the training dataset assuredly would help to create a more accurate predictive model.

In conclusion we have shown a proof of concept of a segmentation method for CMB detection. Although we presented some results, the whole training process need to be further explored in more depth. The main contribution of this technique is a higher specificity due to the use of internal field map. Further evaluation § on a larger group of patients with more diverse types of CMBs needs to be done to prove the applicability of this method as a general CMB detection algorithm.

Chapter 5

CONCLUSION & PERSPECTIVES

Summary and conclusion

CMBs, small hypo-intense foci with a maximum diameter of 10 millimeters, were first thought clinically silent. They are now considered as an imaging marker of cerebral small vessel diseases and their clinical involvement is increasingly recognized; they may be associated with an increased risk of hemorrhagic stroke, ischemia and dementia such as Alzheimer's disease. However, their relation with pathology and its causality remains largely to be understood, partly because of their tricky characterization in-vivo; developing new techniques for characterizing CMBs in vivo thus appear of primary import. The routine use of the magnitude image of GRE T2*-weighted sequences for vascular exploration has been shown to be far from optimal for detecting CMBs. On this image, in-vivo detection suffers from low specificity, poor inter-rater reproducibility and is biased by acquisition parameters. However, these focal hypo-intensities result from local magnetic field inhomogeneities caused by their hemosiderin content and the use of the phase image of the same sequence appears as interesting additional input, being directly linked with field variations. This phase information has been introduced in the SWI technique that has allowed better CMBs detection. This technique allows to enhance blood (as in blood vessels) and its degradation products (as in CMBs) and has been shown to allow a better appreciation of CMBs prevalence than T2* magnitude image. However, SWI is not always available on MR scanners and thus not necessarily feasible in large multi-center clinical studies, whereas routine GRE T2*-weighted sequences can be acquired on all systems, and phase images can be saved along with magnitude images on nearly all systems. In the Memento cohort, image

acquisition has been standardized as much as possible to minimize inter-site variability. However, difference between Philips and Siemens sequences parameters still remain because specific characteristics of each manufacturer. The aim of this PhD was to develop a robust tool for the automatic segmentation of cerebral microbleeds in a multi-center dataset in a clinical setting. To do so, it was necessary both to better characterize CMBs, as a large number of false positives has been reported in the literature for segmentation methods, and to take into account the multi-center aspect of the available dataset.

After introducing the historical context of CMBs and their underlying pathology the technical aspect of their detection was developed. State-of-the art methods for their visual and automatic detection were described and compared, and they revealed the need to improve the specificity of automatic techniques. This was the scope of the new robust and efficient method developed in the second chapter to extract usable information from phase images, as phase was expected to allow refining the definition of CMBs on clinical images. This new technique for processing the phase image from 2D GRE T2*-weighted sequence includes unwrapping and background field correction by carrying out the key numerical operation (Laplace) in 2D on a slice-by-slice basis. This tool was called 2DHF for 2D harmonic filtering. This method results in internal field maps (IFM) which reveal local field details linked with magnetic inhomogeneity within the region of interest. The new technique was shown to better preserve the phase contrast than high pass filtering and better eliminate inter-slice effects compared to a method widely used for the same purpose (PDF). The method was evaluated on both a synthetic phantom and multi-center 2D datasets and compared with two state-of-the-art methods. It proved to yield consistent results on synthetic images and to be applicable and robust on patient data. As a proof-of-concept, we demonstrated that it is possible to find a magnetic signature of CMBs and CMCs on internal field maps generated with 2DHF on 2D clinical datasets that gives consistent results with CT-scans in a subsample of 10 subjects acquired with both modalities. This work focusses on 2D GRE acquisition, which is widely used in clinics but all recent developments in the field of phase imaging focus on 3D acquisition; this new implementation could thus allow a more systematic use of phase images in clinical routine. The usefulness of this new information was evaluated for clinical routine in the third chapter through systematic experiments to compare the ratings obtained by trained observers with several image types, from T2* magnitude to IFM. 15 participants from the MEMENTO multi-center cohort were selected, with a wide range of CMB

number. After pilot experiments, T2* magnitude, Susceptibility Weighted Imaging (SWI) minimum intensity projection (mIP) on three slices and IFM were kept for the rating experiments. Six raters of various background and expertise independently selected definite or possible CMBs from a specific user interface that displayed subjects and images in random order. Rating results were compared with respect to a specific consensus reference, on both a single lesion point of view and a subject-type point of view. IFM yielded increased sensitivity and specificity for CMB identification compared to T2* magnitude and SWI-mIP images. SWI increases the contrast of CMBs, both revealing small CMBs and increasing the number of mistaken CMBs. In fact, it reveals many flow voids from small blood vessels and enhanced some hypo-signal artifact that can be mistaken for CMBs. Thus, the sensitivity increase with SWI comes at the expense of a decrease in specificity. Moreover, SWI enhances the blooming effect compared with magnitude images, which can lead to an over-estimation of the CMB extent. Finally, Inter-rater variability was decreased with IFM when identifying subjects with numerous lesions, with only a limited increase in rating time. IFM thus appears as an interesting candidate to improve CMB identification in clinical setting. A proof-of-concept was finally presented for designing a segmentation method that would make use of robust features on several complementary aspects (intensity, shape and susceptibility). The conclusion of the comparison experiments was used to define the features, to take advantage of each image type. Candidate points for CMBs are first selected and then classified using multi-contrast features to discriminate CMBs from non-CMBs points. The method was implemented and validated on the fifteen participants from the comparison study. First experiments showed very promising results regarding the decrease of false positives while keeping a low false negative rate. Further validation is needed on a larger dataset to validate this finding.

Perspectives

This PhD addressed three main topics for which further developments could be considered. The first topic is related to the characterization of CMBs using MR phase images on a multicenter dataset and was addressed by designing, implementing and evaluating the 2DHF method. This method proved efficient for CMB characterization or further application in vascular imaging. However, this characterization remains sensitive to the choice of echo time, as it affects the size of the signal void area around each CMB and size measurement may still not be relevant on

IFM to fully characterize CMB burden. More advanced tools, such as Quantitative susceptibility Mapping (QSM) (more detailed in Appendix 2), aim at quantifying susceptibility variations and may present a good tool for CMBs characterization. In parallel with the work described here, we investigated the feasibility of solving the "field to source" inverse problem from IFM generated by 2DHF method on our multicenter dataset, as working on susceptibility "sources" may overcome the blooming effect issue and make it possible to access to the real size of CMBs, both for cross-study comparisons and robust longitudinal data analysis. In fact, the dipole deconvolution in QSM can theoretically eliminate the blooming artifact when proper prior information is used, such as morphology derived from images with no or little blooming artifact. Quantitative aspects of CMBs characterization are shortly described in Appendix 2; preliminary results were obtained during the internship of Kanza Dekkiche where we evaluated and compared the state-of-the-art QSM methods on multi-center datasets. In fact, the main issue for QSM maps reconstruction is to solve an ill-posed inverse problem; to do so, priors are introduced, such as regularization. The issue of regularization parameter setting for multicenter dataset was investigated to overcome center/machine variabilities, but this evaluation needs to be further developed. Moreover, QSM is inherently a 3D problem and further analyses are needed to validate it in the 2D context. Liu et al in [Liu et al., 2012] retrospectively analyzed 40 CMBs detected in 10 patients; they compared the efficiency of QSM, R2* map, T2*weighted magnitude and SWI for CMB detection on an advanced 3D multi-echo spoiled gradient echo sequence in order to investigate whether QSM can overcome the variability due to TE modifications for measuring CMB burden. This study showed that the total susceptibility of a CMB is an intrinsic physical property and is not related with echo time; this conclusion is in accordance with previous phantom and ex vivo validations in which QSM had proven to be efficient to accurately quantify the amount of iron. QSM may thus be the most relevant direction for future work for better characterizing CMBs.

However, 3D multi-echo imaging may be crucial to obtain an even better sensitivity and specificity for CMBs identification, but remain challenging in multicenter context. Therefore, as a second topic, I was part to the CATI quantitative imaging working group aiming at optimizing a new 3D multi-echo T2*-weighted GRE sequence on 3T systems from the three main manufacturers. This sequence was designed to obtain both reliable R2* maps and better characterization for CMBs. Its principle consists of acquiring a series of T2*-weighted images (magnitude and phase) using the same TR but a series of TE. Previous studies showed that, by using more

adapted methods for GRE phase with multiple TE, field inhomogeneity artifact could be reduced further while preserving contrast elsewhere in the image. This kind of sequence makes it possible to accommodate or correct air/tissue interfaces. High bandwidth imaging avoids geometric distortion, and multi-echo data offer a means to ideally unwrap phase data on a voxel by voxel basis. Consequently, QSM on this type of data would yield more accurate results than 2D single echo acquisition. Datasets are being acquired with this sequence for three studies managed by the CATI, and a specific one focuses on vascular abnormalities in ageing. Furthermore, multi-echo 3D GRE imaging may offer a means to image the entire vascular system, including arteries and veins alike. The field is still developing, and there are hints that technical advances in magnet homogeneity, gradient strengths, and faster imaging methods such as parallel imaging techniques may make it possible in the future. The third topic raised by this PhD is to further develop the automatic segmentation tool for CMBs and to validate it on a large multicenter dataset. The method presented above is a proof-of-concept applied on fifteen participants; a larger validation with more participants is thus needed. Even though the proof-of-concept described using two steps seems adapted for CMB identification, both steps could be further improved by increasing the sensitivity of the first step and the specificity of the second step. Thresholds may not be statistical but inspired from the magnetic signature of CMBs, for example. An "a contrario" approach may also be used for initial candidate selection. In fact, this probabilistic approach aims at identifying signal outliers in a given background. For the classification step, the method needs to be extended to include more local and global multi-contrast features.

- mIP-SWI yields interesting information to differentiate CMBs from elongated veins, and a "mIP-feature" should be defined.

- CMBs magnetic signature on IFM was not yet used. It is a defined as a sign inversion in sagittal view. Intensity profiles measured along several directions in the sagittal plane around candidate voxels could be used to define specific features. The dipolar pattern with ring-like effect would characterize a CMB. A multi-scale correlation with the response of a unit dipole may also be a good discriminant.

- Feature derived from T2-weighted image intensity may make it possible to exclude hyperintensities and discriminate cavernous malformations.

- QSM features may straighten the segmentation tool with a direct insight to the real extent of CMBs.
- QSM features may also help differentiating CMBs from other rare mimicking lesions such as brain capillary telangiectasia (small, asymptomatic low flow vascular lesions of the brain)

Regarding the classification method, features were not selected to keep only the most discriminant features; a features selection step could be undertaken to use only most discriminant features and thus strengthen the generalization of the method. Other classifiers need to be investigated when features normalization and selection will be embedded. The automatic identification method will also have to be evaluated and adapted for 3D multi-echo GRE T2*-weighted images.

Finally, the aim of the PhD was to add a new service to the CATI portfolio, by reliably assessing the number of CMBs. However, an automatic identification method could allow further developments and analysis. The first one could be related with the rating scales, MARS and BOMBS, that were proposed in the literature, as described in chapter 1. These scales both embed localization characteristics, as the clinical relevance of CMBs has been shown to be related with their localization. The automatic identification method would yield an image with voxels labelled as "definite CMBs" and "possible CMBs", and a straightforward extension would be to combine it either with a registered atlas or with a segmentation method to create an automatic report corresponding to the rating scales. The second issue is related with WHASA, another software that has been developed in the Aramis team by Thomas Samaille and that aims at segmenting White Matter Hyper intensities in ageing subjects. In fact, some questions were raised about the combination of the presence or absence of cerebral microbleeds and white matter hyper intensities and it was shown that these combinations are a risk factors for subsequent recurrent stroke types [Naka et al., 2006]. Therefore, an automatic identification and evaluation of both lesions will help further analysis and understanding of their underlying association.

* * *

APPENDIX

Appendix 1: How to simulate internal field map giving a susceptibility distribution

The forward approach mentioned in the numerical simulation section chapter 2 consists of the calculation of the internal field map and complex signal from a created susceptibility distribution as illustrated in the figure below:

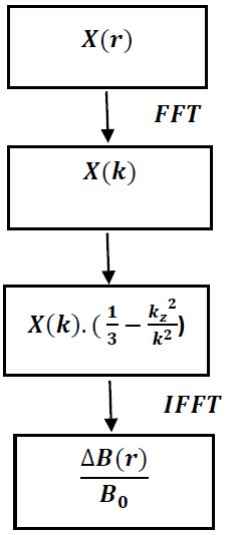

Figure 5.0.1: Forward approach to simulate internal field map, background field map, complex signal from a known susceptibility distribution as described in Salomir et al. [2003], Marques and Bowtell [2005].

Our experiment details were as follow:

1. Head simulation: An ellipsoid within a susceptibility of -9 ppm (part per million) is first created (main axis dimensions were 75 mm (in head-foot direction), 100 mm (in right-left direction) and 125 mm (in anteroom-posterior direction).

2. Air/tissue interfaces: Two small ellipsoids were removed, from the initial ellipsoid simulating the head, to simulate the strong effects that can be observed close to ear canals (dimension 5x10x16mm).

3. Small structures simulations : Multiple dipole inclusions were embedded in the central slice as described :

   a) Paramagnetic dots in the left hemisphere

   b) Diamagnetic dots in the right hemisphere.

4. Spatial resolution was chosen as 1x1x2.4mm.

5. The reconstruction matrix was chosen to be 210x210x256

6. The total field is created by the susceptibility distribution and computed using the forward approach [Marques and Bowtell, 2005, Salomir et al., 2003] : In Fourier domain, Field variation is related to susceptibility by

$$\triangle B(k) = \chi(k) \cdot D(k) \tag{5.0.1}$$

   k denotes the spatial frequency coordinates, and D is the expression of a unit dipole kernel in Fourier domain, given by

$$D(k) = \frac{1}{3} - \frac{k_z^2}{k^2} \tag{5.0.2}$$

   $k^2 = k_x^2 + k_y^2 + k_z^2$, knowing χ and D, the field can be calculated as

$$\triangle B(r) = IFFT(\chi(k) \cdot D(k)) \tag{5.0.3}$$

   .

7. Internal field of reference was obtained by repeating the total field calculation in the same numerical phantom but without simulating the "air cavities" (without step 2).

8. Complex MRI data simulation:

   a) Converting magnetic field to phase ($\varphi = \gamma \times B_0 \times TE \times \triangle B(r)$) with γ the gyromagnetic ratio of hydrogen nucleus, $B_0 = 3T$ and $TE = 20ms$.

   b) $2k\pi$ was added to generate phase wraps.

   c) In order to mimic the 2D GRE T2*-weighted scans :

      i. Random noise was generated from a normal distribution and added on both real and imaginary components, assuming SNR=30 (for magnitude)which corresponds to experimental values.

ii. A random constant within slice gradient was added to each slice to mimic the observed slice-to-slice inconsistency.

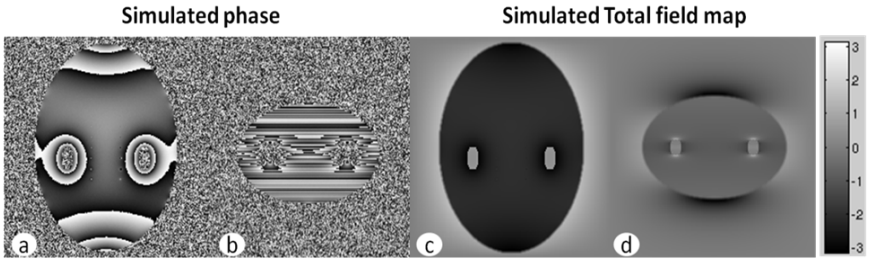

Figure 5.0.2: simulation illustration

Appendix 2: Quantitative susceptibility mapping: investigation in a multi-center context

Context

The aim of this work is to investigate the feasibility of the use of IFM obtained by 2DHF to map the magnetic susceptibility within the human brain. QSM provides a novel contrast mechanism in which the voxel intensity is linearly proportional to the underlying tissue apparent magnetic susceptibility. Several methods have been proposed in the literature to quantify susceptibility using T2* weighted GRE sequence and the main technical challenge is to choose the suitable method to solve the ill-posed problem of inverting the field maps to reconstruct the susceptibility maps.

The local field δB induced by local sources is given by the convolution of the volume susceptibility distribution χ with the dipole kernel d:

$$\delta B = d \otimes \chi \tag{5.0.4}$$

This spatial convolution can be expressed as a point-wise multiplication in Fourier domain:

$$\Delta B(k) = D(k) \cdot \chi(k) \tag{5.0.5}$$

where k denotes the spatial frequency coordinates and D is the response of a unit dipole called the green function. This Fourier expression provides an efficient way to predict the susceptibility distribution for a known local field variations:

$$\chi(k) = \frac{\Delta B(k)}{D(k)} \tag{5.0.6}$$

where D is given by

$$D(k) = \frac{1}{3} - \frac{k_z^2}{k^2} \tag{5.0.7}$$

D equals zero at a pair of cone surfaces at the magic angle ($\theta = 54^\circ$) with respect to B_0. This cone is illustrated in Figure 5.0.3.

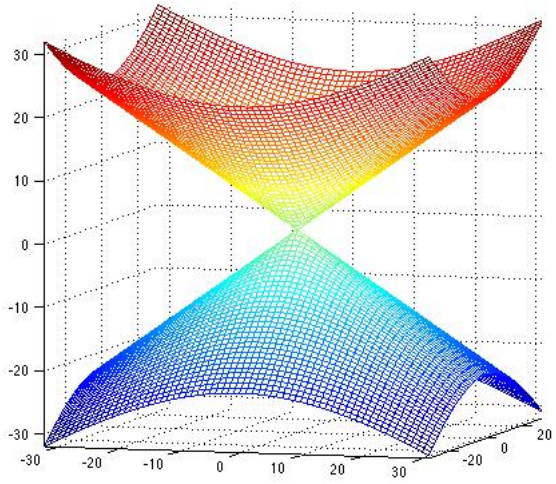

Figure 5.0.3: A visualization of the cone in Fourier domain.

Susceptibility distribution is, thus, under-determined at the spatial frequencies on the cone surface, which often leads to severe streaking artifacts in the reconstructed susceptibility distribution.

The truncated K-space division

The field-to-source inverse problem can be solved by several methods; the truncated K-space division (TKD) [Shmueli et al., 2009] and the Morphology Enabled Dipole Inversion (MEDI) [de Rochefort et al., 2010b].

The under-determined data in Fourier domain is only at the location of the cone and its immediate vicinity. For this region in k-space, TKD suggests to set spatial-frequencies of the dipole kernel to a pre-determined non-zero value for the division. The choice of due to the fact that TKD method only requires a single echo acquisition, and benefits from the ease of

implementation as well as the fast calculation speed. However, streaking artifacts are frequently present in the QSM and the susceptibility value is underestimated. The used regularized filter is defined by

$$D^{-1} = \begin{cases} \frac{1}{Th} & |D| < Th \\ \frac{1}{D} & |D| > Th \end{cases} \tag{5.0.8}$$

where Th is the small truncation value.

The Morphology Enabled Dipole Inversion

MEDI aims to solve the ill conditioned problem taking into account a prior information extracted from the magnitude image; edges that arises from the underlying change of tissue type, are the same cause for the change of susceptibility. A regularization is needed to enforce the smooth susceptibility distribution between edges. This observation is translated into mathematics in MEDI by

$$min \left\| W \left(D\chi - \delta B \right) \right\|_2^2 + \alpha^2 \left\| W_0 \chi \right\|_2^2 + \beta \left\| W_1 G \chi \right\|_2^2 \tag{5.0.9}$$

The first term of the equation is the data fidelity where the residual is weighted by the matrix W that contains the inverse of the standard deviation of the noise measurement in the magnitude image. In the second term, W_0 is a mask used to impose proper boundary condition. α is the regularization parameter of the second term. The third term corresponds to Tikhonov regularization; the gradient operator applied to the susceptibility map is used to impose susceptibility distribution to have the same edges as magnitude image. $W_1$is a weighting matrix to smooth the solution with respect to gradient image. This minimization is performed using the conjugate gradient algorithm. More details of the method are available in [Li et al., 2011, de Rochefort et al., 2010b].

Evaluation procedures

Both methods were validated on 3D data and both includes regularization parameter that needs to be set. To do so, an investigation was underwent on numerical simulation and on real data to determine the optimal values of regularization parameter for both method.

To evaluate the quantitative error estimation of TKD method, the mean of reconstructed susceptibility of each simulated structure was compared to its reference value in the initial simulated susceptibility map, and the root mean square error to quantify the degree of alteration due to the truncation of the dipole kernel. For MEDI method, besides the visual inspection, the optimal regularization parameter was investigated using the Lcurve which plot the norm of the Tikhonov solution with respect to its residual; the corner of the obtained Lcurve correspond to the optimal regularization parameter for data.

Results

TKD was applied for different truncation values Th=0.1, Th=0.2, Th=0.5 see Figure 5.0.4. For small Th values, obtained susceptibility maps are blurred with streaking artifacts detectable in the coronal and sagittal view, it alter the true susceptibility value. When increasing Th value, the streaking artifact is attenuated as shown in Figure for Th=0.2 and Th=0.5. For very large values of Th the susceptibility map is very smooth due to information loss induced by truncation. Consequently, Th=0.2 was selected as it presents the compromise between the under-estimation of the quantitative values and the streaking artifacts blurring the images. TKD allows to reconstruct QSM in 2.97 s.

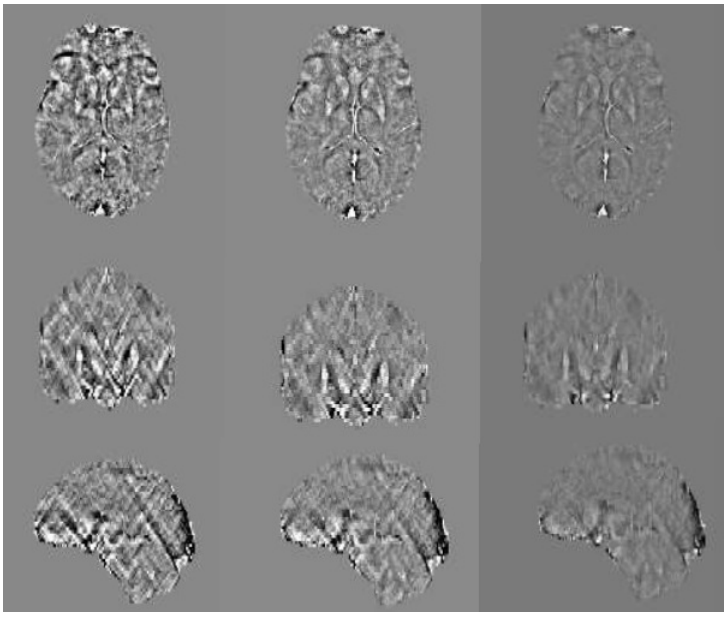

Figure 5.0.4: TKD on real data acquired from Siemens MR Scanner for truncation values Th a)Th=0.1, b) Th=0.2, c) Th=0.5.

Figure 5.0.5 illustrates QSM obtained with different β value for MEDI method. For better analysis, the α parameter associated to the second term that imposes proper boundaries, was removed. Lcurve analysis allowed to select the regularization parameter of MEDI to be $\beta = 10$; corresponding to the corner of the Lcurve.

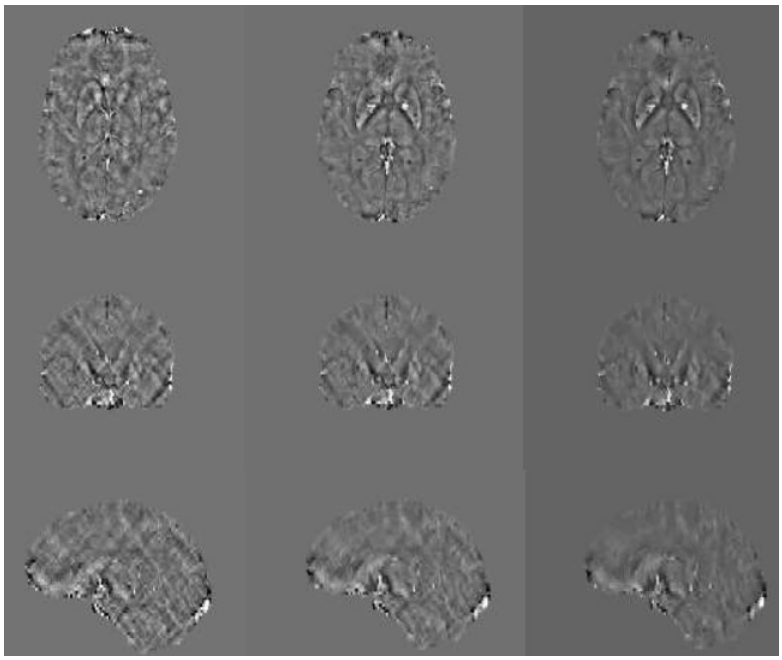

Figure 5.0.5: Susceptibility map obtained using MEDI on Siemens data a) for regularization Parameter$\beta = 1$, b)$\beta = 10$, c) $\beta = 100$.

Conclusion

This study demonstrated that MEDI is more accurate than TKD method on multi-center dataset. These results are preliminary and need further investigation on a large dataset to be confirmed. A more thorough quantitative analysis of brain deep structures, with known iron distribution, is also recommended for more accurate evaluation.

Appendix 3: Pilot experiment

A pilot experiment was first carried-out in order to evaluate the experiment settings: number of subjects, image types and the specifically designed Graphical User Interface (GUI) built with GUIDE in MATLAB. This was conducted by an experienced neuro-radiologist who selected the image types to be considered. Possible image types included: T2* magnitude, IFM and

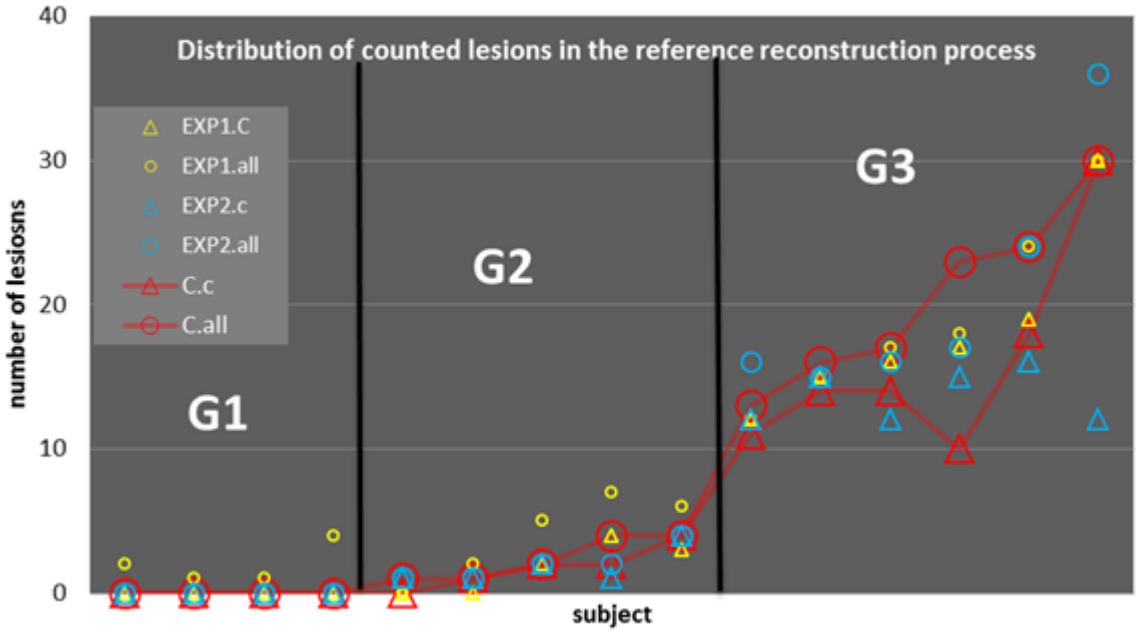

Figure 5.0.6: Number of detected CMBs for the 15 subjects for each rater and final consensus during the consensus reference building-up.

SWI minimum intensity projection (mIP) on n slices ($n = [2, 3, 4]$) and QSM calculated as in [de Rochefort et al., 2010a]. 15 subjects proved feasible and T2* magnitude, SWI-mIP on three slices and IFM were kept for the comparison experiments and the GUI was finalized as in Figure 3.2.1 and Figure 3.2.2. This evaluation GUI allows for displaying the overall 45 images, randomized on subjects and image types in order not to bias the comparison.

Appendix 4

On subject-type point of view, Figure 5.0.6 illustrates the consistency of the three groups as determined by the two raters and the consensus reference.

Appendix 5

Table 5.0.1 presents the rating results for all detected CMBs for each subject group (details of Table 3.3.4).

	G1 (N=4)			G2 (N=5)						G3 (N=6)					
	$\sum FP$			$\sum TP$			$\sum FN$			$\sum TP$			$\sum FN$		
	T2*	SWI-mIP	IFM	T2*	SWI-mIP	IFM	T2*	SWI-mIP	IFM	T2*	SWI-mIP	IFM	T2*	SWI-mIP	IFM
CRA	2	5	3	3	4	3	9	8	9	48	38	70	75	85	53
Exp.Junior1	1	1	0	4	3	3	8	9	9	70	62	83	53	61	40
Exp.Senior1	3	2	0	3	3	6	9	9	6	96	75	89	27	48	34
Trained. Ing	0	2	0	8	5	5	4	7	7	75	77	87	48	46	36
Exp.Senior2	1	0	0	3	2	2	9	10	10	89	76	76	34	47	47
Exp.Junior2	10	2	4	4	3	5	8	9	7	101	96	96	22	27	23
Median	2	2	0	4	3	4	9	9	8	82	76	76	41	48	38
Mm	0	0	0	3	2	2	4	7	6	48	38	38	22	27	23
Max	10	5	4	8	5	6	9	10	10	101	96	96	75	85	53

	$\sum FP$		
	T2*	SWI-mIP	IFM
CRA	5	16	5
Exp.Junior1	6	12	3
Exp.Senior1	28	27	11
Trained. Ing	11	27	8
Exp.Senior2	14	37	2
Exp.Junior2	67	160	53
Median	13	27	7
Mm	5	12	2
Max	67	160	53

Table 5.0.1: Rating results for all detected CMBs for each subject group (details of Table 3.3.4).

Bibliography

John Ashburner and Karl J Friston. Unified segmentation. 26(3):839–851, 2005. ISSN 1053-8119. doi: 10.1016/j.neuroimage.2005.02.018. URL http://www.ncbi.nlm.nih.gov/pubmed/15955494.

Muhammad Ayaz, Alexander S. Boikov, E. Mark Haacke, Wolff M. Kirsch, and Daniel K. Kido. Imaging cerebral microbleeds using susceptibility weighted imaging: one step toward detecting vascular dementia. *Journal of magnetic resonance imaging : JMRI*, 31(1):142–148, January 2010. ISSN 1053-1807. doi: 10.1002/jmri.22001. URL http://www.ncbi.nlm.nih.gov/pmc/articles/PMC2802499/.

Samuel R S Barnes, E Mark Haacke, Muhammad Ayaz, Alexander S Boikov, Wolff Kirsch, and Dan Kido. Semiautomated detection of cerebral microbleeds in magnetic resonance images. *Magnetic Resonance Imaging*, 29(6):844–852, July 2011. ISSN 1873-5894. doi: 10.1016/j.mri.2011.02.028. URL http://www.ncbi.nlm.nih.gov/pubmed/21571479.

Boubaker Belaroussi. Correction par traitement d images de l'artefact de susceptibilitÃ© magnetique dans les images IRM. 2005. URL http://theses-search.insa-lyon.fr/thematic-search.html?menuKey=theses_insa&submenuKey=authors&id=belaroussi_boubakeur.

Wei Bian, Christopher P. Hess, Susan M. Chang, Sarah J. Nelson, and Janine M. Lupo. Computer-aided detection of radiation-induced cerebral microbleeds on susceptibility-weighted MR images. *NeuroImage: Clinical*, 2:282–290, 2013. ISSN 2213-1582. doi: 10.1016/j.nicl.2013.01.012. URL http://www.sciencedirect.com/science/article/pii/S2213158213000144.

Berkin Bilgic, Adolf Pfefferbaum, Torsten Rohlfing, Edith V Sullivan, and Elfar Adalsteinsson. MRI estimates of brain iron concentration in normal aging using quantitative susceptibility mapping. *NeuroImage*, 59(3):2625–2635, February 2012. ISSN 1095-9572. doi: 10.1016/j.neuroimage.2011.08.077.

S. Chan, K. Kartha, S. S. Yoon, D. W. Desmond, and S. K. Hilal. Multifocal hypointense cerebral lesions on gradient-echo MR are associated with chronic hypertension. *American Journal of Neuroradiology*, 17(10):1821–1827, January 1996. ISSN 0195-6108, 1936-959X. URL http://www.ajnr.org/content/17/10/1821.

Andreas Charidimou, Clare Shakeshaft, and David J. Werring. Cerebral Microbleeds on Magnetic Resonance Imaging and Anticoagulant-Associated Intracerebral Hemorrhage Risk. *Frontiers in Neurology*, 3, September 2012. ISSN 1664-2295. doi: 10.3389/fneur.2012.00133. URL http://www.ncbi.nlm.nih.gov/pmc/articles/PMC3446731/.

Govind B. Chavhan, Paul S. Babyn, Bejoy Thomas, Manohar M. Shroff, and E. Mark Haacke. Principles, Techniques, and Applications of T2*-based MR Imaging and Its Special Applications. *Radiographics*, 29(5):1433–1449, September 2009. ISSN 0271-5333. doi: 10.1148/rg.295095034. URL http://www.ncbi.nlm.nih.gov/pmc/articles/PMC2799958/.

Genevieve Chene, Pierre-Jean Ousset, Florence Pasquier, Jean-Francois Dartigues, Audrey Gabelle, Jacques Hugon, Frederic Blanc, Pierre Krolak-Salmon, Mathieu Pierre Ceccaldi, Marie-Odile Barrellon, Olivier Beauchet, Catherine Belin, Athanase Benetos, Bruno Dubois, Armelle Gentric, Olivier Godefroy, Didier Hannequin, Olivier Hanon, Sandrine Harston, Caroline Hommet, Isabelle Jalenques, Olivier Moreaud, Marc Paccalin, Jeremie Pariente, Renaud David, Olivier Rouaud, Francois Sellal, Pierre Vandel, Martine Vercelletto, Olivier Marcy, and Carole Dufouil. MEMENTO: A NATIONAL COHORT ON DETERMINANTS AND BIOMARKERS OF ALZHEIMER'S DISEASE AND ASSOCIATED DISORDERS. *Alzheimer's & Dementia: The Journal of the Alzheimer's Association*, 10(4):P814, July 2014. ISSN 1552-5260. doi: 10.1016/j.jalz.2014.05.1600. URL http://www.alzheimersanddementia.com/article/S1552526014022638/abstract.

Ah-Ling Cheng, Saima Batool, Cheryl R. McCreary, M. L. Lauzon, Richard Frayne, Mayank Goyal, and Eric E. Smith. Susceptibility-weighted imaging is more reliable than T2*-weighted

gradient-recalled echo MRI for detecting microbleeds. *Stroke; a Journal of Cerebral Circulation*, 44(10):2782–2786, October 2013. ISSN 1524-4628. doi: 10.1161/STROKEAHA.113.002267.

Marie Chupin. *Segmentation automatique du complexe hippocampe-amygdale e partir de donnees d'imagerie par resonance magnetique : application e des cas cliniques et e la modelisation de sources en magneto/electro-encephalographie*. PhD thesis, Paris 11, January 2004. URL http://www.theses.fr/2004PA112126.

M. M. A. Conijn, M. I. Geerlings, G.-J. Biessels, T. Takahara, T. D. Witkamp, J. J. M. Zwanenburg, P. R. Luijten, and J. Hendrikse. Cerebral microbleeds on MR imaging: comparison between 1.5 and 7t. *AJNR. American journal of neuroradiology*, 32(6):1043–1049, July 2011. ISSN 1936-959X. doi: 10.3174/ajnr.A2450.

Thomas E. Conturo and Gregory D. Smith. Signal-to-noise in phase angle reconstruction: Dynamic range extension using phase reference offsets. *Magnetic Resonance in Medicine*, 15(3):420–437, 1990. ISSN 1522-2594. doi: 10.1002/mrm.1910150308. URL http://onlinelibrary.wiley.com/doi/10.1002/mrm.1910150308/abstract.

Cordonnier. Brain microbleeds: more evidence, but still a clinical dilemma. *Curr. Opin. Neurol.*, 24(1):69–74, February 2011. ISSN 1473-6551. doi: 10.1097/WCO.0b013e328341f8c0.

C. Cordonnier, W. M. van der Flier, J. D. Sluimer, D. Leys, F. Barkhof, and P. Scheltens. Prevalence and severity of microbleeds in a memory clinic setting. *Neurology*, 66(9):1356–1360, May 2006. ISSN 1526-632X. doi: 10.1212/01.wnl.0000210535.20297.ae.

Charlotte Cordonnier and Wiesje M van der Flier. Brain microbleeds and Alzheimer's disease: innocent observation or key player? *Brain*, 134(Pt 2):335–344, February 2011. ISSN 1460-2156. doi: 10.1093/brain/awq321.

Charlotte Cordonnier, Gillian M. Potter, Caroline A. Jackson, Fergus Doubal, Sarah Keir, Cathie L. M. Sudlow, Joanna M. Wardlaw, and Rustam Al-Shahi Salman. improving interrater agreement about brain microbleeds: development of the Brain Observer MicroBleed Scale (BOMBS). *Stroke; a Journal of Cerebral Circulation*, 40(1):94–99, January 2009. ISSN 1524-4628. doi: 10.1161/STROKEAHA.108.526996.

Ludovic de Rochefort, Ryan Brown, Martin R. Prince, and Yi Wang. Quantitative MR susceptibility mapping using piece-wise constant regularized inversion of the magnetic field. 60(4): 1003–1009, 2008. ISSN 1522-2594. doi: 10.1002/mrm.21710. URL http://onlinelibrary.wiley.com/doi/10.1002/mrm.21710/abstract.

Ludovic de Rochefort, A Delzor, M Guillermier, D Houitte, N Chaigneau, P Hantraye, and V Lebon. Quantitative Susceptibility Mapping In Vivo in the Rat Brain. volume 4997, 2010a.

Ludovic de Rochefort, Tian Liu, Bryan Kressler, Jing Liu, Pascal Spincemaille, Vincent Lebon, Jianlin Wu, and Yi Wang. Quantitative susceptibility map reconstruction from MR phase data using bayesian regularization: validation and application to brain imaging. *Magnetic resonance in medicine: official journal of the Society of Magnetic Resonance in Medicine / Society of Magnetic Resonance in Medicine*, 63(1):194–206, January 2010b. ISSN 1522-2594. doi: 10.1002/mrm.22187.

Andreas Deistung, Hans-Joachim Mentzel, Alexander Rauscher, Stephan Witoszynskyj, Werner A Kaiser, and Jurgen R Reichenbach. Demonstration of paramagnetic and diamagnetic cerebral lesions by using susceptibility weighted phase imaging (SWI). *Zeitschrift fÃŒr medizinische Physik*, 16(4):261–267, 2006. ISSN 0939-3889.

Andreas Deistung, Alexander Rauscher, Jan Sedlacik, Jorg Stadler, Stephan Witoszynskyj, and Jurgen R. Reichenbach. Susceptibility weighted imaging at ultra high magnetic field strengths: Theoretical considerations and experimental results. *Magnetic Resonance in Medicine*, 60(5): 1155–1168, 2008. ISSN 1522-2594. doi: 10.1002/mrm.21754. URL http://onlinelibrary.wiley.com/doi/10.1002/mrm.21754/abstract.

Jeff H. Duyn, Peter van Gelderen, Tie-Qiang Li, Jacco A. de Zwart, Alan P. Koretsky, and Masaki Fukunaga. High-field MRI of brain cortical substructure based on signal phase. *Proceedings of the National Academy of Sciences*, 104(28):11796–11801, October 2007. ISSN 0027-8424, 1091-6490. doi: 10.1073/pnas.0610821104. URL http://www.pnas.org/content/104/28/11796.

Alan C. Evans. The NIH MRI study of normal brain development. *NeuroImage*, 30(1):184–202, March 2006. ISSN 1053-8119. doi: 10.1016/j.neuroimage.2005.09.068. URL http://www.sciencedirect.com/science/article/pii/S105381190500710X.

F. Fazekas, R. Kleinert, G. Roob, G. Kleinert, P. Kapeller, R. Schmidt, and H. P. Hartung. Histopathologic analysis of foci of signal loss on gradient-echo T2*-weighted MR images in patients with spontaneous intracerebral hemorrhage: evidence of microangiopathy-related microbleeds. *AJNR. American journal of neuroradiology*, 20(4):637–642, April 1999. ISSN 0195-6108.

Amir Fazlollahi, Fabrice Meriaudeau, Victor L. Villemagne, Christopher C. Rowe, Patricia M. Desmond, and Paul A. Yates Olivier Salvado. *Automatic Detection of Small Spherical Lesions Using Multiscale Approach in 3d Medical Images*. 2013.

Wei Feng, Jaladhar Neelavalli, and E Mark Haacke. Catalytic multiecho phase unwrapping scheme (CAMPUS) in multiecho gradient echo imaging: removing phase wraps on a voxel-by-voxel basis. *Magnetic resonance in medicine: official journal of the Society of Magnetic Resonance in Medicine / Society of Magnetic Resonance in Medicine*, 70(1):117–126, July 2013. ISSN 1522-2594. doi: 10.1002/mrm.24457.

Jeroen D C Goos, Wiesje M van der Flier, Dirk L Knol, Petra J W Pouwels, Philip Scheltens, Frederik Barkhof, and Mike P Wattjes. Clinical relevance of improved microbleed detection by susceptibility-weighted magnetic resonance imaging. *Stroke; a journal of cerebral circulation*, 42(7):1894–1900, July 2011. ISSN 1524-4628. doi: 10.1161/STROKEAHA.110.599837.

S. M. Greenberg, S. P. Finklestein, and P. W. Schaefer. Petechial hemorrhages accompanying lobar hemorrhage: detection by gradient-echo MRI. *Neurology*, 46(6):1751–1754, June 1996. ISSN 0028-3878.

Steven M Greenberg, Meike W Vernooij, Charlotte Cordonnier, Anand Viswanathan, Rustam Al-Shahi Salman, Steven Warach, Lenore J Launer, Mark A Van Buchem, and Monique Mb Breteler. Cerebral microbleeds: a guide to detection and interpretation. *Lancet Neurology*, 8(2):165–174, February 2009. ISSN 1474-4422. doi: 10.1016/S1474-4422(09)70013-4. URL http://www.ncbi.nlm.nih.gov/pubmed/19161908.

S M Gregoire, U J Chaudhary, M M Brown, T A Yousry, C Kallis, H R Jager, and D J Werring. The Microbleed Anatomical Rating Scale (MARS): reliability of a tool to map brain microbleeds. 73(21):1759–1766, November 2009. ISSN 1526-632X. doi: 10.1212/WNL.0b013e3181c34a7d. URL http://www.ncbi.nlm.nih.gov/pubmed/19933977.

S. M. F. Gregoire. *Cerebral microbleeds as a marker of small vessel disease: new insights from neuro-imaging and clinical studies in stroke patients.* Doctoral, UCL (University College London), September 2014. URL http://discovery.ucl.ac.uk/1437813/.

S A Gronemeyer, J W Langston, S L Hanna, and J W Langston, Jr. MR imaging detection of calcified intracranial lesions and differentiation from iron-laden lesions. *Journal of magnetic resonance imaging: JMRI*, 2(3):271–276, June 1992. ISSN 1053-1807.

L F Guo, J Geng, M H Qiu, C H Mao, C Liu, and L Cui. Quantification of Phase Values of Cerebral Microbleeds in Hypertensive Patients Using ESWAN MRI. *Clinical neuroradiology*, 23(3):197–205, September 2013. ISSN 1869-1447. doi: 10.1007/s00062-012-0196-4.

R K Gupta, S B Rao, R Jain, L Pal, R Kumar, S K Venkatesh, and R K Rathore. Differentiation of calcification from chronic hemorrhage with corrected gradient echo phase imaging. *Journal of computer assisted tomography*, 25(5):698–704, October 2001. ISSN 0363-8715.

E M Haacke and J R Reichenbach. *Susceptibility Weighted Imaging in MRI: Basic Concepts and Clinical Applications.* 2011. URL http://eu.wiley.com/WileyCDA/WileyTitle/productCd-0470043431,subjectCd-BE70.html.

E. M Haacke, S. Mittal, Z. Wu, J. Neelavalli, and Y. C.n Cheng. Susceptibility-Weighted Imaging: Technical Aspects and Clinical Applications, Part 1. 30(1):19–30, January 2009. ISSN 0195-6108, 1936-959X. doi: 10.3174/ajnr.A1400. URL http://www.ajnr.org/content/30/1/19.

K. E Hammond, Lupo J. M, Xu D, Veeraraghavan S, Lee H, Kincaid A, Vigneron D. B, Manley G. T, Nelson S. J, and Mukherjee P. Microbleed Detection in Traumatic Brain Injury at 3t and 7t: Comparing 2d and 3d Gradient-Recalled Echo (GRE) Imaging with Susceptibility-Weighted Imaging (SWI). Proceedings of the International Society of Magnetic Resonnance in Medecine, 2009.

Kathryn E. Hammond, Janine M. Lupo, Duan Xu, Meredith Metcalf, Douglas A.C. Kelley, Daniel Pelletier, Susan M. Chang, Pratik Mukherjee, Daniel B. Vigneron, and Sarah J. Nelson. Development of a robust method for generating 7t multichannel phase images of the brain with application to normal volunteers and patients with neurological diseases. *NeuroImage*,

39(4):1682–1692, February 2008. ISSN 1053-8119. doi: 10.1016/j.neuroimage.2007.10.037. URL http://www.ncbi.nlm.nih.gov/pmc/articles/PMC2377156/.

Saima Hilal, Monica Saini, Chuen Seng Tan, Joseree A. Catindig, Way Inn Koay, Wiro J. Niessen, Henri A. Vrooman, Tien Yin Wong, Christopher Chen, Mohammad K. Ikram, and Narayanaswamy Venketasubramanian. Cerebral microbleeds and cognition: the epidemiology of dementia in Singapore study. *Alzheimer Disease and Associated Disorders*, 28(2):106–112, June 2014. ISSN 1546-4156. doi: 10.1097/WAD.0000000000000015.

Roy E. Hoffman. Measurement of magnetic susceptibility and calculation of shape factor of NMR samples. *Journal of Magnetic Resonance*, 178(2):237–247, February 2006. ISSN 1090-7807. doi: 10.1016/j.jmr.2005.09.009. URL http://www.sciencedirect.com/science/article/pii/S1090780705003125.

J. A. Hopkins and F. W. Wehrli. Magnetic susceptibility measurement of insoluble solids by NMR: magnetic susceptibility of bone. *Magnetic Resonance in Medicine*, 37(4):494–500, April 1997. ISSN 0740-3194.

John David Jackson. *Classical electrodynamics*. Wiley, New York, 1999. ISBN 0-471-30932-X 978-0-471-30932-1.

Yuwei Jiang, Dazhi Yin, Dongrong Xu, Weiwei Men, Rui Cao, Bing Li, and Mingxia Fan. Investigating microbleeding in cerebral ischemia rats using susceptibility-weighted imaging. *Magnetic Resonance Imaging*, 33(1):102–109, January 2015. ISSN 1873-5894. doi: 10.1016/j.mri.2014.09.002.

Takoua Kaaouana, Ludovic de Rochefort, Thomas Samaille, Nathalie Thiery, Carole Dufouil, Christine Delmaire, Didier Dormont, and Marie Chupin. 2d harmonic filtering of MR phase images in multicenter clinical setting: Toward a magnetic signature of cerebral microbleeds. *NeuroImage*, 104:287–300, January 2015. ISSN 1095-9572. doi: 10.1016/j.neuroimage.2014.08.024.

Jan Klohs, Andreas Deistung, Ferdinand Schweser, Joanes Grandjean, Marco Dominietto, Conny Waschkies, Roger M Nitsch, Irene Knuesel, Jurgen R Reichenbach, and Markus Rudin. Detection of cerebral microbleeds with quantitative susceptibility mapping in the ArcAbeta mouse model of cerebral amyloidosis. *J Cereb Blood Flow Metab*, 31(12):2282–2292, December

2011. ISSN 0271-678X. doi: 10.1038/jcbfm.2011.118. URL http://www.ncbi.nlm.nih.gov/pmc/articles/PMC3323188/.

Wisnumurti Kristanto, Peter M. A. van Ooijen, Jaap M. Groen, Rozemarijn Vliegenthart, and Matthijs Oudkerk. Small calcified coronary atherosclerotic plaque simulation model: minimal size and attenuation detectable by 64-MDCT and MicroCT. *The International Journal of Cardiovascular Imaging*, 28(4):843–853, April 2012. ISSN 1569-5794. doi: 10.1007/s10554-011-9869-3. URL http://www.ncbi.nlm.nih.gov/pmc/articles/PMC3360866/.

Hugo J Kuijf, Jeroen de Bresser, Mirjam I Geerlings, Mandy M A Conijn, Max A Viergever, Geert Jan Biessels, and Koen L Vincken. Efficient detection of cerebral microbleeds on 7.0 T MR images using the radial symmetry transform. *NeuroImage*, 59(3):2266–2273, February 2012. ISSN 1095-9572. doi: 10.1016/j.neuroimage.2011.09.061. URL http://www.ncbi.nlm.nih.gov/pubmed/21985903.

Christian Langkammer, Ferdinand Schweser, Nikolaus Krebs, Andreas Deistung, Walter Goessler, Eva Scheurer, Karsten Sommer, Gernot Reishofer, Kathrin Yen, Franz Fazekas, Stefan Ropele, and Jurgen R Reichenbach. Quantitative susceptibility mapping (QSM) as a means to measure brain iron? A post mortem validation study. *Neuroimage*, 62(3):1593–1599, September 2012. ISSN 1095-9572. doi: 10.1016/j.neuroimage.2012.05.049.

P. C. Lauterbur. Image Formation by Induced Local Interactions: Examples Employing Nuclear Magnetic Resonance. *Nature*, 242(5394):190–191, March 1973. doi: 10.1038/242190a0. URL http://www.nature.com/nature/journal/v242/n5394/abs/242190a0.html.

Junghoon Lee, Jonghye Woo, Fangxu Xing, Emi Z. Murano, Maureen Stone, and Jerry L. Prince. SEMI-AUTOMATIC SEGMENTATION OF THE TONGUE FOR 3d MOTION ANALYSIS WITH DYNAMIC MRI. *Proceedings / IEEE International Symposium on Biomedical Imaging: from nano to macro. IEEE International Symposium on Biomedical Imaging*, 2013:1465–1468, December 2013. ISSN 1945-7928. doi: 10.1109/ISBI.2013.6556811. URL http://www.ncbi.nlm.nih.gov/pmc/articles/PMC3892671/.

S. H. Lee, H. J. Bae, S. J. Kwon, H. Kim, Y. H. Kim, B. W. Yoon, and J. K. Roh. Cerebral microbleeds are regionally associated with intracerebral hemorrhage. *Neurology*, 62(1):72–76, January 2004. ISSN 1526-632X.

L Li and J S Leigh. High-precision mapping of the magnetic field utilizing the harmonic function mean value property. *J. Magn. Reson.*, 148(2):442–448, February 2001. ISSN 1090-7807. doi: 10.1006/jmre.2000.2267.

Wei Li, Bing Wu, and Chunlei Liu. Quantitative susceptibility mapping of human brain reflects spatial variation in tissue composition. *Neuroimage*, 55(4):1645–1656, April 2011. ISSN 1095-9572. doi: 10.1016/j.neuroimage.2010.11.088.

Wei Li, Bing Wu, Alexandru V. Avram, and Chunlei Liu. Magnetic Susceptibility Anisotropy of Human Brain in vivo and its Molecular Underpinnings. *Neuroimage*, 59(3):2088–2097, February 2012. ISSN 1053-8119. doi: 10.1016/j.neuroimage.2011.10.038. URL http://www.ncbi.nlm.nih.gov/pmc/articles/PMC3254777/.

Tian Liu. *QUANTITATIVE SUSCEPTIBILITY MAPPING USING MAGNETIC RESONANCE IMAGING*. PhD thesis, Cornell University, New York, 2011.

Tian Liu, Krishna Surapaneni, Min Lou, Liuquan Cheng, Pascal Spincemaille, and Yi Wang. Cerebral microbleeds: burden assessment by using quantitative susceptibility mapping. *Radiology*, 262(1):269–278, January 2012. ISSN 1527-1315. doi: 10.1148/radiol.11110251.

G. Loy and A. Zelinsky. Fast radial symmetry for detecting points of interest. *Pattern Analysis and Machine Intelligence, IEEE Transactions on*, 25(8):959–973, August 2003. ISSN 0162-8828. doi: 10.1109/TPAMI.2003.1217601.

J.p. Marques and R. Bowtell. Application of a Fourier-based method for rapid calculation of field inhomogeneity due to spatial variation of magnetic susceptibility. *Concepts in Magnetic Resonance Part B: Magnetic Resonance Engineering*, 25B(1):65–78, 2005. ISSN 1552-504X. doi: 10.1002/cmr.b.20034. URL http://onlinelibrary.wiley.com/doi/10.1002/cmr.b.20034/abstract.

Grant McAuley, Matthew Schrag, Pal Sipos, Shu-Wei Sun, Andre Obenaus, Jaladhar Neelavalli, E. Mark Haacke, Barbara Holshouser, Ramona Madacsi, and Wolff Kirsch. Quantification of punctate iron sources using magnetic resonance phase. *Magnetic Resonance in Medicine*, 63 (1):106–115, 2010. ISSN 1522-2594. doi: 10.1002/mrm.22185. URL http://onlinelibrary.wiley.com/doi/10.1002/mrm.22185/abstract.

Grant McAuley, Matthew Schrag, Samuel Barnes, Andre Obenaus, April Dickson, Barbara Holshouser, and Wolff Kirsch. Iron quantification of microbleeds in postmortem brain. *Magnetic resonance in medicine: official journal of the Society of Magnetic Resonance in Medicine / Society of Magnetic Resonance in Medicine*, 65(6):1592–1601, June 2011. ISSN 1522-2594. doi: 10.1002/mrm.22745.

K. Murao, C. Rossi, and C. Cordonnier. Intracerebral haemorrhage and cognitive decline. *Revue Neurologique*, 169(10):772–778, October 2013. ISSN 00353787. doi: 10.1016/j.neurol.2013.07.021. URL http://linkinghub.elsevier.com/retrieve/pii/S0035378713008801.

H. Naka, E. Nomura, T. Takahashi, S. Wakabayashi, Y. Mimori, H. Kajikawa, T. Kohriyama, and M. Matsumoto. Combinations of the Presence or Absence of Cerebral Microbleeds and Advanced White Matter Hyperintensity as Predictors of Subsequent Stroke Types. *American Journal of Neuroradiology*, 27(4):830–835, January 2006. ISSN 0195-6108, 1936-959X. URL http://www.ajnr.org/content/27/4/830.

Hiromitsu Naka, Eiichi Nomura, Shinichi Wakabayashi, Hiroshi Kajikawa, Tatsuo Kohriyama, Yasuyo Mimori, Shigenobu Nakamura, and Masayasu Matsumoto. Frequency of asymptomatic microbleeds on T2*-weighted MR images of patients with recurrent stroke: association with combination of stroke subtypes and leukoaraiosis. *AJNR. American journal of neuroradiology*, 25(5):714–719, May 2004. ISSN 0195-6108.

R N K Nandigam, A Viswanathan, P Delgado, M E Skehan, E E Smith, J Rosand, S M Greenberg, and B C Dickerson. MR imaging detection of cerebral microbleeds: effect of susceptibility-weighted imaging, section thickness, and field strength. *AJNR. American journal of neuroradiology*, 30(2):338–343, February 2009. ISSN 1936-959X. doi: 10.3174/ajnr.A1355.

Jaladhar Neelavalli, Yu-Chung N Cheng, Jing Jiang, and E Mark Haacke. Removing background phase variations in susceptibility-weighted imaging using a fast, forward-field calculation. *Journal of magnetic resonance imaging: JMRI*, 29(4):937–948, April 2009. ISSN 1053-1807. doi: 10.1002/jmri.21693.

H. Offenbacher, F. Fazekas, R. Schmidt, M. Koch, G. Fazekas, and P. Kapeller. MR of cerebral

abnormalities concomitant with primary intracerebral hematomas. *AJNR. American journal of neuroradiology*, 17(3):573–578, March 1996. ISSN 0195-6108.

Jae-Hyun Park, Sang Won Seo, Changsoo Kim, Geon Ha Kim, Hyun Jin Noh, Sung Tae Kim, Ki-Chang Kwak, Uicheul Yoon, Jong Min Lee, Jong Weon Lee, Ji Soo Shin, Chi Hun Kim, Young Noh, Hanna Cho, Hee Jin Kim, Cindy W. Yoon, Seung Jun Oh, Jae Seung Kim, Yearn Seong Choe, Kyung-Han Lee, Jae-Hong Lee, Michael Ewers, Michael W. Weiner, David J. Werring, and Duk L. Na. Pathogenesis of cerebral microbleeds: In vivo imaging of amyloid and subcortical ischemic small vessel disease in 226 individuals with cognitive impairment. *Annals of Neurology*, 73(5):584–593, May 2013. ISSN 1531-8249. doi: 10.1002/ana.23845.

Marielle M. F. Poels, Meike W. Vernooij, M. Arfan Ikram, Albert Hofman, Gabriel P. Krestin, Aad van der Lugt, and Monique M. B. Breteler. Prevalence and Risk Factors of Cerebral Microbleeds An Update of the Rotterdam Scan Study. *Stroke*, 41(10 suppl 1):S103–S106, October 2010. ISSN 0039-2499, 1524-4628. doi: 10.1161/STROKEAHA.110.595181. URL http://stroke.ahajournals.org/content/41/10_suppl_1/S103.

Alexander Rauscher, Markus Barth, Jurgen R Reichenbach, Rudolf Stollberger, and Ewald Moser. Automated unwrapping of MR phase images applied to BOLD MR-venography at 3 Tesla. *Journal of magnetic resonance imaging: JMRI*, 18(2):175–180, August 2003. ISSN 1053-1807. doi: 10.1002/jmri.10346.

J R Reichenbach, R Venkatesan, D J Schillinger, D K Kido, and E M Haacke. Small vessels in the human brain: MR venography with deoxyhemoglobin as an intrinsic contrast agent. *Radiology*, 204(1):272–277, July 1997. ISSN 0033-8419. doi: 10.1148/radiology.204.1.9205259.

Jurgen R. Reichenbach and E. Mark Haacke. High-resolution BOLD venographic imaging: a window into brain function. *NMR in Biomedicine*, 14(7-8):453–467, November 2001. ISSN 1099-1492. doi: 10.1002/nbm.722. URL http://onlinelibrary.wiley.com/doi/10.1002/nbm.722/abstract.

G. Roob and F. Fazekas. Magnetic resonance imaging of cerebral microbleeds. *Current Opinion in Neurology*, 13(1):69–73, February 2000. ISSN 1350-7540.

Rares Salomir, Baudouin Denis de Senneville, and Chrit TW Moonen. A fast calculation method for magnetic field inhomogeneity due to an arbitrary distribution of bulk susceptibility. *Con-*

cepts in Magnetic Resonance Part B: Magnetic Resonance Engineering, 19B(1):26–34, 2003. ISSN 1552-504X. doi: 10.1002/cmr.b.10083. URL http://onlinelibrary.wiley.com/doi/10.1002/cmr.b.10083/abstract.

Thomas Samaille, Ludovic Fillon, Remi Cuingnet, Eric Jouvent, Hugues Chabriat, Didier Dormont, Olivier Colliot, and Marie Chupin. Contrast-Based Fully Automatic Segmentation of White Matter Hyperintensities: Method and Validation. *PLoS One*, 7(11), November 2012. ISSN 1932-6203. doi: 10.1371/journal.pone.0048953. URL http://www.ncbi.nlm.nih.gov/pmc/articles/PMC3495958/.

J. Scharf, E. Brauherr, M. Forsting, and K. Sartor. Significance of haemorrhagic lacunes on MRI in patients with hypertensive cerebrovascular disease and intracerebral haemorrhage. *Neuroradiology*, 36(7):504–508, October 1994. ISSN 0028-3940.

Marvin A. Schofield and Yimei Zhu. Fast phase unwrapping algorithm for interferometric applications. *Optics Letters*, 28(14):1194–1196, July 2003. doi: 10.1364/OL.28.001194. URL http://ol.osa.org/abstract.cfm?URI=ol-28-14-1194.

Matthew Schrag, Grant McAuley, Justine Pomakian, Arshad Jiffry, Spencer Tung, Claudius Mueller, Harry V. Vinters, E. Mark Haacke, Barbara Holshouser, Daniel Kido, and Wolff M. Kirsch. Correlation of hypointensities in susceptibility-weighted images to tissue histology in dementia patients with cerebral amyloid angiopathy: a postmortem MRI study. *Acta Neuropathologica*, 119(3):291–302, March 2010. ISSN 1432-0533. doi: 10.1007/s00401-009-0615-z.

Ferdinand Schweser, Andreas Deistung, Berengar W. Lehr, and Jurgen R. Reichenbach. Differentiation between diamagnetic and paramagnetic cerebral lesions based on magnetic susceptibility mapping. *Medical Physics*, 37(10):5165, 2010a. ISSN 00942405. doi: 10.1118/1.3481505. URL http://www.academia.edu/762037/Differentiation_between_diamagnetic_and_paramagnetic_cerebral_lesions_based_on_magnetic_susceptibility_mapping.

Ferdinand Schweser, Berengar Wendel Lehr, Deistung Andreas, and Reichenbach Jurgen Rainer. Sophisticated Harmonic Artifact Reduction for Phase Data (SHARP). *In proceeding of: Proc GC Intl Soc Mag Reson Med*, 2010b.

Ferdinand Schweser, Andreas Deistung, Berengar Wendel Lehr, and Jurgen Rainer Reichenbach. Quantitative imaging of intrinsic magnetic tissue properties using MRI signal phase: An

approach to in vivo brain iron metabolism? *NeuroImage*, 54(4):2789–2807, February 2011. ISSN 1053-8119. doi: 10.1016/j.neuroimage.2010.10.070. URL http://www.sciencedirect.com/science/article/pii/S1053811910013789.

Ferdinand Schweser, Andreas Deistung, Karsten Sommer, and Jurgen Rainer Reichenbach. Toward online reconstruction of quantitative susceptibility maps: Superfast dipole inversion. *Magnetic resonance in medicine: official journal of the Society of Magnetic Resonance in Medicine / Society of Magnetic Resonance in Medicine*, July 2012a. ISSN 1522-2594. doi: 10.1002/mrm.24405.

Ferdinand Schweser, Karsten Sommer, Andreas Deistung, and Jurgen Rainer Reichenbach. Quantitative susceptibility mapping for investigating subtle susceptibility variations in the human brain. *Neuroimage*, 62(3):2083–2100, September 2012b. ISSN 1095-9572. doi: 10.1016/j.neuroimage.2012.05.067.

Ferdinand Schweser, Michael G. Dwyer, Andreas Deistung, Jurgen R. Reichenbach, and Robert Zivadinov. Impact of tissue atrophy on high-pass filtered MRI signal phase-based assessment in large-scale group-comparison studies: a simulation study. *Frontiers in Biomedical Physics*, 1:14, 2013. doi: 10.3389/fphy.2013.00014. URL http://www.frontiersin.org/Journal/10.3389/fphy.2013.00014/abstract.

Mohamed L. Seghier, Magdalena A. Kolanko, Alexander P. Leff, Hans R. Jager, Simone M. Gregoire, and David J. Werring. Microbleed Detection Using Automated Segmentation (MIDAS): A New Method Applicable to Standard Clinical MR Images. *PLoS ONE*, 6(3):e17547, March 2011. doi: 10.1371/journal.pone.0017547. URL http://dx.doi.org/10.1371/journal.pone.0017547.

Matthew Shive, William David Stanish, Robert G. McCormack, Francisco Forriol, Nick Mohtadi, Stephane Pelet, Jacques Desnoyers, Jose Tamez-Pena, Saara Totterman, Adele Changoor, Alex Yaroshinsky, and Alberto Restrepo. Quantitative 3d MRI as a Valid Endpoint for Randomized Clinical Trials in Cartilage Repair and its Correlation with Repair Tissue Collagen Architecture. *Arthroscopy*, 29(10):e133–e134, October 2013. ISSN 0749-8063. doi: 10.1016/j.arthro.2013.07.169. URL http://www.arthroscopyjournal.org/article/S0749806313007184/abstract.

Karin Shmueli, Jacco A. de Zwart, Peter van Gelderen, Tie-Qiang Li, Stephen J. Dodd, and Jeff H. Duyn. Magnetic susceptibility mapping of brain tissue in vivo using MRI phase data. *Magnetic Resonance in Medicine*, 62(6):1510–1522, 2009. ISSN 1522-2594. doi: 10.1002/mrm.22135. URL http://onlinelibrary.wiley.com/doi/10.1002/mrm.22135/abstract.

Moon-Ho Song, S Napel, N J Pelc, and G H Glover. Phase unwrapping of MR phase images using Poisson equation. *IEEE Trans Image Process*, 4(5):667–676, 1995. ISSN 1057-7149. doi: 10.1109/83.382500.

Roger C. Tam, Andrew Riddehough, and David K. B. Li. Detection and measurement of coverage loss in interleaved multi-acquisition brain MRIs due to motion-induced inter-slice misalignment. *Medical Image Analysis*, 13(3):381–391, June 2009. ISSN 1361-8423. doi: 10.1016/j.media.2008.12.006.

A. Tanaka, Y. Ueno, Y. Nakayama, K. Takano, and S. Takebayashi. Small chronic hemorrhages and ischemic lesions in association with spontaneous intracerebral hematomas. *Stroke; a Journal of Cerebral Circulation*, 30(8):1637–1642, August 1999. ISSN 0039-2499.

Tian Liu, Ildar Tian Liu, Ludovic de Rochefort, Pascal Spincemaille, Jing Liu, A. John Tsiouris, and Yi Wang. A novel background field removal method for MRI using projection onto dipole fields (PDF). *NMR in Biomedicine*, 24(9):1129–1136, 2011. ISSN 1099-1492. doi: 10.1002/nbm.1670. URL http://onlinelibrary.wiley.com/doi/10.1002/nbm.1670/abstract.

Yoshito Tsushima, Jun Aoki, and Keigo Endo. Brain microhemorrhages detected on T2*-weighted gradient-echo MR images. *AJNR. American journal of neuroradiology*, 24(1):88–96, January 2003. ISSN 0195-6108.

Wiesje M Van der Flier and Charlotte Cordonnier. Microbleeds in vascular dementia: clinical aspects. *Exp. Gerontol.*, 47(11):853–857, November 2012. ISSN 1873-6815. doi: 10.1016/j.exger.2012.07.007.

Meike W. Vernooij, M. Arfan Ikram, Piotr A. Wielopolski, Gabriel P. Krestin, Monique M. B. Breteler, and Aad van der Lugt. Cerebral Microbleeds: Accelerated 3d T2*-weighted GRE MR Imaging versus Conventional 2d T2*-weighted GRE MR Imaging for Detection. *Radiology*, 248(1):272–277, July 2008. ISSN 0033-8419. doi: 10.1148/radiol.2481071158. URL http://pubs.rsna.org/doi/full/10.1148/radiol.2481071158.

David J. Werring. *Cerebral Microbleeds: Pathophysiology to Clinical Practice*. Cambridge University Press, May 2011. ISBN 978-1-139-49621-6.

Sam Wharton, Andreas Schafer, and Richard Bowtell. Susceptibility mapping in the human brain using threshold-based k-space division. 63(5):1292–1304, 2010. ISSN 1522-2594. doi: 10.1002/mrm.22334. URL http://onlinelibrary.wiley.com/doi/10.1002/mrm.22334/abstract.

Samuel Wharton and Richard Bowtell. Effects of white matter microstructure on phase and susceptibility maps. *Magnetic Resonance in Medicine*, pages n/a–n/a, March 2013. ISSN 1522-2594. doi: 10.1002/mrm.25189. URL http://onlinelibrary.wiley.com/doi/10.1002/mrm.25189/abstract.

Stephan Witoszynskyj, Alexander Rauscher, Jurgen R. Reichenbach, and Markus Barth. Phase unwrapping of MR images using Phi UN–a fast and robust region growing algorithm. *Medical Image Analysis*, 13(2):257–268, April 2009. ISSN 1361-8423. doi: 10.1016/j.media.2008.10.004.

Zhen Wu, Sandeep Mittal, Karl Kish, Yingjian Yu, J. Hu, and E. Mark Haacke. Identification of Calcification with Magnetic Resonance Imaging Using Susceptibility-Weighted Imaging: A Case Study. *Journal of magnetic resonance imaging : JMRI*, 29(1):177–182, January 2009. ISSN 1053-1807. doi: 10.1002/jmri.21617. URL http://www.ncbi.nlm.nih.gov/pmc/articles/PMC2646180/.

N Yamada, S Imakita, T Sakuma, and M Takamiya. Intracranial calcification on gradient-echo phase image: depiction of diamagnetic susceptibility. *Radiology*, 198(1):171–178, January 1996. ISSN 0033-8419.